FACULTY
OF MATHEMATICS
AND PHYSICS
Charles University

**DOCTORAL THESIS**

Mgr. Michael Alexandridis

# Adsorption of Metal Atoms and Growth of Metal Nanostructures on Silicon Surface - STM Study

Department of Surface and Plasma Science

Supervisor of the doctoral thesis: doc. RNDr. Ivan Ošt'ádal, CSc.
Study programme: Physics of Surfaces and Interfaces

Prague 2021

I declare that I carried out this doctoral thesis independently, and only with the cited sources, literature and other professional sources.

I understand that my work relates to the rights and obligations under the Act No. 121/2000 Sb., the Copyright Act, as amended, in particular the fact that the Charles University has the right to conclude a license agreement on the use of this work as a school work pursuant to Section 60 subsection 1 of the Copyright Act.

In Prague 25. 10. 2021.

Mgr. Michael Alexandridis

First and foremost, I would like to thank my supervisor, Ivan Ošt'ádal, for introducing me into the field of nanoscience, for sharing his immense knowledge with me and teaching me more skills (hard and soft) than are dreamt of in my philosophy, for all his patience and support from the time when I started as an undergraduate student.

My thanks also go to my colleagues Pavel Sobotík, Pavel Kocán, Petr Zimmerman, Karel Majer, Filip Rozbořil and Ondřej Krejčí for our friendly collaboration and helpful and critical discussions.

I would also like to thank the whole team of Pavel Jelínek from the Institute of Physics of the Czech Academy of Science for letting me share with them their precious measuring time at the Omicron LT STM.

Special thanks go to both my families - the Czech one and the Greek one - for their never ending support.

The above written text is a place of the first and the most personal contact between a curious reader and the author...and it is probably the only place, where the first can shape his ideas about the personality of the latter based on the choice of the words he uses to thank various people.

It is a custom to thank everybody the author deems physically or mentally involved in the process of writing the thesis. But to my mind: "It is a custom more honoured in the breach than the observance." [1]. Thus, as much as I appreciate all the support and help that all of you have provided me with, there is one thank that is far more sincere than all the thanks I was able to put together: Thank God it's over!

Title: Adsorption of Metal Atoms and Growth of Metal Nanostructures on Silicon Surface - STM Study

Author: Mgr. Michael Alexandridis

Department: Department of Surface and Plasma Science

Supervisor: doc. RNDr. Ivan Ošt'ádal, CSc., Department of Surface and Plasma Science

Abstract: Behaviour of Group III (Al) and IV (Sn) metals on Si(100) surface was studied by Scanning Tunneling Microscopy in a temperature range from 115 K to 350 K. Evolution of the length of Sn chains at room and elevated temperatures was studied by the method of repeated line scans. Activation energies and the respective frequency prefactors for detachment of different individual atoms from the chains' terminations were obtained by means of statistical processing. Kinetic Monte Carlo simulations were used to obtain activation energies for hops of Sn adatoms on the Si(100) surface at room temperature by fitting experimentally measured growth characteristics of Sn/Si(100). Three basic Al objects observed by Scanning Tunneling Microscopy at room temperature on Si(100) were identified and thoroughly described. Direct observation of Al adatom hopping on Si(100)-c$(4 \times 2)$ at 115 K was used to evaluate the activation energies for individual hops in directions parallel with Si dimer rows and perpendicular to Si dimer rows. Kinetic Monte Carlo simulations were used to obtain activation energies for hops of Al adatoms on the Si(100) surface at room temperature by fitting experimentally measured growth characteristics of Al/Si(100).

Keywords: STM, KMC, Al, Sn, Si(100), heteroepitaxy

# Contents

# 1. Introduction

Group III (Al, In, Ga) and Group IV (Sn, Pb) metals form on Si(100) surface oriented one dimensional (1-D) nanostructures (so called atomic chains), which were in the spotlight of scientific research for several past decades because of their promising application in the nanotechnologies as possible conducting nanowires. Even though these promises remained unfulfilled, the research of the metals on Si surfaces continues, though with lower intensity, until today.

For the experimental investigation of these systems, the scanning tunnelling microscopy (STM) was (and still is) extensively used. It is the possibility of concurrent acquiring of an atomic resolution, manipulation of the individual adatoms and study of the local electronic character that makes the STM an irreplaceable experimental tool. Theoretical studies are then primarily based on the density functional theory (DFT) calculations.

The ultimate goal which can be achieved in nanotechnology is the ability to have a full control over the grow of desired nanostructures together with the ability to predict their character. If we want to influence, in a controlled way, the growth of the aforementioned nanostructures in the early stages of deposition, and at the same time predict their character based on the experimental conditions, a detail knowledge of the processes accompanying the growth is necessary. To the processes that have to be thoroughly investigated belong for example a migration of the adatoms on the surface, attachment/detachment of the adatoms to/from the grown structures or to/from the surface defects.

The migration of the adatoms can be well characterized by the values of the activation energies for hops of adatom from one adsorption position to a neighbouring one. Unfortunately the direct estimation of their values from the experiments is complicated and it is often necessary to use the STM that enables cooling of the sample to low temperatures (in some cases several tens of Kelvins) to slow down the fast movement of the adatoms on the surface.

Similarly to the migration of the adatoms, the growth of the nanostructures can be well characterized by the values of the activation energies for the detachment of different types of the adatoms from these structures. Unlike for direct investigation of the adatom migration, to observe the detachment of adatoms from the nanostructures, it is often necessary to heat the samples to higher temperatures to support the disintegration of the structures.

From the metals listed at the beginning of this Chapter, until today only the hopping barriers for In were directly obtained from the low temperature experiments. Also only for In the activation energies for the detachment of individual adatoms from the grown nanostructures were experimentally obtained by the direct observations of disintegration of In chains. For the remaining metals, only theoretically calculated values or values obtained from kinetic Monte Carlo (KMC) simulations at room temperature (RT) are available. In this thesis we endeavour not only to fill several of the missing gaps in this knowledge base, but also to present a thorough study of one representative metal for each Group - Al and Sn - and to provide a comprehensive view on the growth of their structures on the Si(100) surface

In this thesis a combination of experimental and theoretical approaches is used to study adsorption of single adatoms, their diffusion and finally the formation and character of the grown nanostructures. The experimental methods used in the thesis are complex in-situ experiments employing observations by the STM. From the theoretical methods, KMC is used to simulate the growth process of Al and Sn on Si(100) surface.

The thesis consist of 7 chapters, including this Introduction. Chapters 2-3 sum up the basic knowledge about the silicon surfaces and growth of Group III and Group IV metal on these surfaces. Special attention is paid to the Si(100) surface and growth of Al and Sn on it.

The first half of Chapter 4 focuses on the STM method used throughout this thesis. The second half of Chapter 4 describes in detail the experimental set ups and conditions of all our experiments.

Chapter 5 introduces our atomistic lattice-gas model, which reflects the crucial features of the real investigated systems of Group III and Group IV metals on Si(100). It further describes in detail the background of the KMC simulations that were used to investigate the properties of our model and to simulate studied systems of Al and Sn on Si(100).

Chapter 6 contains our genuine experimental results. It is divided into 2 sections with Section 6.1 dealing with Sn on Si(100) and Section 6.2 concentrating on Al on Si(100). Even though the results of the 2 sections are individually summarized at the end of each of them, they are again repeated in Chapter 7 at the end of this thesis. Chapter 7, however, does not merely repeat the individual summaries, but it puts them together, compares all our findings and emphasize the similarities and contrasts of both the studied metals.

The thesis is provided with rich graphical content. Although we tried to explain everything clearly and distinctly within the main text, we usually attached an accompanying picture, graph or schema with additional description that allows the reader to imagine the problematic more easily and look at it from a different point of view. If not stated otherwise in the description, all the images used in the thesis origin from our experiments or are of our own design.

Full derivation of several equations within Chapter 6 is also provided. If the equation originated from our derivation, then the derivation is given in its full form. Also, if we were unable to find a full derivation of any equation in the literature and provide a curious reader with the respective link, we took our time to execute the derivation by ourselves and present it in this thesis.

# 2. Silicon surface

Being a crucial component of the majority of electronic devices (smartphones, televisions, computers and other everyday life gadgets) the importance of silicon in today's technological advances cannot be overstated. It is a semiconductor, which is almost exclusively used as a substrate and the electronic properties of which can be easily modified by doping. Because of its low cost, easy oxidation, high stability and possibility to prepare large single crystals, the silicon has enjoyed great popularity for more than half a century and its dominance in fabrication of microprocessors or fast memory storage components will most probably remain unshaken for much longer.

Silicon crystallizes in a diamond cubic lattice and each atom in the crystal is bounded by four strong sp$^3$ covalent bonds with its neighbours. The lattice constant of the Si crystal is $a = 5.43$ Å. In order to obtain a desired silicon surface, the crystal is cleaved along the respective crystallographic plane. Upon cleavage the covalent bonds between the silicon atoms are broken, the result of which are surface atoms that contain unpaired electrons in highly localized electronic states - so called dangling bonds. As a direct result, the surface free energy increases. To decrease this energy, the surface undergoes a process of reconstruction and relaxation consisting of rearranging and rebonding of the surface atoms. Even though there is a great variety of the silicon surfaces and their reconstructions, the reconstructions usually consist of only several basic building blocks (e.g. dimers, restatoms, adatoms). Si(100) surfaces consist of silicon dimers. Si(111) surfaces, on the other hand, consist of adatoms and restatoms.

## 2.1 Si(100) surface and its reconstructions

The Si(100) surface has a square symmetry with lattice constant $a/\sqrt{2} = 3.84$ Å. Because of a small angle deviation from the ideal crystallographic plane during the crystal cleavage (so called "miscut"), the resulting real surface is not a large flat plane, but it contains steps and terraces. Out of the three main crystallographic planes - (111), (100) and (110) - the plane (100) has the smallest density of atoms, but the highest surface energy [2] (see Table 2.1). The reason behind it is breaking of two bonds per one surface atom during the process of cleaving.

| | Si(100) | Si(111) | Si(110) |
|---|---|---|---|
| Density of atoms [cm$^{-2}$] | $6.78 \times 10^{14}$ | $9.59 \times 10^{14}$ | $15.66 \times 10^{14}$ |
| Surface energy [J/cm$^2$] | 2.13 | 1.51 | 1.23 |

**Table 2.1:** The densities of atoms and the surface energies for three main Si crystallographic planes.

Heating the cleaved crystal over a critical temperature ($\approx$ 1200°C) causes two neighbouring surface atoms to come closer to each other due to thermal vibrations. Consequently, the half-filled sp$^3$ orbitals of the two atoms overlap. A strong interaction between the orbitals causes them to dehybridize to orbitals (p$_x$ + p$_y$) and orbitals (s +p$_z$) [3]. The orbitals (p$_x$ + p$_y$) lay in the surface plane and create strong $\sigma$ bridge bond, while the orbitals (s $+p_z$) are perpendicular to the surface and create weak $\pi$ bond. A single pair of atoms which are bonded in such a way is called symmetric dimer. The dimers are arranged in long ladder-like rows in crystallographic directions [010] and [001] alternately on individual terraces forming the Si(100)-(2 × 1) reconstruction. The increase of the surface energy due to the elastic deformation of the bonds is much smaller than the decrease of the energy caused by the dimerization process. The final lowering of the surface energy is 2.0 eV per dimer according to [4] and 1.4 eV according to [5].

The symmetric configuration of dimers is, however, not the energetically most favourable state and the system undergoes a shift to a more favourable one [6]. One of the two atoms within the dimer comes closer to the second surface layer, while the other atom moves away from it. At the same time an electric charge is transferred from the lower atom to the upper one. This process (called dimer buckling) can be characterized as emptying of the $sp^3$ orbital of the lower atom and filling of the $sp^3$ orbital of the upper one. Due to this process the surface energy is further lowered by 0.2 eV per dimer according to [4] and 0.15 eV according to [5]. Such a rearranging of the electric charge causes an opening of an energy gap (0.9 eV wide) between a $\pi$ bonding and a $\pi^*$ anti-bonding state [7]. Because of a small activation energy for switching of the dimer buckling ($\approx$ 100 meV) [8, 9], the buckling of the dimers changes regularly at temperatures higher than $\approx$ 200 K, which is called flip-flop motion.

Side effect of the buckling is a mechanical stress exerted on the surface. The stress can be reduced by a periodic alteration of the buckled dimers with opposite tilt within the dimer row (so called antiphase buckling). The reduction of the stress is 0.02 eV per dimer according to [4] and 0.08 eV according to [5]. The antiphase buckling within the rows can result into two different surface reconstructions. The Si(100)-p(2 × 2) reconstruction originates from the buckled dimer rows being buckled in-phase with each other. The Si(100)-c(4 × 2) reconstruction has neighbouring buckled dimer rows buckled antiphase [10]. Even though the c($4\times2$) is the most stable of all the Si(100) reconstructions, according to [4] the energy difference compared to the p(2 × 2) is only 0.002 eV per dimer and according to [5] there is no energy difference at all. Schematic top views of all the types of Si(100) surface reconstructions with the transitions between them are depicted in Figure 2.1.

Although this work focuses on the Si(100) surface and its reconstructions, the reconstructions of the other already mentioned Si surfaces [(111), (110)] attract a comparable amount of attention in the scientific world, which is the main reason for mentioning them briefly at the end of this subsection. The most famous reconstruction of Si(111) is (7 × 7) [11, 12]. There exist, however, also other reconstructions of Si(111) such as (2 × 1) and metastable (5 × 5) [13]. Even though the investigation of the Si(110) and its reconstructions has been neglected for a long time, its importance in development of fast devices with low power consumption (e.g. FIN–FET transistors) [14] ranks it nowadays among major semiconductor surfaces. Even though its most famous reconstruction is (16 × 2) [15–22], it is also possible to create (5 × 8) surface reconstruction [23].

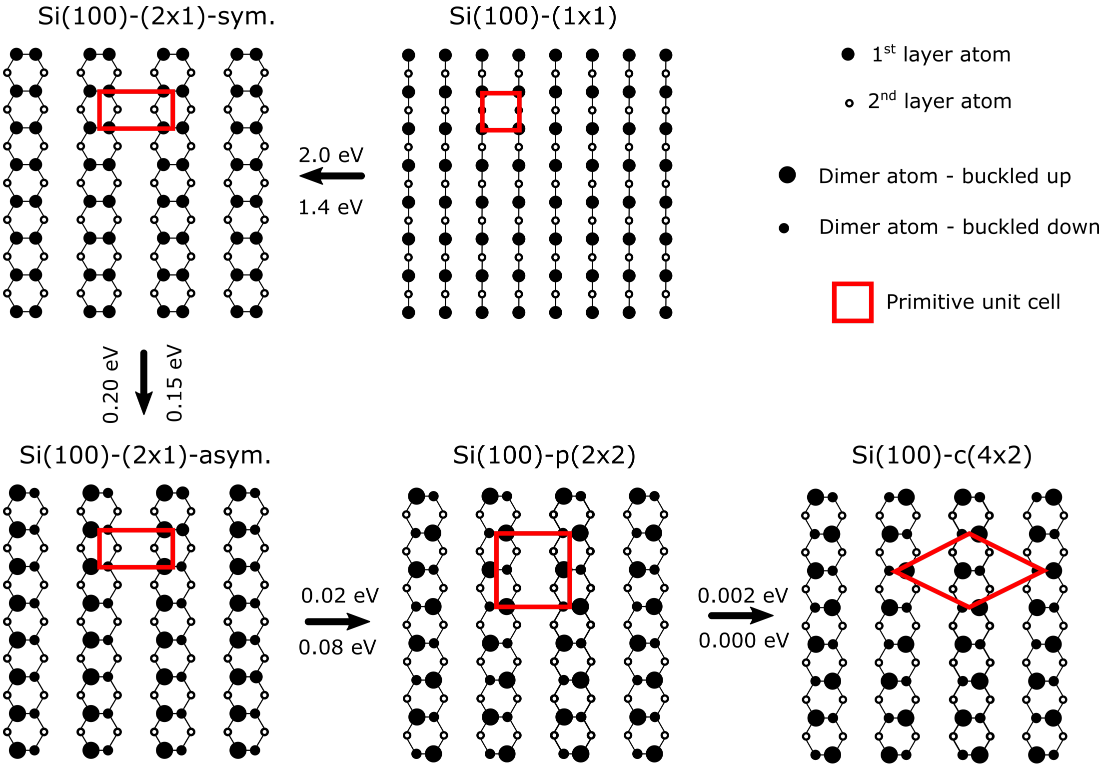

**Figure 2.1:** Different types and stages of Si(100) surface reconstruction. The energies of the energetic gain of the transition between individual types of reconstructions are "per dimer". The numbers above and below the arrows are taken from [4] and [5] respectively.

### 2.1.1 Surface defects

Unlike other Si surfaces, the Si(100) surface contains indispensable number of defects and it is very difficult to prepare it virtually defect free. We can divide the defects into two groups: structural defects and contamination defects. The structural defects are the result of the surface tendency to lower the stress caused by the reconstruction. The contamination defects origin from the residual gases in experimental chamber. In ultra high vacuum (UHV) condition we can usually observe four basic types of defects [7, 24]:

- *A*-type defect is the structural defect. It is interpreted as one missing Si dimer in a dimer row
- *B*-type defect is the structural defect. It is interpreted as two missing neighbouring Si dimers in a dimer row
- Split-off dimer defect is a defect caused by contamination of a substrate by Ni or W atoms. In the STM it looks like a *A*-type defect separated from a *B*-type defect by one Si dimer.
- *C*-type defect is the contamination defect caused by a disociative adsorption of a water molecule. The most common configuration of the *C*-type defect has both the hydroxyl group (OH) and hydrogen atom (H) bonded on the same side of the same Si dimer row to two neighbouring Si dimers [25–30]. Various other configurations of the *C*-type defects were found and

described together with reversible and irreversible switching between some of them [25, 30, 31].

At low concentrations, the *A*-type and *B*-type defects play negligible role during the growth of metal structures on the Si(100) surface, because they only act as blocking sites for adsorption and migration of the adatoms [32, 33]. However, if the concentration of the *A*-type and the *B*-type defects is very high, they will effectively block the growth of larger structures and consequently determine the character of the grown layer (e.g. the average size of island). The *C*-type defects, on the other hand, play an important role during the epitaxial growth of the Group III and Group IV metals [32–40], because of the two dangling bonds that are created upon their adsorption. These very reactive dangling bonds then act as nucleation centers for the growth of the nanostructures. The *C*-type defects can be in some cases the governing factor for the growth kinetics even if their concentration on the surface is low [34–36, 41]. Also freezing of the flip-flop motion of the Si dimers takes place in their vicinity.

### 2.1.2 Si(100) surface imaged by STM

The buckling of the dimers switches very fast compared to STM scanning speed at RT and the Si(100) surface reconstruction images as $(2 \times 1)$. The overall symmetric look of Si dimers at RT is sometimes distorted by the presence of a surface defect, in which case the buckling of the dimers can become "frozen" (recall the *C*-type defect in Subsection 2.1.1). Representative images of Si(100) surface at RT are shown in Figure 2.2(a)-(b). Imaging at negative sample voltage (filled states) visualizes the $\pi$ bonding states, the electron density of which is localized between the two Si atoms forming the dimer, and the bright rows in the filled states STM images correspond directly to the Si dimer rows. On the other hand, scanning at positive sample voltage (empty states) visualizes the anti-bonding states, the density of which is localized outside the Si dimer on its both sides. The bright rows in the empty states STM images then correspond to the trenches between the two neighboring Si dimer rows.

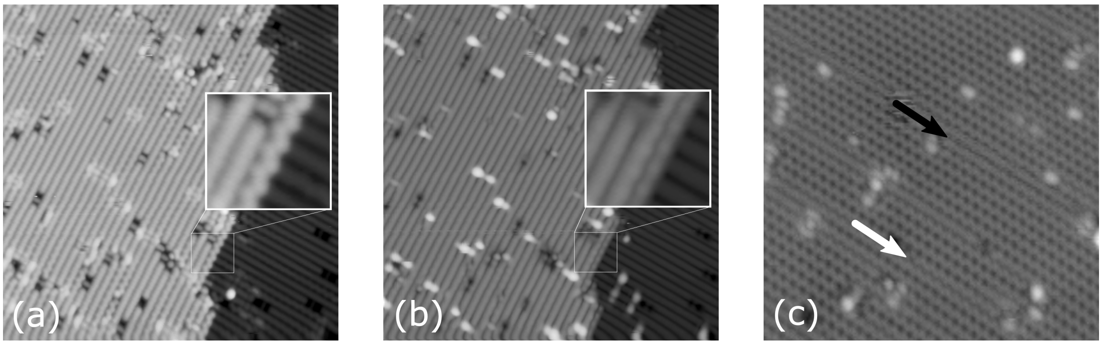

**Figure 2.2:** STM images of Si surface with Al at RT in (a) filled states and (b) empty states. The enlarged sections of the images show the difference in step imaging in the filled and empty states (c) Si(100)-c$(4\times2)$ surface with Al at 100 K. White arrow points to p$(2 \times 2)$ reconstruction while black arrow points to $(2 \times 1)$ reconstruction

Unlike in the filled states the frozen buckling of the dimers is not visible in the empty states images. At the step edges there is another difference of imaging in empty and filled states - the dimer rows in empty states are imaged as half-rows compared to the dimer rows within the terraces, whereas in the filled states the buckling of the dimers is frozen.

Cooling the surface below ≈ 200 K causes the freezing of the Si dimer buckling on the whole Si(100) surface. Even though the Si(100)-c(4 × 2) is the base reconstruction with the lowest total energy, depending on the scanning conditions (temperature, tunneling current, sample bias, sample doping, ...) there can appear in the STM images areas with other reconstructions [p(2 × 2), (2 × 1)]. It was shown that the appearance of the other reconstructions is probe-induced [42–44]. Figure 2.2(c) shows Si(100) surface at 100 K with the presence of several different reconstructions.

Since the buckling of the dimers can be frozen by the presence of the surface defects, the high density of the defects can also allow for imaging of small areas with p(2 × 2) or c(4 × 2) reconstructions at RT.

# 3. Growth of metal nanostructures on Si(100) surface

One of the reasons why the reconstructed Si surfaces are commonly used in electronic devices is their ability to serve as suitable templates for growth of various nanostructures. The character of the resulting nanolayers is largely defined by two groups of factors:

1. The growth conditions such as: deposition rate, the material coverage, surface temperature, etc.
2. The type of reconstruction in combination with the type of adsorbate, which determines not only the adatom hopping barriers, but also the interactions between individual adatoms and the structure/shape of the resulting nanostructures [e.g. 1-D atomic chains in case of Group III and Group IV metals on Si(100)]

The Si(100) surface has such a unique electronic structure that many species spontaneously self-organize themselves upon adsorption at coverages $< 0.5$ monolayer (ML[1]) into long atom-wide chains (nanowires). Typical species for which the self-assembly into the nanowires occurs are Group III and Group IV metals (In, Ga, Al, Sn, Pb, ...) [45–50]. The phenomenon was, however, observed even for organic molecules [51].

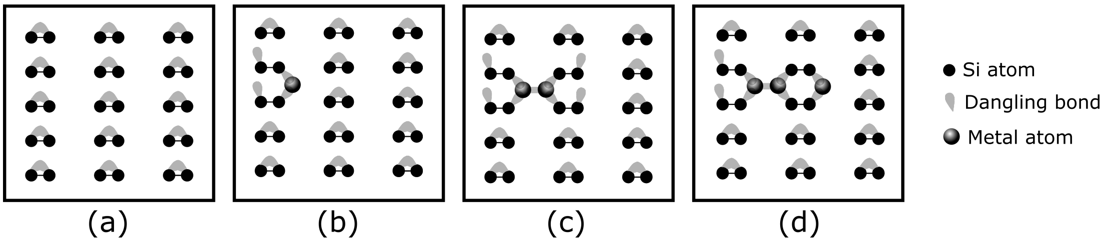

**Figure 3.1:** A simplified schema of the surface polymerization reaction.

A model describing the self-organized growth of nanowires was proposed by Brocks and Kelly [45] and it was called "surface polymerization reaction" based on its similarity with classic polymerization. Its mechanism is schematically shown in Figure 3.1(a)-(d) and it can be described as follows: Two metal adatoms migrating on the Si(100) surface have high probability of meeting each other and creating more stable object called dimer [Figure 3.1(c)]. Metal dimers originate in the trenches between Si dimer rows and every adatom within these dimers is bound to two neighbouring Si dimers. Creation of the metal dimer and its binding to the surface causes disruption of the $\pi$ bonds between Si atoms in all four participating Si dimers. The Si atoms within these four Si dimers which are not directly involved in the bonds with the metal dimer have 4 valence electrons at their disposal (each Si atom has 1 electron), which makes them more reactive than the rest of the surface. Thus, they further serve as nucleation centres for

---

[1] $1\text{ML} = 6.8 \times 10^{14}\text{atoms} \times \text{cm}^2$

other migrating metal adatoms. When another (the third) adatom is caught by this centre, it consequently serves as a new nucleation centre [Figure 3.1(d)]. After catching the fourth adatom, new metal dimer is created and the process starts over.

The growth of the metal chains saturates the Si dangling bonds and because of that the adsorption of additional metal adatoms in the direction perpendicular to the metal chains is possible at adsorption positions that are 2 lattice constants far away in that direction.

In the following two sections, there are presented generally known and accepted information about two metals studied in this thesis.

## 3.1 Sn on Si(100) surface

Electronic configuration of Sn atom in the ground state is $[\mathrm{Kr}]4\mathrm{d}^{10}5\mathrm{s}^{2}5\mathrm{p}^{2}$. During the process of the growth of Sn chain the atomic orbitals hybridize. It leads to creation of 4 half-filled $\mathrm{sp}^3$ orbitals per Sn atom. Two of the orbitals are used for creation of two $\sigma$ bonds with two neighbouring Si atoms. The other two orbitals dehybridize to orbital $(\mathrm{s} + \mathrm{p}_z)$ and orbital $(\mathrm{p}_x + \mathrm{p}_y)$. These orbitals participate on the creation of $\sigma$ and $\pi$ bond between the Sn adatoms and a metal dimer is formed. A filled $\pi$ bonding state and an empty $\pi^*$ anti-bonding state are the reason for the Sn dimers appearing as bright objects in the STM images in both filled and empty states (see Figure 3.2).

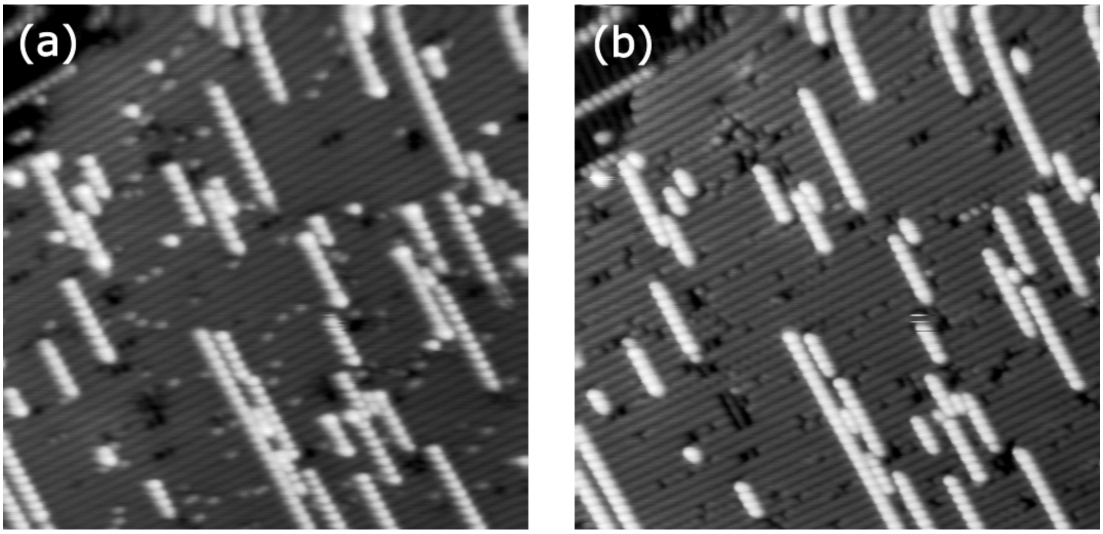

**Figure 3.2:** Typical STM images of (a) empty and (b) filled states of Sn chains grown on Si(100) at RT. $U_{\mathrm{S}} = \pm 1.5V$ and $I = 0.3$ nA

The published theoretical and experimental studies about the growth of the Sn nanostructures on the Si(100) surface focused mainly on the electronic and geometrical structure of the grown objects for coverages ranging from less then 0.5 ML up to 2 ML. The studies of the stability of the grown objects, hopping barriers of individual adatoms or their interaction with surface defects were more or less neglected topics. Only in [52] the authors refer to unpublished results that suggest an anisotropy of adatom hopping. The interaction of Sn adatoms with

$C$-type defects is briefly mentioned in [32], where the heterogeneous nucleation of Sn is said to be similar to In and Ga.

The studies of the electronic and geometrical structure confirmed that the growth of the Sn chains follows the surface polymerization reaction and that the monomer terminations are bounded to the chains enough to be observable by STM at RT [53]. Both experimental [53] and theoretical [54] investigations showed that the Sn dimers are buckled within the chains due to the same process that causes the buckling of Si atoms in the Si dimers – a charge transfer from the lower Sn adatom to the upper Sn adatom. It was further found that the Sn chains are composed not only of the buckled dimers, but also of combination of buckled and symmetric dimers [53]. There was no flip flop motion of the Sn dimers observed within the chains.

## 3.2 Al on Si(100) surface

The electronic configuration of Al atom in a ground state is [Ne]3s$^2$3p$^1$. During the process of the growth of Al chain the Al atomic orbitals hybridize which leads to creation of 3 half-filled orbitals per Al atom. The electronic configuration of the Al adatom within the dimer is very close to [Ne]sp$^2$sp$^2$sp$^2$3p$^1$. Two of the hybridized orbitals are used for creation of two $\sigma$ bonds with two neighbouring Si atoms. The third orbital remains unsaturated or can create a $\sigma$ bond with another Al adatom which results in forming a dimer. This leaves each Al adatom within the dimer with empty p orbital. Overlapping of these empty p orbitals creates an empty $\pi$ bonding state and an empty $\pi^*$ anti-bonding state. This is the reason why the Al dimers appear in STM images as bright objects in the empty states and are not that much pronounced in the filled states (see Figure 3.3).

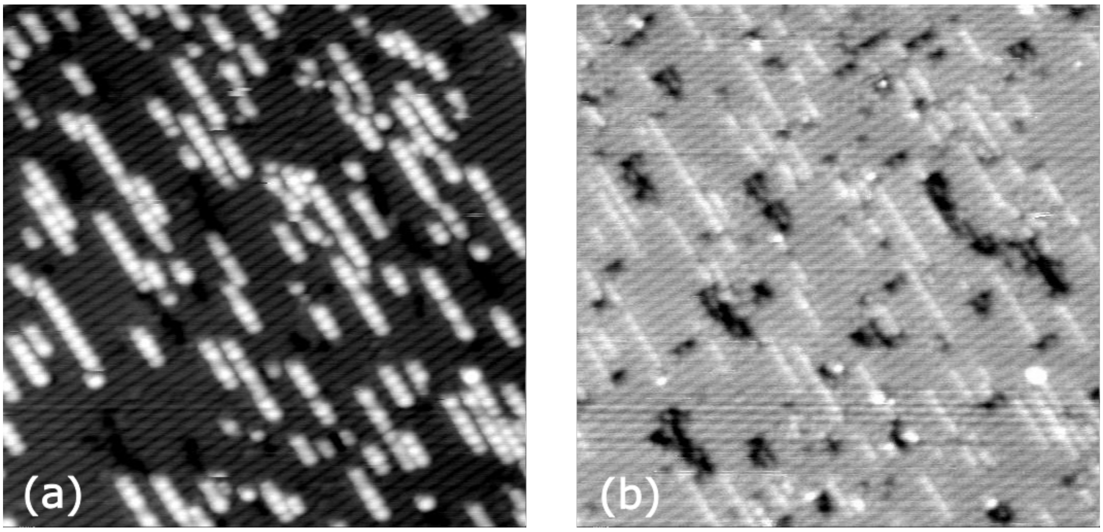

**Figure 3.3:** Typical STM images of (a) empty and (b) filled states of Al chains grown on Si(100) at RT. $U_S = \pm 2V$ and $I = 0.3$ nA. Notice the different contrast of the objects within the chains in the empty states and also branching of the chains.

Submonolayer Al coverages on the Si(100) were studied extensively in the past [45, 46, 48, 52, 55–59]. Even though Al belongs to a different metal Group than Sn, there exist a lot of similarities. Aluminium deposited on Si(100) at temperatures close to RT or higher (300 - 500 K) also self-assembles into 1-D chains with a parallel dimer structure via surface polymerization reaction [45, 55, 60, 61]. Since the p orbitals of the both Al adatoms within the dimer are empty upon the creation of the dimer, there is no charge, that can be transferred between the adatoms like in the case of Sn. Thus, the Al dimers are symmetric and there is no buckling of them.

More stable structures than dimers - clusters - are created upon heating the Al layer to higher temperatures. These clusters consist of a mixture of Al and Si adatoms. The most stable structures are the so called "magic clusters" that self-assemble into c(4 × 12) or (4 × 5) array at Al coverages of 0.5-1.0 ML that are heated to temperatures around 800 K [62–66].

## 3.3 Scaling theories

It is clear from the two previous sections about Sn and Al that the grown layers of different materials (as well as the layers of the same material grown at different experimental conditions) look different in STM images. Even though the layers can be described in qualitative terms - for example the brightens of the objects at different scanning voltages - to describe them in such a way that would allow for more systematic comparison, a set of quantitative metrics is needed.

Thin layers in the first phases of their growth, when there is on the substrate only few islands consisting of few adatoms, can be characterized by different statistical quantities called growth characteristics. The most commonly used growth characteristics are: average size of the island, density of the islands and island-size distribution function. These growth characteristics are unique for every investigated system.

While the characteristics "average size of the island" and "density of the islands" are quite self-explanatory, the term "island-size distribution function" requires more detailed explanation. In this section, we will explain this term and discuss what kind of information this growth characteristic can provide.

The main goal of different scaling theories [67–70] was finding a mathematical relationship (scaling) between some of the growth characteristics and parameters like material coverage $\Theta$ or ratio $\Re$ of diffusivity of adatoms to deposition rate. Solving a set of rate equations[2] with the following assumptions:

1. Only single isolated adatoms are mobile on the surface.
2. Desorption is negligible.
3. The coverage $\Theta$ is low.[3]

---

[2] Differential equations describing all the important atomic scale processes and time evolution of the density of islands $N(s)$ (i.e. the ratio of number of islands of the size $s$ to number of the adsorption sites) of all sizes.

[3] The expression "low coverage" is hard to quantify, because its value differs for various systems. The coverage of 0.05 ML can be, however, considered generally as small coverage for all systems.

4. A concept of a critical island of size $i$ is introduced.[4]

5. Islands with size $< i$ are in local equilibrium with adatom population.

an expression for the density of islands $N(s)$ at a given coverage $\Theta$ can be found:

$$N(s) = \eta(\Theta, i) \exp\left(\frac{E_i}{(i+2)kT}\right) \Re^{\chi} \tag{3.1}$$

where $E_i$ is the energy needed to disintegrate the whole critical island of size $i$, $\chi$ is defined by the size of a critical island and the geometry of the growth (1-D, 2-D, 3-D) and $\eta$ depends on the average geometry of the islands. An expression for the island size distribution that would allow for a comparison of layers grown under different conditions (e.g. different coverages) was found by Bartelt and Evans [68]. They studied a common case of thin layer growth by KMC. The object of their investigation was an isotropic and anisotropic irreversible growth without heterogeneous nucleation and with diffusion much higher then deposition. They proposed a relation for the island size distribution $N(s)$ in the form:

$$N(s) \approx \frac{\Theta}{\langle s \rangle^2} g\left(\frac{s}{\langle s \rangle}\right), \tag{3.2}$$

where the scaling function $g$ meets normalization conditions:

$$\begin{aligned} \int_0^\infty g(x)\mathrm{d}x = 1 \\ \int_0^\infty x g(x)\mathrm{d}x = 1 \end{aligned} \tag{3.3}$$

An example of the function $g$ that fulfills these conditions is an exponential decay $e^{-x}$. Other functions $g$ that fulfill these conditions for a given system can be analytically derived from solving the rate equations.

Since the function $g$ is independent on the coverage $\Theta$ [see equation (3.2)], the quantity $N(s)\langle s \rangle^2/\Theta$ plotted against $s/\langle s \rangle$ produces for one system the same function $g$ for different coverages $\Theta$ if the character of the growth is the same. For example Stroscio et al. reported the changes of function $g$ with varying substrate temperature during the homoepitaxy of Fe [71] and the changes were attributed to the variation of the size of the critical island.

The most important feature of the function $g$, which is exploited in this thesis, is its dependency on the parameters like detachment rates of adatoms from the islands, deposition rates or diffusion barriers. This dependency is introduced into the function $g$ through the rate equations and these kinetic parameters can be obtained by simulating the function $g$ to fit an experimentally obtained one. More information about our atomistic lattice-gas model and KMC simulations, which were used to simulate the growth of metals on Si(100) surface and consequently obtain the function $g$, can be found in Chapter 5.

In case of the system studied by Bartelt et al., it was shown that for small coverages the function $g$ has one well defined maximum around the value 1 (so

---

[4] The size of the critical island is such a size, at which all the additional adatoms do not detach from the island. For irreversible growth the size of the critical island is equal to 1

called monomodal shape) [68]. Their mathematical expression of function $g$ perfectly fitted the results of KMC simulations. More mathematical expressions of function $g$ for various growth mechanisms were derived by Vvedensky et al. [70].

Further studies showed that the scaling relation is valid even for more general systems (e.g. reversible growth [69]). It was also found that instead of the monomodal shape there are systems for which the function $g$ is monotonically decreasing [32, 39]. Current studies focus on the conditions at which the shape of the scaling function $g$ for various systems changes from monotonically decreasing to monomodal and vice versa [72–74]. In principle there are several reasons (and their combinations) for a system to exhibit a purely monotonically decreasing shape of the function $g$ or to exhibit an intermediate state between monomodal and monotonically decreasing shape:

1. A nucleation of new islands dominates over the attachment of the adatoms to already existing islands. This domination increases the population of the small islands at the expense of the larger ones. Typical example of such a case is fast deposition of material with relatively slow diffusion of the material on the surface.

2. The system finds itself at a state of thermodynamical equilibrium (TE) or at a state very close to it [75]. The reversibility of the growth (i.e. possibility of the detachment of the adatoms from the islands) brings the system closer to the TE even during the deposition. Even though Ratsch et al. [69] reported the monomodal character of the function $g$ for reversible growth, in their case the TE was definitely not reached, because the detachment of the adatoms from the islands was very slow compared to the speed of deposition together with the fact that the system was not allowed to relax after the end of the deposition. If the studied system is in a state of TE or close to it, the function $g$ no longer depends on any kinetic parameter. It contains only information about the interaction energy between the closest neighbours within the island [75]. Thus, no kinetic parameters such as diffusion barriers can be obtained form the function $g$ in this case.

3. The heterogeneous nucleation of the islands at surface defects can also cause the monotonically decreasing character of the function $g$ [41].

4. Strong anisotropy of the diffusion of the adatoms on the surface is another reason for the system to exhibit the monotonically decreasing character of the function $g$ [32, 33].

# 4. Experimental methods

## 4.1 Scanning tunnelling microscopy (STM)

### 4.1.1 Concise history

Achieving an atomic resolution in a microscope was for a long time an ultimate goal for many surface scientists. One of the first devices, invented by Erwin Wilhelm Müller in the year 1936, capable of such a resolution, was field emission microscope (FEM). Its construction contained sharp metallic tip, serving as cathode, placed into an evacuated chamber and a fluorescent screen as an anode [76]. The working principle of the microscope was based on applying high electric voltage between the electrodes in order to bend the energetic barrier around the tip. The bending of the barrier then enabled electrons near the Fermi level to tunnel through it and they were further accelerated by the applied voltage towards the fluorescent screen. The resulting image, however, represented more the crystallographic facets of the tip rather than individual atomic steps.

The same Erwin Wilhelm Müller who invented FEM succeeded in achieving true atomic resolution with his another invention from the year 1951 - field ion microscope (FIM). FIM can be viewed as a small modification of FEM. The polarity of the electrodes is exchanged and instead of vacuum the chamber is filled with inert gas (e.g. He [76]). The inhomogeneous electric field between the electrodes causes the polarization of He atoms that are further drawn towards the tip. Upon reaching the proximity of the tip the electrons from the He atoms tunnel into the tip. Loosing their electrons the He atoms become ions that are accelerated back toward the negatively charged screen. In comparison to the FEM, the principle of the FIM yields images that actually represent individual adatoms and atomic steps on the tip.

Even though the FIM allowed investigation of surfaces and real-time changes on it with atomic resolution, its application was unfortunately restricted only to sharp tips of refractive metals as W, Pt, Re, Pd, etc.. Using the crucial components of the FEM and the FIM - the sharp tip and the field emission - in a completely different setup, Russel D. Yung laid in 1971 foundations to a brand new family of microscopes [77]. The resolution of his topographiner (jointly due to the inability to sufficiently isolate the vibrations and the usage of field emission current) was in order of nm and thus unable to reach atomic resolution. However its working principle of a sharp tip that scans row by row an investigated surface and the usage of field emission current between tip and surface as a measured quantity made it the first scanning probe microscope (SPM) of this kind.

An immense scientific breakthrough came in 1982 when Gerd Binning and Heinrich Rohrer managed to measure the exponential dependence of the tunnelling current on the width of the vacuum gap between the tip and the sample [78]. When they later used the tunnelling current as a measured quantity during the scanning of a sample, their SPM became the first STM, which produced a resolution of the atomic steps on $CaIrSn_4(110)$ and Au(110) [79] and resolution of $7 \times 7$ reconstruction on Si(111) [80]. The Nobel Prize for them was only several years away at that time.

Despite all the great features that the STM provided, its main drawback was its limitation only to metallic and semiconducting samples. It took another 4 years (and it was again Gerd Binning) till another type of SPM, which did not require conducting samples, was invented - an atomic force microscope (AFM) [81]. The tunnelling current as the measured quantity was in this type of SPM replaced by a deflection of a cantilever with a mounted tip. Since its invention the AFM has undergone an astonishing number of improvements, at the end of which there are microscopes with the ability to resolve molecular backbones.

### 4.1.2 Basic principles

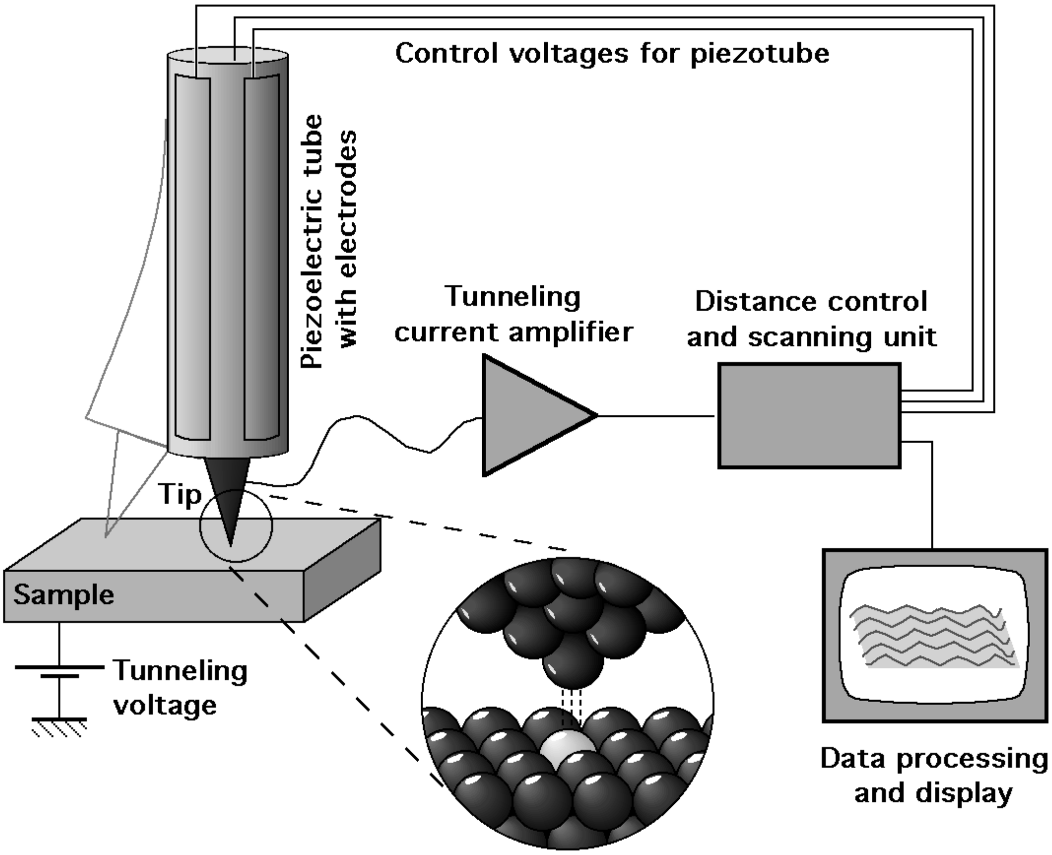

**Figure 4.1:** A schematic of operation of the STM [82]

A simplified schematic illustration of the STM and how it works is presented in Figure 4.1. After application of a bias voltage of several volts between a metallic tip and a conducting/semiconducting sample, the originally distant tip is slowly driven nearer to the sample until a preset value of tunnelling current, which starts to flow between the two electrodes is reached. Based on the polarity of the applied voltage the electrons tunnel either into the empty surface states or from the filled surface states. The flow of the desired tunnelling current usually happens within nanometers distance between the tip and the sample, which means that the tip and the sample are not in the direct contact. This makes the STM technique non-invasive, although a manipulation of objects on the surface is also possible. The tunnelling currents used for scanning are typically under 1 nA so they have to be amplified with an amplifier. After the preset tunnelling current is reached, the tip, which is usually mounted on a piezoelectric tube enabling movement of the tip in all three directions (X, Y, Z), then scans over the surface row by row.

Not only does the STM controlling computer visualize the measured data, but it also concurrently processes the information about the tunnelling current from the amplifier and steers the piezoelectric tube over the surface. This joint function of the computer allows for two distinct modes of measurement (see Figure 4.2):

- CONSTANT CURRENT MODE: In this operating mode the feedback loop is turned on, which means that while the tip hovers over the sample the preset value of the tunnelling current is kept constant by increasing the tip distance from sample where there is higher tunnelling current and reducing the distance in places with smaller tunnelling current. The result of this measurement is a height map of the tip. An indisputable advantage of this method is the protection of the tip from any collision with the investigated surface. A disadvantage of this mode is its relative slowness of scanning, which is limited by the speed of the feedback loop. But since a perfectly sharp tip is the most precious and the most fragile part of the microscope, its protection during the measurements makes this the preferred mode for the vast majority of the experiments.
- CONSTANT HEIGHT MODE: In this operating mode the feedback loop is turned off and the Z-coordinate of the tip is kept constants during the scanning, while changes of the tunnelling current are registered and presented in a form of map of variable tunnelling current. Since the scanning speed is no more limited by the speed of the feedback loop, this operating mode allowes for relatively fast scanning. It is, however, suitable only for flat surfaces, because with the disconnected feedback loop the tip is no more protected from collisions with the investigated surface.

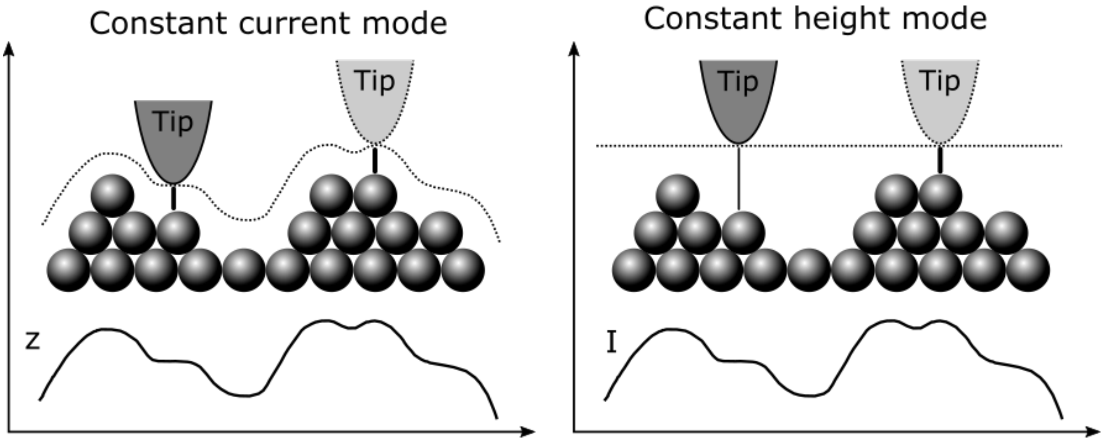

**Figure 4.2:** A schematic drawing of the two most usual operating modes of the STM. Whereas the constant current mode registers the changes in the height of the tip while keeping the current constant, the constant height mode scans in the constant distance from the sample while registering the changes in the tunnelling current.

The presented simplified images could have created a sense that the output of the STM is a morphological map of the surface. However, STM does not provide direct information about the type of adatoms or their exact positions on the investigated surface. Since the whole method is based on measuring electric current, the microscope actually maps the electronic structure of the surface intertwined together with the electronic structure of the tip. In the following sections we will provide a deeper insight into the physics behind the tunneling current in the STM and into the interpretation of the STM images.

### Tunneling effect and tunneling current

One of the extraordinary phenomenons, seemingly colliding with common sense, introduced by quantum physics was the ability of a particle to overcome a potential barrier even if the energy of the particle is lower than the height of the barrier. Something unthinkable in a classical physics is called tunnelling in quantum physics and it was practically used for the first time to explain the nature of radioactive decay [83].

The illustration of the tunnelling effect is presented in Figure 4.3(a). A particle with energy $E$ and mass $m$ finds itself in a region with zero potential energy (1) and is separated from another region with zero potential energy (3) by a potential barrier (2) of height $V_0$ and thickness $a$. The probability of tunnelling $T$ of the particle through the barrier (at condition $E < V_0$) can be expressed as [84]:

$$T = \left[1 + \left(\frac{V_0}{4\sqrt{E(V_0 - E)}}\right)\sinh^2\left(a\frac{\sqrt{2m(V_0 - E)}}{\hbar}\right)\right]^{-1} \tag{4.1}$$

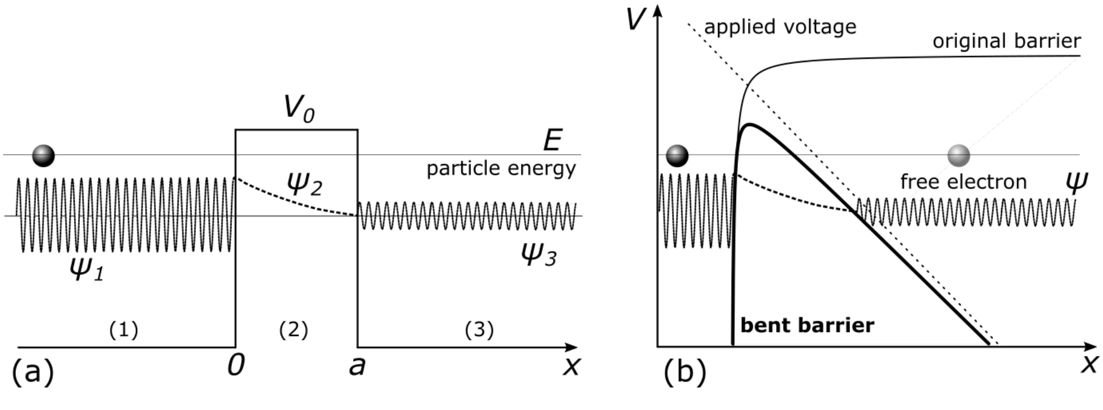

**Figure 4.3:** Tunneling of a particle through a potential barrier. (a) Idealized case of tunneling through a rectangular barrier of height $V_0$ and width $a$. (b) Tunneling through a bent energetic barrier in the vicinity of metal surface caused by application of external homogeneous electric field $\mathcal{E}$.

As basic as the tunnelling of the single particle through the energetic barrier may seem, it was and still is the crucial starting point in understanding the back bone of the STM - the tunnelling current.

Under the assumptions of Sommerfeld's model of metal, the electric potential $V$ in close proximity of the surface can be expressed as [85]:

$$V(x) = \frac{1}{4\pi\epsilon_0}\frac{e}{2x}. \tag{4.2}$$

Application of a homogeneous electric field $\mathcal{E}$ results in bending of the energetic barrier [see equation (4.3)], which would allow tunneling of the electrons through this barrier similarly to the already described special case of rectangular barrier [compare Figure 4.3(a) and 4.3(b)].

$$V(x) = \frac{1}{4\pi\epsilon_0}\frac{e}{2x} - \mathcal{E}x. \tag{4.3}$$

When the voltage $V$ is applied between two metal surfaces, which are brought sufficiently close together, the system is brought out of equilibrium, the energetic barrier between the surfaces is bent and electronic states in the metals are shifted apart by $eV$. As a consequence of this, electrons from occupied states of one metal start to tunnel through the bent barrier into the unoccupied electronic states of the other metal establishing a net current flow (see Figure 4.4). The current depends on several factors: the separation of the surfaces $z$, the shape of the electrodes (if they are not in a shape of flat surfaces) and the height of the barrier $\Phi$ (this can be roughly approximated by an average of the work functions $\Phi_1$ and $\Phi_2$ of the two metals). Despite all these apparent complications, the usage of JWKB method [86] yields an approximation of the tunnelling current $I_t$ in 1-D in a simple form [87]:

$$I_t = Vf(V)\exp\left(-z\sqrt{\frac{2m_e\Phi}{\hbar^2}}\right), \tag{4.4}$$

where $m_e$ is the mass of the electron and $f(V)$ is a function that describes the dependence of the tunneling current on the applied voltage and thus basically capturing the dependence of the current on the geometrical factors of the two electrodes.

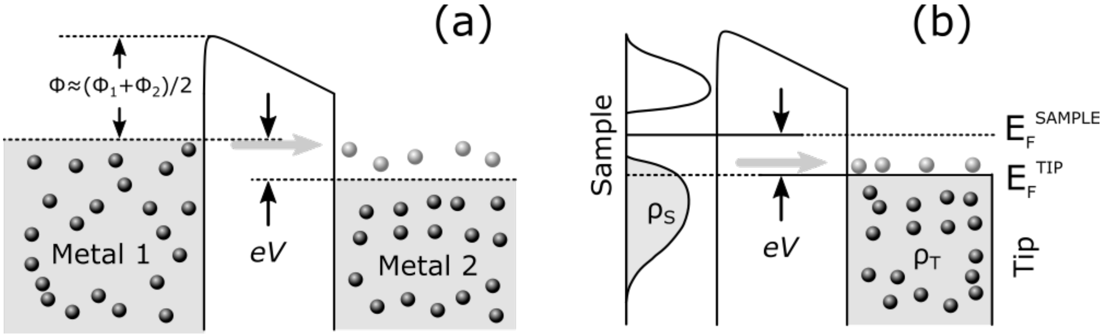

**Figure 4.4:** (a) A simplified schema of the tunneling current established between two metals after application of voltage $V$ between them. (b) The schema of tunneling current capturing its dependence on the density of states of the sample and the tip according to the equation (4.8).

Even though the equation (4.4) proves the exponential dependence of the tunneling current on the distance between the electrodes, it is far from sufficiently describing the experimental setups in the real world, where a sharp metal tip and planar sample with complex electronic structure are used as electrodes. Bardeen's approach, which makes use of the time dependent perturbation theory, can be used to derive more general formula taking into account the electronic structures of the tip and the sample [87]. The probability $P_{\mathrm{T,S}}$ of tunneling of an electron from a surface state $\psi_\mathrm{S}$ at energy $E_\mathrm{S}$ into a tip state $\psi_\mathrm{T}$ at energy $E_\mathrm{T}$ is given by Fermi's golden rule as:

$$P_\mathrm{T,S} = \frac{2\pi}{\hbar}|M_\mathrm{T,S}|^2\delta(E_S - E_T), \tag{4.5}$$

where $\delta$ is Dirac distribution and $M_\mathrm{T,S}$ is tunneling matrix, the elements of which can be expressed as:

$$M_\mathrm{T,S} = \frac{-\hbar^2}{2m_e}\int_S (\psi_\mathrm{S}^*\nabla\psi_\mathrm{T} - \psi_\mathrm{T}^*\nabla\psi_\mathrm{S})\mathrm{d}S, \tag{4.6}$$

where $S$ is a surface in the barrier region lying between the tip and the sample.

The tunneling current with applied voltage $V$ can be then obtained as the weighted sum of the combinations of the local densities of states (LDOS) of the sample $\rho_\mathrm{S}$ and the tip $\rho_\mathrm{T}$, where the weights are represented by equation (4.5):

$$I_t = \frac{4\pi e}{\hbar}\sum_\mathrm{T,S}[(f(E_\mathrm{T}) - f(E_\mathrm{S} - eV))]\rho_\mathrm{T}(E_\mathrm{T})\rho_\mathrm{S}(E_\mathrm{S} - eV)|M_\mathrm{T,S}|^2\delta(E_S - E_T), \tag{4.7}$$

where $f(E)$ is the Fermi distribution at energy $E$.

A simplification of the equation (4.7) can be achieved by approximating the Fermi distribution functions $f$ by step functions. The tunneling current can be then expressed as:

$$I_t = \frac{4\pi e}{\hbar}\int_0^{eV} \rho_\mathrm{T}(E_F + \epsilon)\rho_\mathrm{S}(E_\mathrm{F} - eV + \epsilon)|M_\mathrm{T,S}|^2\mathrm{d}\epsilon, \tag{4.8}$$

Figure 4.4(b) shows a simplified schematic representation of this equation.

### STM images

Considering that the mass of the electron $m_e$ is $9.109 \times 10^{-31}$ kg, the height of the barrier $\Phi$ is several units of eV and distance $z$ between the tip and the surface is several units of Å and substituting these values into the equation (4.4) shows that a change in the distance $z$ by 1 Å results into the change of the tunneling current by one order. This means that practically only the topmost atom on the tip is involved in tunneling and that even a macroscopically blunt tip can provide outstanding vertical resolution if there is a small cluster of several atoms at its apex. The quality of the vertical resolution is, however, limited by other factors: quality of vibration isolation, background noise, quality of the piezodrives, sensitivity of the current amplifier and the quality of the used electronics.

Whereas an excellent vertical resolution is achievable even with blunt tip, the lateral resolution is dependent on its sharpness. The sharp tip is a necessity for studying morphologically variegated surfaces, where the blunt tip would be unable to accurately map narrow trenches and small corrugations (see Figure 4.5).

As was already mentioned, the interpretation of the STM images is not straightforward. They do not simply show the geometric positions of individual adatoms. Under simplified assumptions of Tersoff-Hamann model [88], it can be concluded that the STM maps the corrugations of the LDOS of the sample

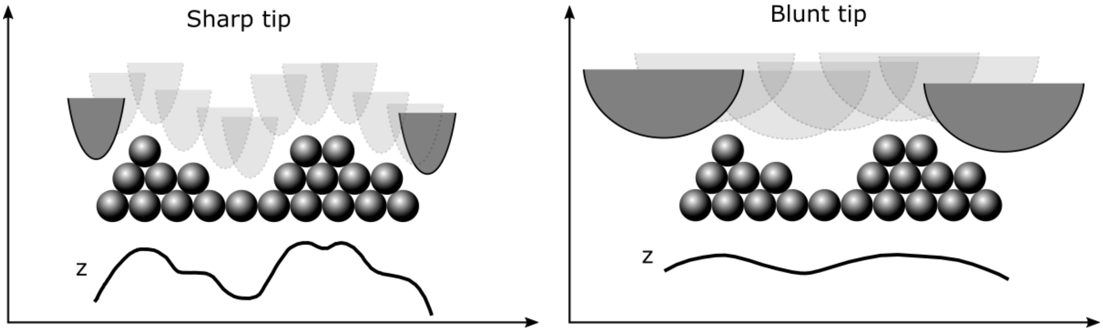

**Figure 4.5:** Schema of the impact of the sharpness of the STM tip on the lateral resolution of the final image.

at Fermi level. Usually the protrusions exceeding 1 Å show contours of underlying atoms (i.e. steps) whereas smaller protrusions are results of local electronic structure of the surface and adsorbate. Thus, not even an ultra sharp tip could provide better resolution in cases, where the electronic structure of the surface is homogeneous, and it is necessary to take utmost caution and care while interpreting the STM images. It is something that is sometimes impossible to do without the help of theoretical calculations or additional use of other surface methods (LEED, RHEED, XPS, etc.).

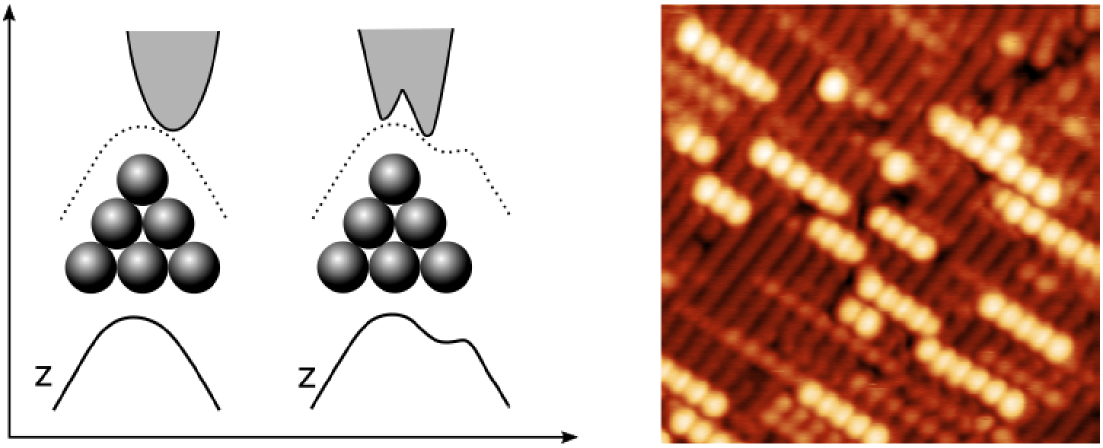

**Figure 4.6:** On the left there is shown a schema of how the ghost objects are created in the STM images because of the double tip. On the right there is an experimental image of Sn chains on Si(100)-(2 × 1) with visible ghost chains that arise from the double tip.

Apart from the complicated interpretation of the images caused by the very physical nature of the method, the images can be further distorted in other manners:

- Double tip: If the tip is not terminated with a single atom but with a small cluster of atoms that create multiple tips on the apex of the original tip, the resulting STM image may contain multiple ghost images of the scanned objects (see Figure 4.6). The most usual situation of multiple tip is that of a double tip. The ghost objects pose a real problem during the processing of the images not only when they are as pronounced as the original objects, but also when they are only faded duplicates of their originals. The ghosts can superimpose with their originals, with other objects (i.e. surface defects) or with other ghosts and thus smear crucial features of the investigated system making the correct interpretation of the observed structures extremely complicated if not utterly impossible.

- Drift: A thermal drift of the sample relatively to the tip is a consequence of the sample annealing at the beginning of the experiment. Together with the sample the surrounding parts of the microscope are heated as well and they cool down in the course of the experiment. This causes their expansion and shrinking, which further causes the lateral drift of the sample relatively to the tip. Even though the speed of the drift changes in time, in short time intervals (tens of minutes) it can be approximated with linear function. Thus it can be eliminated by superimposing linearly varying voltage to the voltage that controls the piezoelectric tube.

- Creep: The term *creep* is used to describe the deformation of the STM image caused by the plastic behavior of the piezoelectric tube. The deformation is the more severe the faster is the change of the position of the tip over the sample. In the case of large (approximately several tens of nm) and quick (approximately less than 1 s) changes of the tip position, the peizoceramics slowly creeps to the final position, causing logarithmic deformation of the image [89, 90]. The creep of the ceramics caused by intentional large change of the tip position can be eliminated by dividing the change to several small changes. If not prevented, this creep is usually of large magnitude and cannot be well defined and easily removed from the images. The creep of the ceramics caused by unintentional position changes that happen every time the tip returns from the end of last scanned line to the beginning of the first scanned line can be eliminated by incorporating a delay of several seconds between two consecutive image scans. This kind of creep is usually of small magnitude, constant and well defined across a longer sequence of scanned images. A relatively simple non-linear transformation of the images can be then used to remove the creep from them (see Figure 4.7). Our program that removes the creep from STM images can be found in [91].

### 4.1.3 Spectroscopy

One of the unique properties of the STM is the possibility of its usage for analysis and determination of energies of the surface electronic states both above and below the Fermi level. If we suppose that the tunnelling current can be described as a weighted convolution of the LDOS of the tip $\rho_{\mathrm{T}}$ and the sample $\rho_{\mathrm{S}}$, where the weight is the exponentially decreasing tunnelling probability expressed by equation (4.4), it can be then approximated by equation [92, 93]:

$$I(V) = \int_{E_{\mathrm{F}}}^{E_{\mathrm{F}}+eV} \rho_{\mathrm{S}}(E-eV)\rho_{\mathrm{T}}(E)\exp\left(-2z\sqrt{\frac{2m_e(\Phi+E_{\mathrm{F}}-E)}{\hbar^2}}\right)\mathrm{d}E \qquad (4.9)$$

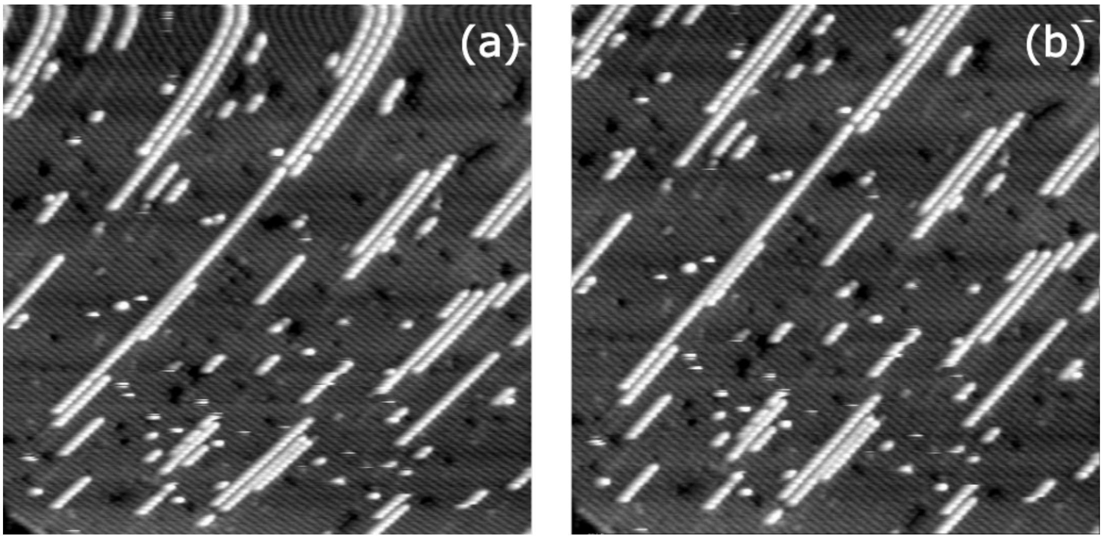

**Figure 4.7:** (a) A creep-deformed STM image of Sn chains grown on Si(100)-(2 × 1) surface at 350 K. The creep is caused by the regular movement of the tip from the bottom right corner to the top left corner after finishing one complete scan. (b) The same image after the non-linear transformation that removes the creep.

It can be deduced from the equation (4.9) that with increasing voltage $V$ the tunnelling current also increases as more of the electronic states participate in the tunnelling. Sharp rise of the current will happen when a peak in the electronic structure is reached. These changes can be measured in a form of a differential conductance normalized to conductance [see equation (4.10)], which has the advantage of suppressing the dependence of the measured characteristics on the tip-sample separation [92, 93]:

$$\frac{\mathrm{d}I/\mathrm{d}V}{I/V} \approx \frac{\rho_\mathrm{S}(eV)}{\frac{1}{eV}\int_0^{eV} \rho_\mathrm{T}(E)\mathrm{d}E} \tag{4.10}$$

If the electronic structure of the tip is similar to metal bulk, the denominator can be considered to be constant and measuring $\frac{\mathrm{d}I/\mathrm{d}V}{I/V}$ will yield the LDOS $\rho_\mathrm{S}(eV)$. The requirement of metallicity of the tip proves to be the biggest issue especially during experiments on non-metallic surfaces, because the tip can become contaminated with the substrate material. Spectra acquired with such a tip do not represent the real electronic structure of the sample, but carry non-negligible fingerprint of the electronic structure of the tip too. Also the existence of a band gap, charge transport limitations, band bending induced by the tip and other problems further complicate the scanning tunnelling spectroscopy (STS) measurements on non-metallic surfaces. Several works of Feenstra et al. [94–98] provide deeper insight into the STS measurements on non-metallic surfaces.

There are two basic approaches how to measurement the quantity $\frac{\mathrm{d}I/\mathrm{d}V}{I/V}$. The most simple and straightforward is the measurement of $I(V)$ characteristics and consequent numerical calculation of $\mathrm{d}I/\mathrm{d}V$. The numerical differentiation, however, amplify noise and the only way to suppress it is by averaging many datasets. The second method, although slower, complicated and requiring special equipment, uses lock-in amplifier which evaluates $\mathrm{d}I/\mathrm{d}V$ simultaneously with measurement of $I(V)$ characteristics and thus suppresses the noise implicitly.

### 4.1.4 Real-time monitoring of surface events

Throughout the past decades the STM proved to be an ideal experimental tool for studies of individual atomic-scale processes on surfaces. It was not only because of its inherent atomic resolution, but mainly because of the variability of experimental setups and scanning regimes, which the microscope offers. All of the various setups try to overcome the biggest limitation of the conventional STM image acquisition - the rate at which the atomic processes can be recorded. The suitable time resolution and elimination of undesirable interaction between the investigated adatoms and the tip were challenges that were successfully and variously solved by many researchers.

Repeated imaging of a selected surface area is the most conventional and straightforward experimental approach for achieving a recording of surface events with the time resolution given by the rate of the image acquisition [99–107]. Even though a video-rate of the image acquisition can be achieved [108], there are surface processes, which are confined to one dimension and which do not require full two-dimensional (2-D) scan. The rate of recording of dynamic processes happening in one line can be enhanced by about two orders of magnitude by utilizing a method of "line-scanning" [40], which was developed in our laboratory [34]. This method is based on repeated scans of the microscope tip over only one line of the investigated area.

Another method, which is not limited to 1-D processes and which enhances the recording rate of conventional STM method even more (by about three orders of magnitude), is adatom tracking [109, 110]. This method uses a lateral-positioning feedback which locks the STM tip above a selected adatom with sub-angstrom precision. After the STM is locked, it then tracks the position of the adatom migrating on the surface. The tunneling electrons may, however, influence the mobility of the investigated adatom during the whole time of the tracking.

If the adatom is confined in a small restricted area of several adsorption sites (e.g. half unit cell of the Si(111)-($7 \times 7$) surface reconstruction), the method of measuring the tunnelling current fluctuations at the STM tip position above a selected adsorption site can be used. The fluctuations of the current are responses to the presence/absence of the adatom in the tunnelling channel. Analysis of the current fluctuation (time-dependent tunneling spectroscopy) then provides the lifetimes of adatom at different adsorption positions [111, 112]. The tunneling conditions had to be carefully checked and investigated in order to minimize the tip-sample interactions.

The above listed methods enhance the recording rate by enhancing the time when the tip is above the investigated object. All of them are more or less sensitive to a good temperature drift compensation and the direct imaging of the whole area is sacrificed for the sake of higher recording rate. It is then impossible to be sure that the surface situation is still the same in the vicinity of the investigated objects.

Since the advent of low-temperature (LT) STM, some of the studies of the surface dynamics focused on slowing the motion of the adatoms by lowering the sample temperature rather than enhancing the recording speed of the microscope [40, 113]. This method provides the advantage of seeing the full scan of the area during the course of the whole experiment and thus gives a fuller image of the surface dynamics. Even though the time during which the tip locally influences the surface is not enhanced as in the aforementioned methods, the tip induced processes can become non-negligible in comparison with thermally activated processes, which are suppressed at the LT. Thus, the tip-sample interactions remain a great concern for this type of experiments too.

## 4.2 Experimental setup

### 4.2.1 STM

We used two different STMs for our experiments. Most of them (including the measurements at temperatures higher than RT) were conducted at the STM of our own design. The measurements that required cooling of the samples to LT were conducted at commercial STM: Omicron VT STM 045 P4535. All of the experiments were conducted under UHV conditions with base pressure better than $3 \times 10^{-9}$ Pa. This pressure not only ensured that the contamination of the studied surfaces - especially at LT - were kept at negligible level throughout the course of the experiment, but it also allowed for preparation of silicon surfaces by flash anneal procedure, which required pressures better than $1 \times 10^{-7}$ Pa.

### 4.2.2 Sample preparation

The Si(100) samples were cut from heavily Sb doped silicon wafers with resistivity $< 0.014$ Ωcm. Small sizes of the samples ($\approx 1.5 \times 8$ mm) were preferred since the heating of the surrounding parts of the microscope during the sample annealing was then reduced. Each freshly mounted sample was first resistively heated by DC current to the temperature of 600°C in order to be degassed at this temperature for two days. If the temperature during the degassing of the fresh sample exceeded the value of 660°C for an extended time period, the protective oxide layer was slowly removed, which resulted in roughening of the sample. This roughening was then irreversible [see Figure 4.8(a)]. After the slow degassing the sample was rapidly annealed (flashed) at the temperature 1200°C for several times in order to remove the protective oxide layer, expose the bare Si surface and create the $(2 \times 1)$ reconstruction. The flashes lasted usually 5-30 s with the first flashes being shorter and gradually becoming longer. It was crucial to keep the pressure in the chamber under $1 \times 10^{-7}$ Pa during the whole period of the flashes to prevent another irreversible roughening and spoiling of the sample surface.

Even though the preparation procedure of the Si(100)-$(2 \times 1)$ surface reconstruction is very simple, obtaining a virtually defect free surface with negligible concentration of *A*-type or *B*-type defects [see Figure 4.8(b)] requires special degassing procedure [114]. After initial degassing and annealing, the sample should be annealed for several days at temperature 900°C. The prolonged high temperature annealing requires the sample holder to be perfectly degassed as well in order to prevent any possible contamination of the sample. Although this procedure produces surfaces with minimal concentration of the defects, extensive heating results into a massive transport of Si over the sample, which causes the increased density of steps, shorter terraces etc. Thus, compromise between the defect concentration and the size of the terraces has to be found.

Having a sample with low concentration of the defects was of great importance for the most of our experiments that dealt with adsorption of metals on Si(100). Since it was proved that $C$-type defects play an important role during the growth of the submonolayers of Group III and Group IV metals [32–40], it was desirable to keep their concentration at minimum.

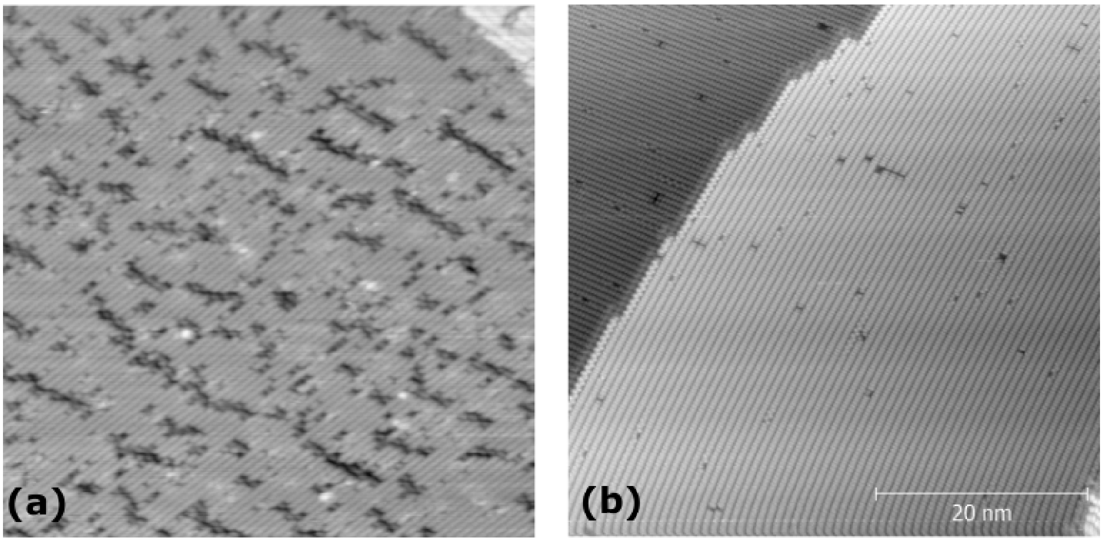

**Figure 4.8:** (a) Roughening of the Si(100) surface after inappropriate handling of the sample during preparation of the reconstruction. (b) Si(100) surface with extremely low concentration of the surface defects.

### 4.2.3 Metal deposition

All materials were deposited 1.5 hour after the flashing of the sample in order to let the sample and its surrounding cool down to RT and minimize the temperature drift during the scanning. The deposition differed based on the used material as well as on the used type of STM:

- STM OF OUR OWN DESIGN: The metals were evaporated from sources that were wrapped in resistively heated tungsten filament. The Sn was evaporated from a tantalum crucible and for Al a sapphire tube was used. Crystal thickness monitor located in the main chamber allowed for establishing of the deposition rates of both sources.

- OMICRON VT STM 045 P4535: Al was deposited from sapphire tube that was heated by electron bombardment. Since there was a problem reported for this kind of deposition concerning charging of the deposited atoms, we used the same solution as was reported in [113] - charged particles were separated from the beam of deposited atoms by an external magnetic field ($\approx 0.1$ T). There was no crystal thickens monitor present in this type of STM and thus all the experimental coverages had to be obtained ex post from the STM images.

### 4.2.4 Heating and cooling of the sample

For the experiments at temperatures higher than RT the samples were resistively heated. This approach leads to a voltage drop across the sample and the effective tunnelling voltage gap then depends on the geometrical position of the tip over the sample [see Figure 4.9(a)]. The numerical correction of the preset voltage has to be made to ensure the correct tunnelling voltage gap:

$$V_{\mathrm{gap}}^{\mathrm{eff}} = V_{\mathrm{gap}}^{\mathrm{set}} + V_{\mathrm{H}} \frac{l_{\mathrm{x}}}{l_{\mathrm{sample}}} \tag{4.11}$$

For the experiments at LT around 100 K a continuous liquid nitrogen flow cryostat was fitted to the STM with its heat exchanger ending several cm from the sample holder within the STM chamber [see Figure 4.9(b)]. Thermal coupling between the sample holder and the heat exchanger of the cryostat was achieved via copper braid clamped to both of them. The temperature was measured by cryostat temperature diode and stability of about 0.1 K was achieved after 1-2 hours.

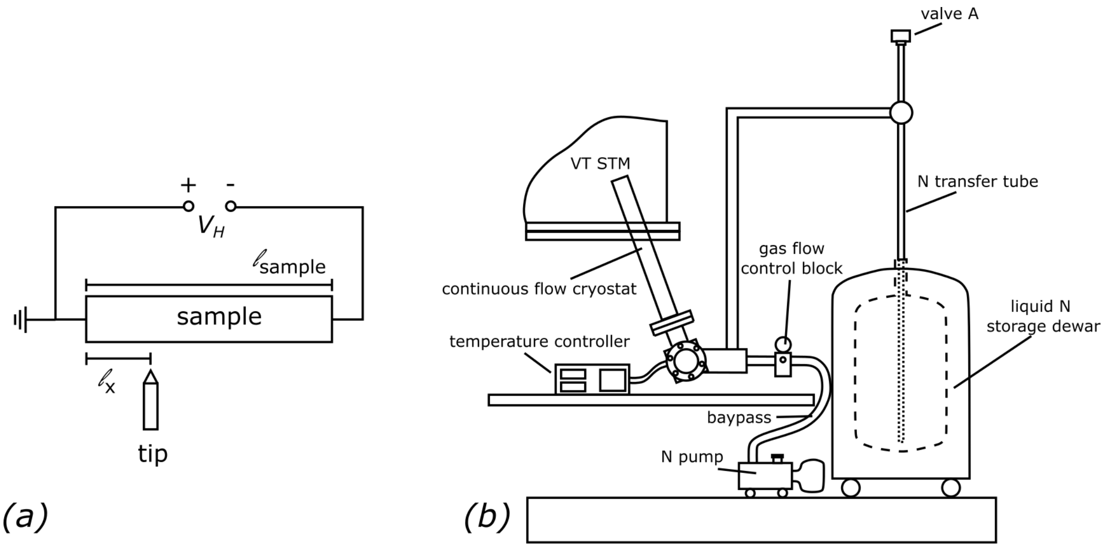

**Figure 4.9:** (a) A setup of direct heating of the sample by passing current. The geometrical position of the tip over the sample defines the voltage drop across the sample that has to be taken into account (b) Simplified schema of the setup of LT experiment using the liquid nitrogen flow cryostat.

# 5. Modeling methods

As was briefly mentioned at the end of Section 3.3, the growth characteristics of the real-life system can be compared with characteristics of a simulated one. Based on this comparison, the kinetic parameters of the real-life system can be in some special cases obtained. To achieve this goal the complex real process of the growth has to be reformulated into a more simple model, whose behaviour can be consequently simulated by KMC. In the following section, we introduce our lattice-gas model that tries to capture the key aspects of the migration of adatoms on the anisotropic Si(100) surface and growth of the chains via the surface polymerization reaction. This model, together with the KMC simulations, is used in this thesis to derive several kinetic parameters of the systems Sn/Si(100) and Al/Si(100).

## 5.1 Atomistic lattice-gas model

To simulate and subsequently investigate growth process of Group III and Group IV metals on the Si(100)-(2 × 1) surface a simplified atomistic lattice-gas model was developed based on the generally accepted experimental observations presented in Chapter 3. The Si(100)-(2 × 1) is represented by square lattice $N \times N$ of adsorption sites with periodic boundary conditions. The surface geometry is reflected by the model in the numbering of the columns of the square area. Two consecutive columns (even and odd - in this order) represent the adsorption sites between two silicon dimer rows. This way it is easy to distinguish between metal dimers (regular dimers formed in the surface trenches) and "bridge structures" (two adatoms bound over the surface dimer row - see Figure 6.18 in Section 6.2.1). The natural coverage of $C$-type defects is modeled by initial random denotation of several adsorption sites as immovable $C$-type defects.

The evolution of the system is modeled by the following events, features and restrictions (see Table 5.1 for additional details):

1. **Adsorption/Desorption.** The atoms are individually positioned on the random unoccupied adsorption sites of the surface at a given deposition flux $F$. If the randomly chosen site is occupied then the nearest free adsorption site is chosen by the means of a random walk. The deposition ends when the desired coverage $\Theta$ is reached. Desorption is not allowed in our model.

2. **Migration.** A free adatom will undergo an anisotropic migration on the Si surface with different rates in the parallel and perpendicular directions with respect to the Si dimer rows. It can hop in four directions: back and forth in parallel direction and back and forth in perpendicular direction. Our model simplifies the real-life situation by presuming the same energy barrier for the perpendicular hops between the Si dimer rows and for hops over the Si dimer rows. The anisotropy of the adatom migration is driven by the energy barriers for individual parallel hops $E^{\parallel}$ and perpendicular hops $E^{\perp}$. Adatoms can move only to the adsorption sites unoccupied by other objects (atoms, $C$-type defects).

3. **Unfavourable positions.** Experimental observations show that metal chain on Si(100)-$(2 \times 1)$ never grows on the adjacent side of another one and all chains are thus separated by a minimum distance of two lattice constants. To be consistent with this finding it is usual to implement into the model the forbidden zones (i.e. free adsorption sites to which the adatoms cannot move) around all objects in the direction parallel with silicon dimer rows [32, 39, 72, 73]. We believe that this strict rule limits the migration of the adatoms far too much. Thus we rather model these adsorption sites as unfavourable ones. It means that the adatoms are allowed to move to these positions, but to support their almost immediate leaving of this positions all the surrounding hopping barriers are lowered by a constant $E_{\mathrm{unf}}$.

4. **Nucleation.** The model allows for simulation of two types of nucleation.

    - Homogeneous: If two migrating adatoms meet each other at the adjacent positions in the direction perpendicular to the silicon dimer rows then they are bound together and form a nucleus for further growth of the chain. The strength of the bond depends on the position of the two adatoms. If they are both positioned within the same surface trench then they form regular dimer and the binding energy is $E_{\mathrm{DD}}$. If the two adatoms are positioned on opposite sites of the silicon dimer row then they form bridge structure and the binding energy is $E_{\mathrm{MM}}$.
    - Heterogeneous: If the migrating adatom visits an adsorption position, which is adjacent to a $C$-type defect on the opposite site of a silicon dimer row then the adatom is trapped by the defect and forms a nucleus for further growth of the chain. The binding energy is $E_{\mathrm{C}}$. The adsoprtion position on the other side of the $C$-type defect (in the same surface trench) is unaffected by its presence.

5. **Attachment/Detachment.** If a migrating adatom meets an end of an existing chain in the direction perpendicular to the silicon dimer rows then it is bound to it. The strength of the bond depends on the type of the chain termination. If the chain is terminated by a dimer then the binding energy is $E_{\mathrm{MD}}$ and the type of the termination changes to monomer. If the chain is terminated by a monomer then a new terminating dimer is formed and the binding energy is $E_{\mathrm{DD}}$. Detachment of adatoms from any position within the chain is allowed in the model. In order to detach, however, there must be a free adjacent adsorption position and the adatom must overcome on the one hand all the binding energies and on the other hand the migration barrier in the direction of the detachment. Thus the adatoms detach exclusively from the chains' terminations, because these adatoms have to overcome only one binding energy.

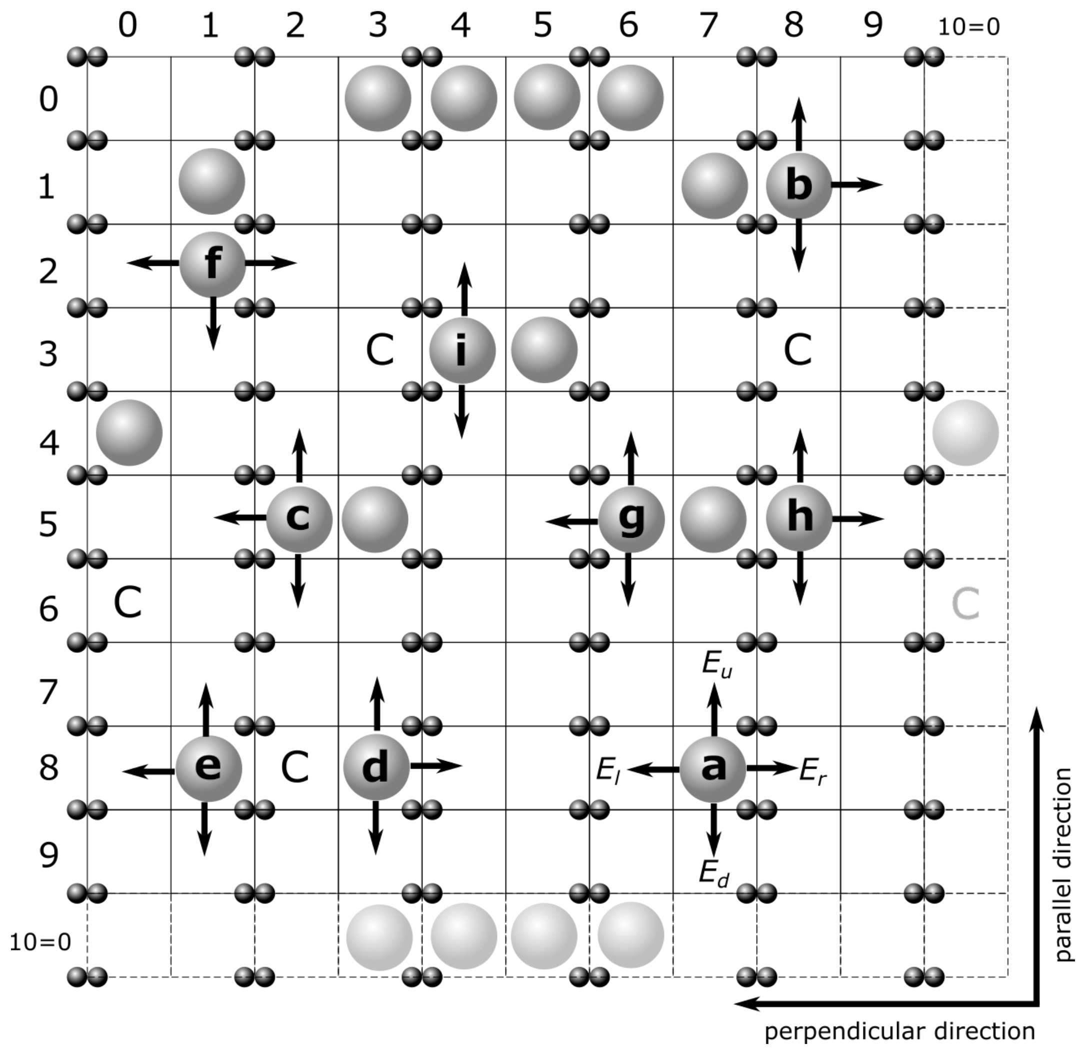

| | $\mathbf{E}_\mathrm{u}$ | $\mathbf{E}_\mathrm{d}$ | $\mathbf{E}_\mathrm{l}$ | $\mathbf{E}_\mathrm{r}$ |
|---|---|---|---|---|
| **a** | $E_a^{\parallel}$ | $E_a^{\parallel}$ | $E_a^{\perp}$ | $E_a^{\perp}$ |
| **b** | $E_a^{\parallel} + E_\mathrm{MM}$ | $E_a^{\parallel} + E_\mathrm{MM}$ | $\infty$ | $E_a^{\perp} + E_\mathrm{MM}$ |
| **c** | $E_a^{\parallel} + E_\mathrm{DD}$ | $E_a^{\parallel} + E_\mathrm{DD}$ | $E_a^{\perp} + E_\mathrm{DD}$ | $\infty$ |
| **d** | $E_a^{\parallel} + E_\mathrm{C}$ | $E_a^{\parallel} + E_\mathrm{C}$ | $\infty$ | $E_a^{\perp} + E_\mathrm{C}$ |
| **e** | $E_a^{\parallel}$ | $E_a^{\parallel}$ | $E_a^{\perp}$ | $\infty$ |
| **f** | $\infty$ | $E_a^{\parallel} - E_\mathrm{unf}$ | $E_a^{\perp} - E_\mathrm{unf}$ | $E_a^{\perp} - E_\mathrm{unf}$ |
| **g** | $E_a^{\parallel} + E_\mathrm{DD}$ | $E_a^{\parallel} + E_\mathrm{DD}$ | $E_a^{\perp} + E_\mathrm{DD}$ | $\infty$ |
| **h** | $E_a^{\parallel} + E_\mathrm{MD}$ | $E_a^{\parallel} + E_\mathrm{MD}$ | $\infty$ | $E_a^{\perp} + E_\mathrm{MD}$ |
| **i** | $E_a^{\parallel} + E_\mathrm{C} + E_\mathrm{DD}$ | $E_a^{\parallel} + E_\mathrm{C} + E_\mathrm{DD}$ | $\infty$ | $\infty$ |

**Table 5.1:** Schematic of the atomistic lattice-gas model. The Si(100)-$(2 \times 1)$ is represented by a square lattice $N \times N$ (in this example $10 \times 10$). Small black spheres represent Si atoms, large gray spheres represent metal adatoms and the letters C represent *C*-type defects. Additional column and row together with the pale spheres and letters are added to illustrate the periodic boundary conditions. Energy barriers for migration in four directions - up, down, left, right - are denoted respectively $E_\mathrm{u}, E_\mathrm{d}, E_\mathrm{l}, E_\mathrm{r}$.

Corresponding energy barriers for migration and detachment events described above are shown in Table 5.1 for the following situations: (a) A free adatom (b) An adatom bound in nucleus formed by two adatoms, which have met on the opposite sites of a silicon dimer row (c) An adatom bound in nucleus formed by two adatoms, which have met within the surface trench and consequently formed a dimer (d) An adatom trapped by a $C$-type defect on the opposite site of a silicon dimer row and consequently forming a nucleus (e) A free adatom, which is unaffected by the presence of $C$-type defect within the same surface trench (f) An adatom in an unfavourable position (g) A dimer termination of metal chain (h) A monomer termination of metal chain (i) An adatom within a chain that has to overcome binding energy to $C$-type defect and binding energy within the dimer in order to detach from the middle of the chain.

Additional simplification is introduced into the model by assuming the same frequency prefactor $\nu_0$ for all thermally activated processes.

## 5.2 Frequencies of individual actions

Correct evaluation and treatment of the frequencies of individual actions is the heart of any successful KMC simulation. In this section we present our approach to this problem.

The migration and detachment events are presumed to be purely thermally activated events with their rates $\nu$ obeying the Arrhenius relation:

$$\nu = \nu_0 \exp\left(\frac{-E_\mathrm{a}}{kT}\right), \tag{5.1}$$

where $E_\mathrm{a}$ is activation energy of the event, $k$ is Boltzmann constant, $T$ is temperature and $\nu_0$ is frequency prefactor.

In a simple 1-D situation of adatom being able to hop only in one direction (the other being blocked) with the energy barrier in the hopping direction being $E_\mathrm{barr}$, the activation energy for the hop is equal to the energy barrier and the frequency of hopping in this direction is defined by equation (5.1) and equal to

$$\nu = \nu_0 \exp\left(\frac{-E_\mathrm{barr}}{kT}\right). \tag{5.2}$$

If there are, however, more possible actions for the adatom to perform (e.g. hop backward, forward, upward or downward), then evaluation of the correct independent rate for each event is not straightforward. Since the individual possible actions exclude each other (the adatom cannot hop backward and forward in the same time) the frequencies of individual actions calculated by (5.1) are not simply additive and cannot be used as rates of the actions.

To prove it, let us consider a 1-D situation with adatom being able to hop backward and forward and the energy barriers in both directions being equal to $E_\mathrm{barr}$. Notice that in this case the height of the energy barrier is also the activation energy of leaving the adsorption site (no matter in which direction):

$$E_\mathrm{a} = E_\mathrm{barr}. \tag{5.3}$$

Evaluating the frequencies of backward (B) and forward (F) hops independently based on the equation (5.2) and simply adding them would result in the total frequency of leaving the adsorption site as:

$$\nu_{\mathrm{total}} = \nu_{\mathrm{F}} + \nu_{\mathrm{B}} = 2\nu_0 \exp\left(\frac{-E_{\mathrm{barr}}}{kT}\right). \tag{5.4}$$

If this frequency was correct, then the activation energy for leaving the adsorption site (no matter in which direction) calculated on the basis of equation (5.1) would be smaller than the energy barriers in both hopping directions and would violate the equation (5.3):

$$E_{\mathrm{a}} = -kT\ln\left(\frac{\nu_{\mathrm{total}}}{\nu_0}\right) = -kT\ln\left(2\exp\left(\frac{-E_{\mathrm{barr}}}{kT}\right)\right) = E_{\mathrm{barr}} - kT\ln(2). \tag{5.5}$$

Thus, to obtain the correct total frequency in case of more possible actions, the rates of the individual actions calculated by equation (5.2) have to be weighted by the probabilities of these actions. Since the probabilities are proportional to the rates of individual actions, the probability of occurrence of $i$-th action out of $n$ can be expressed as:

$$P_i = \frac{\nu_i}{\sum_{k=1}^{n}\nu_k}. \tag{5.6}$$

The correct total frequency is then equal to:

$$\nu_{\mathrm{total}} = \sum_{i=1}^{n}\nu_i P_i = \frac{\sum_{i=1}^{n}\nu_i^2}{\sum_{k=1}^{n}\nu_k}. \tag{5.7}$$

Next step is finding the correct frequencies of individual actions that are additive and preserve the proportionality of the original rates $\nu_i$. It can be concluded that the frequencies have to fulfill two conditions:

$$\begin{gathered} f_i = \mathrm{C}\nu_i, \text{ where C is constant } \forall i \\ \sum_{i=1}^{n} f_i = \nu_{\mathrm{total}} \end{gathered} \tag{5.8}$$

This form of relation ensures that the probabilities of individual actions calculated on the basis of new frequencies $f_i$ are the same as the probabilities calculated by equation (5.6). Using the equations (5.7) and (5.8) we can find the constant C:

$$\begin{gathered} \sum_{k=1}^{n} f_k = \nu_{\mathrm{total}} \\ \mathrm{C}\sum_{k=1}^{n}\nu_k = \frac{\sum_{i=1}^{n}\nu_i^2}{\sum_{k=1}^{n}\nu_k} \\ \mathrm{C} = \frac{\sum_{i=1}^{n}\nu_i^2}{(\sum_{k=1}^{n}\nu_k)^2} \end{gathered} \tag{5.9}$$

In case of 1-D situation with adatom being able to hop backward and forward, we obtain the correct additive frequencies as:

$$f_{\mathrm{F}} = \nu_{\mathrm{F}}\frac{\nu_{\mathrm{F}}^2 + \nu_{\mathrm{B}}^2}{(\nu_{\mathrm{F}} + \nu_{\mathrm{B}})^2} \qquad \text{and} \qquad f_{\mathrm{B}} = \nu_{\mathrm{B}}\frac{\nu_{\mathrm{F}}^2 + \nu_{\mathrm{B}}^2}{(\nu_{\mathrm{F}} + \nu_{\mathrm{B}})^2} \tag{5.10}$$

For already discussed case of $\nu_\mathrm{F} = \nu_\mathrm{B}$, the equations (5.10) give the following frequencies:

$$
\begin{aligned}
f_\mathrm{F} &= \frac{1}{2}\nu_\mathrm{F} = \frac{1}{2}\nu_0 \exp\left(\frac{-E_\mathrm{barr}}{kT}\right) \\
f_\mathrm{B} &= \frac{1}{2}\nu_\mathrm{B} = \frac{1}{2}\nu_0 \exp\left(\frac{-E_\mathrm{barr}}{kT}\right)
\end{aligned}
\tag{5.11}
$$

In another special case when $\nu_\mathrm{F} \gg \nu_\mathrm{B}$ or $\nu_\mathrm{B} \gg \nu_\mathrm{F}$, the equations 5.10 give:

$$
f_\mathrm{F} \to \nu_\mathrm{F} \qquad \text{and} \qquad f_\mathrm{B} \to \nu_\mathrm{B}. \tag{5.12}
$$

The more similar the energy barriers in backward and forward directions are, the more the correct frequencies differ from the rates of individual actions. This generally applies even to adatom migration with more possible hopping directions.

## 5.3 Kinetic Monte Carlo simulations

Monte Carlo simulation is a computational method, which relies on repeated random sampling to obtain numerical results and which can be used to solve any problem that has a probabilistic interpretation. It is thus suitable for simulation of the thin films' growth, because the processes that occur on the surface are thermally activated and as such are true random events.

In our simulations of the evolution of the lattice-gas model described in Section 5.1, we implemented the Bortz-Kalos-Lebowitz algorithm [115] to simulate the dynamics of the system. Namely the time intervals $\Delta t$ between individual actions were calculated as:

$$
\Delta t = \frac{-\ln(R)}{\sum_{i,k} f_i^k}, \tag{5.13}
$$

where $R$ is a random fraction chosen uniformly over the interval (0, 1) and $f_i^k$ is a frequency of action $i$ of adatom $k$. The adatom and its action that happened in the interval $\Delta t$ were selected as follows: A random variable $p$ was uniformly chosen over the interval $(0, \sum_{i,k} f_i^k)$. The adatom $K$ and its action $I$ for which the equations (5.14) were fulfilled were then chosen and the action of the adatom was executed. After each action all the frequencies $f_i^k$ were recalculated.

$$
\sum_{\substack{i=0\\k=0}}^{\substack{i=I\\k=K}} f_i^k \leq p \qquad \text{and} \qquad \sum_{\substack{i=0\\k=0}}^{\substack{i=I+1\\k=K+1}} f_i^k \geq p \tag{5.14}
$$

A full set of the model parameters that could have been tuned for each run of the simulation is listed in Table 5.2.

A single run of a simulation can be concisely described as follows: The simulation starts with random positioning of $C$-type defects on the surface with desired coverage. Then the deposition of individual atoms starts at a given rate together with their surface migration and growth of various structures. When the desired coverage of the adatoms is achieved, the surface system is let to further evolve (relax) for a given amount of time. An illustrative image of individual phases of the simulation are shown in Figure 5.1.

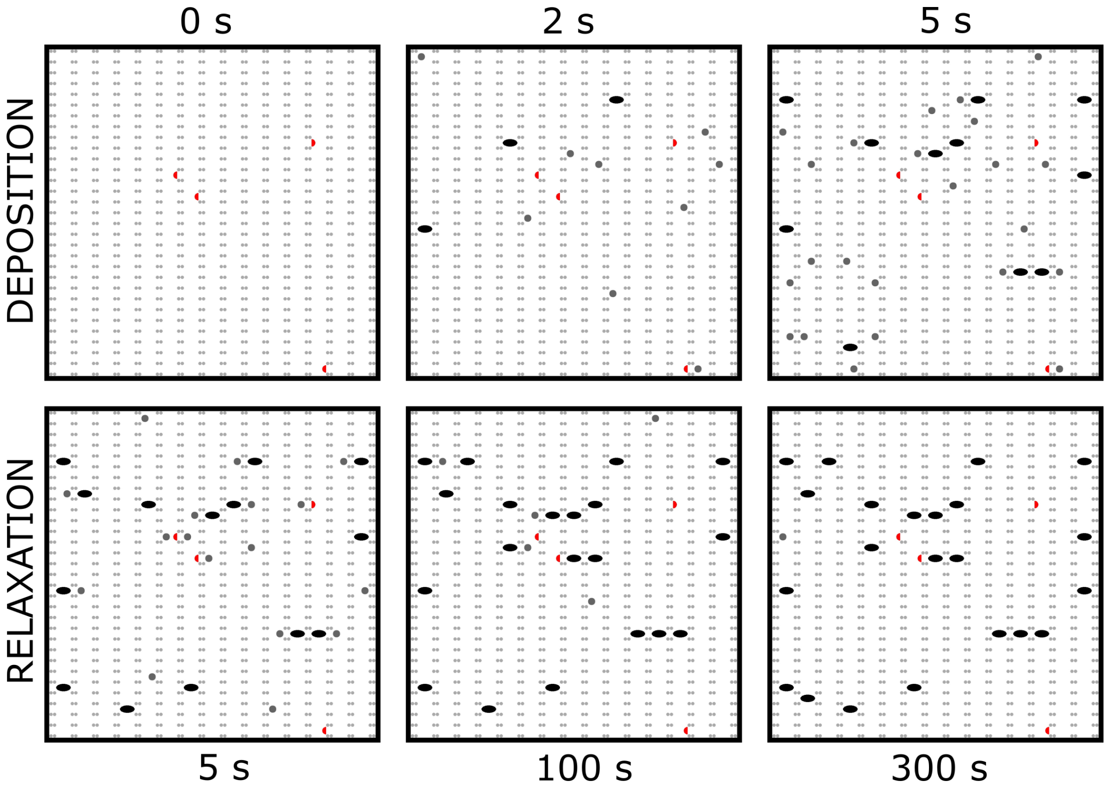

**Figure 5.1:** An example of KMC simulation process. The evolution of the simulation proceeds from left to right and top down. The simulation starts by covering the surface with $C$-type defects (red half circles). Then the deposition of atoms (gray disks) starts together with their migration on the surface and formation of dimers (black ovals) and growth of chains. After the desired amount of adatoms is deposited, the relaxation starts.
The parameters used in this example are: $T = 300$ K, $\Theta_{\mathrm{C}} = 0.005$ ML, $t_{\mathrm{A}} = 5$ s, $r_{\mathrm{A}} = 0.01$ ML/s, $t_{\mathrm{relax}} = 300$ s, $E_a^{||} = 0.7$ eV, $E_a^{\perp} = 0.7$ eV, $E_{\mathrm{DD}} = 1.07$ eV, $E_{\mathrm{MM}} = 0$ eV, $E_{\mathrm{MD}} = 0.8$ eV, $\nu_0 = 10^{13}$ $\mathrm{s}^{-1}$

| **Parameter name** | **Description** |
|---|---|
| $N_{\mathrm{row}}$ | Number of rows |
| $N_{\mathrm{col}}$ | Number of columns |
| $t_{\mathrm{A}}$ | Time of deposition of atoms |
| $r_{\mathrm{A}}$ | Deposition rate of atoms |
| $\Theta_{\mathrm{C}}$ | Coverage of $C$-type defects |
| $t_{\mathrm{relax}}$ | Time of relaxation |
| $\nu_0$ | Frequency prefactor |
| $T$ | Surface temperature |
| $E_a^{\|\|}$ | Energy barrier in parallel direction |
| $E_a^{\perp}$ | Energy barrier in perpendicular direction |
| $E_{\mathrm{DD}}$ | Binding energy in dimer |
| $E_{\mathrm{MM}}$ | Binding energy in intradimer |
| $E_{\mathrm{MD}}$ | Binding energy of monomer to dimer |
| $E_{\mathrm{C}}$ | Binding energy to $C$-type defect |
| $E_{\mathrm{unf}}$ | Repulsive energy of neighbours in parallel direction |

**Table 5.2:** A list of tunable parameters of the simulation.

# 6. Results

## 6.1 Tin on Si(100)

### 6.1.1 Sn chain length fluctuations on Si(100)-$(2 \times 1)$

The results of this subsection were published in: *Phys. Rev. B, 2017,* ***96****, 045430*

The growth of the metal chains on Si(100)-2 × 1 surface together with the deposition of the material is a lively process. The reversibility/iirreversibility of the growth (i.e. a possible adatom detachment from the chains) plays a major role in the growth scenario [37, 39, 41, 75]. If the growing process is reversible then during the deposition new chains are formed, new adatoms are attached to them and conversely adatoms detach from one chain and attach to another. The speed of this exchange of adatoms determines how far the system is from the equilibrium. In case of reversible growth the adatom exchange does not cease after the deposition, but continues even after the relaxation of the grown film. For a given temperature a dynamic equilibrium is finally reached where the lengths of the individual chains can vary in time due to the events of adatom attachment and detachment. The rates of these events depend on the temperature, but the overall growth characteristic of the system - chain length distribution - remains unchanged. All our following results are assumed to be obtained at these conditions of dynamic equilibrium.

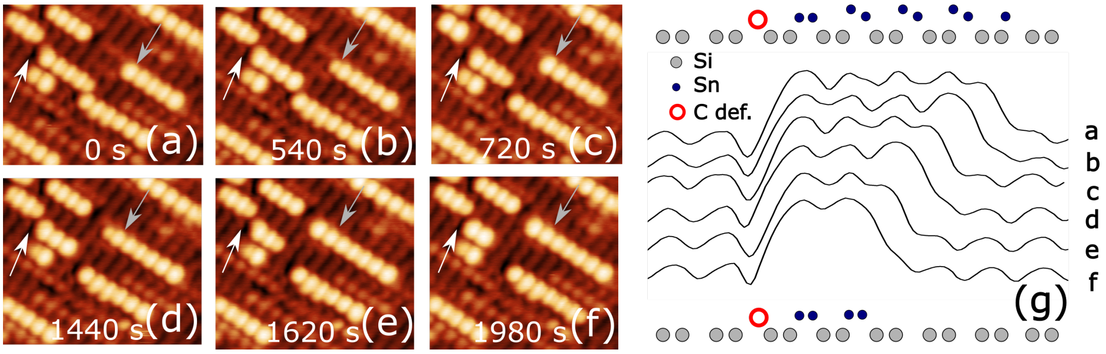

**Figure 6.1:** (a) - (f) An example of length evolution of Sn chains nucleated at a $C$-type defect (scanning parameters: 7.5 nm × 7.5 nm, 332 K, $U_s$ = -2 V, $I$ = 0.3 nA). (g) Line profiles of the chain marked by the white arrow. Buckling of dimers within the chain terminated by a monomer can be recognized. Faint traces of the chains in the images are caused by a double tip.

Figure 6.1(a)-(f) shows a series of STM empty states images with recorded process of exchange of adatoms among Sn chains grown on Si(100)-2 × 1 surface. A white arrow in the image points to a $C$-type defect at which one of the visible chains is anchored. The chain was chosen to demonstrate the gradual detachment of adatoms from its free end one by one. Attachment of adatoms to an existing neighboring chain is demonstrated in the images as well (marked by a gray arrow). The series of the images starts with the chain anchored at the $C$-type defect having length of 9 adatoms [see Figure 6.1(a)] and ended up with the same chain having length of 4 adatoms [see Figure 6.1(f)]. During this process the free end of the chain was alternately terminated by Sn monomer (further in text denoted as *odd* termination) and by Sn dimer (further in text denoted as *even* termination). Both terminations have in empty state images different appearance and can be easily distinguished. The even termination appears as a spot, which is brighter and have bigger radius than the spot representing the odd termination. On the right side of the Figure 6.1 a set of line scans of the investigated chain corresponding to its appearances in individual images (a)-(f) is provided. In agreement with the appearance of the odd and even terminations in empty state images, the profiles of the maxima corresponding to the even terminations are more pronounced than the maxima in case of the odd terminations. Above and below the profiles two schematic side views of the tin adatom arrangement are added. They correspond with the chain arrangement at the beginning of the series - odd termination - and with the chain arrangement at the end of the series - even termination.

The schematic side views also illustrate one interesting feature accompanying the presence of the odd termination observed in our experiments - a buckling of the dimers in the chain. The unbuckled dimer is observed in the STM images as a regular bright oval spot whereas the buckled dimer appears as a distorted version of the unbuckled one. The phenomenon of the dimer buckling in Sn chains at RT was observed and studied by Glueckstein et al. [53]. The presence of another chain in close vicinity of the investigated one was found to be the cause of the buckling. However, we have observed the dimer buckling even in chains well separated from the others, but with odd termination on one or both of its ends. A probable explanation of this observation is freezing of the thermal "flip-flop" motion of Sn dimers caused by the presence of the odd termination. Such a behaviour would be similar to the freezing of the thermal "flip-flop" motion of Si dimers on 2×1 surface in the presence of $C$-type defect. The thermal motion of Sn dimers within the chains has been studied by means of ab initio DFT calculations by Chan et al. [116] and a simulated STM image of Sn chains consisting only of dimers has been acquired. However the influence of the odd termination on the structure of the chain has not been investigated.

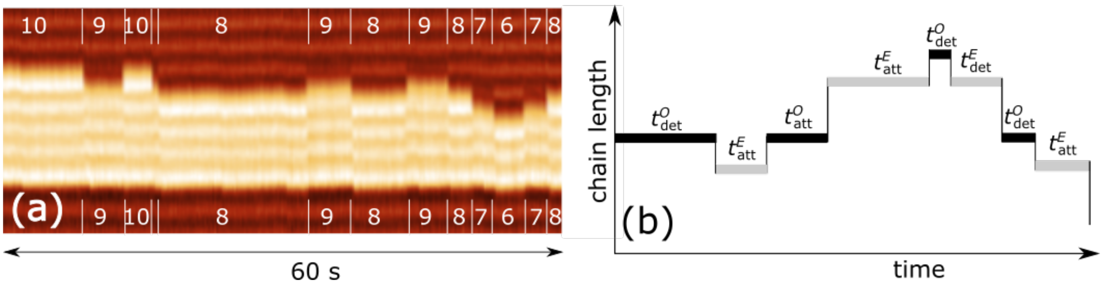

**Figure 6.2:** (a) An example of a line scanning measurement of a Sn chain at 326 K (scanning parameters: $U_s$ = -2 V, $I$ = 0.3 nA). To ease the recognition of the segments of different lengths, the white ticks are added to guide the eye. Where possible the lengths of the chain were added. The chain is nucleated on a $C$-type defect at its lower end. (b) A schematic drawing of the line scanning measurement with description of individual time segments.

To enhance the speed with which we have observed the variations of the chain lengths, we employed the line scanning method. Figure 6.2(a) shows an example of one line scanning measurement. The experiment spanned over a time period of 60 s during which 430 line scans over one investigated chain were recorded. The lower end of the chain was anchored at the $C$-type defect and the upper end was a free one. The recorded image was divided into segments of line scans where the length of the chain was unchanged. These segments are for better orientation highlighted by white ticks inserted into the image and also the unchanged lengths of the chain are added. The widths of the segments represent the lifetimes of the corresponding chain terminations. Reliable distinguishing of the changes of the length by 1 adatom (detachment or attachment) is mainly possible because of the change being distinctly visible in the images, but also because of the apparent transition between buckled and unbuckled dimer imaging between neighbouring segments when the termination of the chain is changed from even to odd and vice versa.

The evolution of the chain length is a sequence of two types of events - detachment of the adatoms from the ends of the chain and attachment of the adatoms to the ends of the chain. Result of each single event is not only the change of the length of the chain by 1 adatom, but also the change of the type of the termination (odd to even and even to odd). Thus, if we consider the detachment of the adatom from the chain being a thermally activated process, we have to introduce two different activation energies - one for each type of termination - $E_a^E$ for even terminations and $E_a^O$ for odd terminations. If we neglect the dependence of the activation energies on the length of the chain, the mean lifetime $\tau_{\mathrm{det}}$ of the chain termination can be expressed by formula:

$$\tau_{\mathrm{det}}^{O,E} = \frac{1}{\nu_0^{O,E}} \exp\left(\frac{E_a^{O,E}}{kT}\right), \tag{6.1}$$

where $\nu_0$ is the frequency prefactor, $k$ is the Boltzmann constant, $E_a$ is the activation energy for detachment and $T$ is temperature. The indexes $E$ and $O$ show if the expression corresponds to the even or odd termination.

If the detachment of the adatoms was the only process present or the attachment process was practically negligible (e.g. at very low coverages [34, 39]) the analysis and further statistical processing of the data would not be complicated. In such a case the mean lifetimes $\tau_{\mathrm{det}}^{O,E}$ of the chain terminations would be equal to a simple average of the measured time intervals $t_{\mathrm{det}}^{O,E}$ between two consecutive detachments:

$$\tau_{\mathrm{det}}^{O,E} = \left\langle t_{\mathrm{det}}^{O,E} \right\rangle \tag{6.2}$$

Closer look at the Figure 6.2 reveals, however, that this was not the case of our experiment. The attachment events were as frequent as the detachment ones. It was a direct consequence of the presence of other chains in close vicinity of the investigated one, because the attaching adatoms were the ones detached from these neighbouring chains.

The non-negligible attachment process has an experimental advantage - the "reservoir" of the detaching adatoms (i.e. the source of statistical data) represented by the chain is not depleted after several detachments, but is continuously supplemented with new adatoms that can later detach and provide the statistical data pool with additional values of the time intervals before detachment. The disadvantage of the attachment process is, however, the impairment of the pure detachment process. Only shorter detachment time intervals can be then observed. Before the longer detachment time interval is measured, an adatom is attached and the "seconds counter" is reset. Thus, simple averaging of the life times of terminations before detachment cannot be used to obtain time constants $\tau_{\mathrm{det}}^{O,E}$ and a complicated approach has to be employed. In order to determine the activation energies and frequency prefactors from the formula (6.2) a relation has to be found between the desired time constants $\tau_{\mathrm{det}}^{O,E}$ and the experimentally measured time intervals $t_{\mathrm{det}}^{O,E}$ influenced by the process of attachment.

As thermally activated processes with constant rates of occurrence $1/\tau_{\mathrm{det}}^{O}$ and $1/\tau_{\mathrm{det}}^{E}$ at given temperature, the detachment events of odd and even terminations can be described as two independent Poisson processes. The rate of attachment generally depends on the number of free migrating adatoms on the surface, which were detached from the chains in close vicinity of the investigated one. In the state of dynamic equilibrium, in which we assume that we have conducted our measurements, the number is on average constant and the rate of attachment $1/\tau_{\mathrm{att}}$ can be introduced. This rate also depends on the local character of the potential-energy surface around the termination. Different local conditions in the proximity of even termination and odd termination lead to introduction of two attachment rates - $1/\tau_{\mathrm{att}}^{E}$ and $1/\tau_{\mathrm{att}}^{O}$. We have thus introduced two additional independent Poisson processes. For the oncoming calculations, which can be performed independently for even and odd terminations, the upper indexes O and E will be temporarily dropped.

Based on the Poisson character of the processes the probability $P_0(t)$ that neither detachment nor attachment will change the termination of the chain in a time interval $(0,t)$ is given as:

$$P_0(t) = \exp\left[-t\left(\frac{1}{\tau_{\mathrm{det}}} + \frac{1}{\tau_{\mathrm{att}}}\right)\right] \tag{6.3}$$

The measured time interval, which ends by the event of detachment, when attachments have to be taken into account, can be described verbally as follows: the chain termination does not change in time interval $(0,t)$ and detachment occurs in time interval $(t,\Delta t)$ whereas attachment does not occur in this interval. Rewritten into mathematical expression of the probabilities:

$$\Delta P_{\mathrm{det}}(t) = P_0(t)\left(1 - \frac{\Delta t}{\tau_{\mathrm{att}}}\right)\frac{\Delta t}{\tau_{\mathrm{det}}}. \tag{6.4}$$

The corresponding probability density function is obtained as follows:

$$p_{\mathrm{det}}(t) = \lim_{\Delta t\to 0}\frac{\Delta P_{\mathrm{det}}(t)}{\Delta t} = \lim_{\Delta t\to 0} P_0(t)\frac{1}{\tau_{\mathrm{det}}}\left(1 - \frac{\Delta t}{\tau_{\mathrm{att}}}\right) = P_0(t)\frac{1}{\tau_{\mathrm{det}}}. \tag{6.5}$$

The probability density function of the event of attachment could be written as:

$$p_{\mathrm{att}}(t) = P_0(t)\frac{1}{\tau_{\mathrm{att}}}. \tag{6.6}$$

The derived probability density functions can be used to determine the mean lifetimes of chains' terminations before the event of detachment $\langle t_{\text{det}} \rangle$:

$$
\begin{aligned}
\langle t_{\text{det}} \rangle &= \int_0^\infty t p_{\text{det}}(t)\,\mathrm{d}t = \int_0^\infty \frac{tP_0(t)}{\tau_{\text{det}}}\,\mathrm{d}t = \int_0^\infty \frac{t}{\tau_{\text{det}}} e^{-t\left(\frac{1}{\tau_{\text{det}}}+\frac{1}{\tau_{\text{att}}}\right)}\,\mathrm{d}t \\
&= \begin{bmatrix} A = \left(\dfrac{1}{\tau_{\text{det}}} + \dfrac{1}{\tau_{\text{att}}}\right) \\ x = e^{-tA} \implies t = -\dfrac{\ln x}{A} \\ \mathrm{d}x = -Ae^{-tA}\,\mathrm{d}t = -Ax\,\mathrm{d}t \end{bmatrix} = \frac{1}{A^2\tau_{\text{det}}}\int_1^0 \ln x\,\mathrm{d}x \qquad (6.7) \\
&= \frac{1}{A^2\tau_{\text{det}}}(x\ln x - x)\bigg|_1^0 = \frac{\tau_{\text{det}}\tau_{\text{att}}^2}{(\tau_{\text{att}}+\tau_{\text{det}})^2}.
\end{aligned}
$$

And similarly for the mean lifetimes of chains' terminations before the event of attachment:

$$
\langle t_{\text{att}} \rangle = \frac{\tau_{\text{att}}\tau_{\text{det}}^2}{(\tau_{\text{att}}+\tau_{\text{det}})^2}. \qquad (6.8)
$$

Eventually the time constants corresponding to the detachment/attachment of adatoms from/to a chain termination can be obtained as:

$$
\tau_{\text{det}} = \frac{(\langle t_{\text{att}} \rangle + \langle t_{\text{det}} \rangle)^2}{\langle t_{\text{det}} \rangle},\ \tau_{\text{att}} = \frac{(\langle t_{\text{det}} \rangle + \langle t_{\text{att}} \rangle)^2}{\langle t_{\text{att}} \rangle}, \qquad (6.9)
$$

where the values $\langle t_{\text{det}} \rangle$ and $\langle t_{\text{att}} \rangle$ are the simple averages of the measured time intervals directly obtainable from experiments. In case of negligible or no attachment process at all (i. e. $\tau_{\text{att}} \gg \tau_{\text{det}}$ or $\tau_{att} \to \infty$) the equation (6.9) gives $\tau_{\text{det}} = \langle t_{\text{det}} \rangle$. This result of general equations is thus consistent with the result of the simplified case represented by equation (6.2).

Apart from the discussed complication of statistical data processing introduced by the presence of attachment process, there is another possible impairment of the data connected with the attachment, which has to be solved. Even though the line-scanning technique provides much faster recording speed (approximately 500×) than standard full image STM scanning, it can still be relatively slow in comparison with speed of some surface events (especially at room and higher temperatures). Accuracy of the results obtained statistically from experimental data depends on the assumption that the data contain whole information about the investigated processes. The line scanning method, however, provides data obtained by "sampling" the chain with limited time resolution and thus a possible leakage of information about the events at the ends of the chain has to be taken into account.

A false observation of no change of the chain termination - "zero event"- is a result of fast consecutive realization of two reverse events before the sample of the chain is taken. Three basic scenarios exist that lead to such a false observations (see also illustration in Figure 6.3):

1. A detached adatom returns and attaches back to the chain termination after a random walk on the surface.

2. A different adatom, which migrates on the surface, attaches on the place of a detached one.

3. Attached adatom quickly detaches and migrates away.

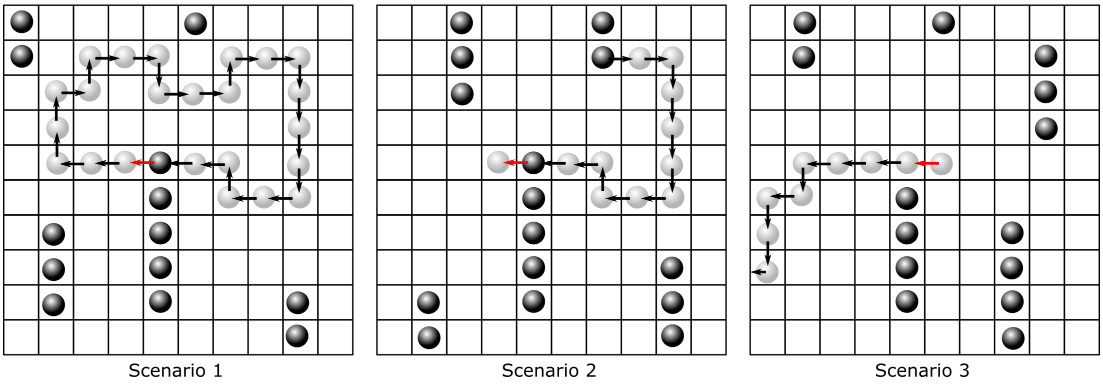

**Figure 6.3:** Examples of "zero events". Red arrow in the pictures represent the first action and black arrows represent the following actions reversing the first one. Mark the difference between Scenario 2 and 3. In Scenario 2 the detachment is missed whereas in the Scenario 3 the attachment of an adatom is missed.

The impairment of the experimental data caused by the latter two scenarios depends solely on the proportion of the values of the time constants $\tau_{\mathrm{det}}$ and $\tau_{\mathrm{att}}$ to the value of sampling speed ($\approx 0.14$ s/sample) and can be evaluated after the data processing. The extent of data impairment caused by the first scenario depends on the degree of thermally activated mobility of the Sn adatoms at room and higher temperature and on the concentration of the chain ends to which the randomly walking adatom can be attached instead of returning to its initial position. Even though the activation energies for shift of Sn adatom from one adsorption position to a neighbouring one has not been reported yet, a good approximation could be the activation energies measured and computed for group-III metals [52, 113], which is $\approx 0.35$ eV. This would mean $10^5 - 10^6$ random steps at room temperature in time between two line scans. Such a mobility is high enough to justify the assumption that if the detached adatom is not attached to another chain it always finds its way back to the original chain before the line scan is taken. In other words for the room temperature and higher the ratio of "zero events" could be considered temperature independent.

In order to evaluate the degree of the data leakage caused by this behavior, we first transformed the real-life situation into a simplified model. The Si(100)-$(2\times1)$ surface was represented by a square lattice and all the chains were modeled as point islands. To provide the point islands with a character of chains with two ends, a migrating adatom could attach to the existing island only from above or from below. At the beginning an adatom is detached from a selected island (it becomes its parent island). Then it is left to randomly walk on the square lattice until it attaches to one of the islands. If it attaches to its parent island and from the same direction from which it was detached, then it is considered as an observation lost due to the "zero event". If the adatom is captured by another chain or by its parent chain from opposite direction than the one from which it was detached, then it is considered as an observable detachment event. The schemes of the three mentioned types of random walk termination are depicted in Figure 6.4.

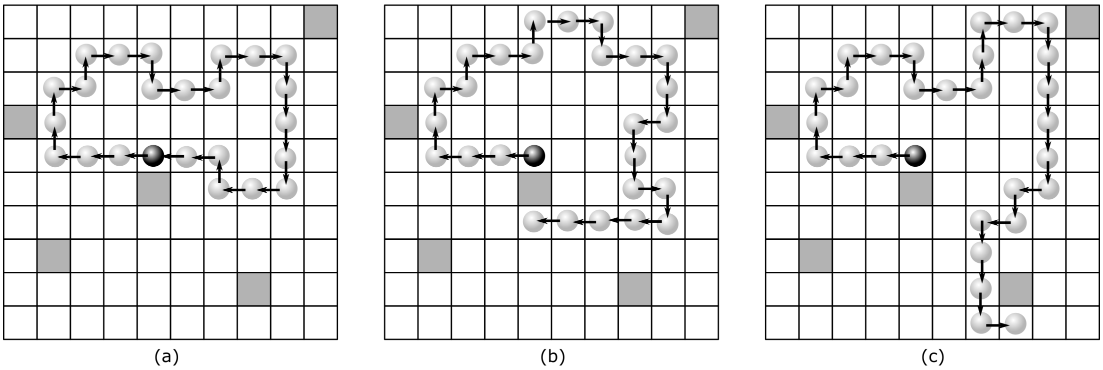

**Figure 6.4:** Schematic pictures of 3 possible terminations of random walk of a detached adatom. (a) "Zero event" - adatom attaches back to its original adsorption position (b) Observable detachment event - adatom attaches to the opposite end of the chain (c) Observable detachment event - adatom attaches to another chain.

We used Monte Carlo simulations to estimate the ratio of "zero events" to observable events. The size of the square lattice together with the concentration of the point islands were the two free parameters of the simulations. The number of the runs of the simulations was chosen as 10 000, because above this number the fluctuation of the results was negligible. The outcome of the simulations showed that 70% of the detachment events end as unobservable for the free parameters set to values corresponding to our experiments (area size 100 × 100 and chains' ends concentration 0.1%). This number is almost independent on concentration of capturing islands and is practically independent on the size of the area for sizes 50 × 50 and larger. As a result we could not neglect the "zero event" data leakage caused by the first scenario. We have missed on average two out of three detachment events, which means that the time intervals and corresponding time constants should be three times shorter.

Because the equation (6.1) can be rewritten in a form:

$$\ln \tau_{\text{det}}^{O,E} = \frac{1}{T}\frac{E_a^{O,E}}{k} - \ln \nu_0^{O,E}, \tag{6.10}$$

obtaining $\tau_{\text{det}}^{O,E}$ for different temperatures allows for concurrent evaluation of activation energy $E_a^{O,E}$ and frequency prefactor $\nu_0^{O,E}$ via a linear regression of dependency of natural logarithm of measured time constants on reciprocal temperature. Because of the temperature independence of the "zero event" ratio, the impairment of the time constants for all temperatures by constant factor $\frac{1}{3}$ will result into the real $\nu_0$ being 3 times higher than the measured one.

We preformed measurements of chain length fluctuation at seven different temperatures. To estimate and possibly eliminate the influence of the tunneling conditions on the observed processes, we performed experiments for three different values of sample voltage and for two different values of tunneling current. These comparative experiments were executed at three lowest temperatures from the seven. Line scans of various chains recorded at the same temperature and with the same tunneling conditions were converted into time series of attachment-detachment events. For almost each set of the conditions and each type of the

Odd termination

| $T$ (K) | $\langle t_{\mathrm{det}} \rangle$ (s) | | $\tau_{\mathrm{det}}$ (s) | $\langle t_{\mathrm{att}} \rangle$ (s) | | $\tau_{\mathrm{att}}$ (s) |
|---|---|---|---|---|---|---|
| 313 | 7.13 | → | **14.90** | 3.18 | → | 33.47 |
| 317 | 3.58 | → | **8.09** | 1.80 | → | 16.06 |
| 326 | 2.62 | → | **5.03** | 1.01 | → | 13.04 |
| 332 | 1.63 | → | **2.48** | 0.38 | → | 10.53 |
| 337 | 0.67 | → | **1.49** | 0.33 | → | 3.03 |
| 342 | 0.37 | → | **0.53** | 0.07 | → | 2.69 |
| 349 | 0.19 | → | **0.24** | 0.02 | → | 1.96 |

Even termination

| $T$ (K) | $\langle t_{\mathrm{det}} \rangle$ (s) | | $\tau_{\mathrm{det}}$ (s) | $\langle t_{\mathrm{att}} \rangle$ (s) | | $\tau_{\mathrm{att}}$ (s) |
|---|---|---|---|---|---|---|
| 313 | - | → | - | - | → | - |
| 317 | 9.76 | → | **54.39** | 13.28 | → | 39.97 |
| 326 | 4.05 | → | **12.54** | 3.08 | → | 16.49 |
| 332 | 2.35 | → | **9.11** | 2.28 | → | 9.39 |
| 337 | 1.09 | → | **4.35** | 1.09 | → | 4.37 |
| 342 | 0.83 | → | **2.89** | 0.72 | → | 3.35 |
| 349 | 0.60 | → | **2.34** | 0.59 | → | 2.39 |

**Table 6.1:** Table of values of mean lifetimes obtained from measurements at various temperatures. The corresponding calculated time constants are also included.

termination about 200 time intervals were obtained and processed. Mean lifetimes of chain terminations before attachment $\langle t_{\mathrm{att}}^{O,E} \rangle$ and detachment $\langle t_{\mathrm{det}}^{O,E} \rangle$ were then calculated and equation (6.9) was subsequently used to evaluate the time constants $\tau_{\mathrm{att}}^{O,E}$ and $\tau_{\mathrm{det}}^{O,E}$. Both the measured mean lifetimes of the chains' terminations and the corresponding time constants obtained at non-intrusive tunneling conditions are shown in table 6.1.

We see that the time constants for detachment and attachment are for all temperatures distinctly higher than the time needed to acquire one line scan. The above mentioned impairment of the experimental data caused by the last two scenarios of "zero event" can be thus neglected, because their time scale is much higher than the time scale of the sampling.

Figure 6.5(a)-(b) shows a temperature dependence of time constants for detachment of odd and even terminations. The dependence for odd terminations [see Figure 6.5(a)] displays a clear Arrhenian behavior for all tunneling conditions used in the experiments in the whole measured temperature range. Time constants for detachment of adatoms from even terminations show also Arrhenian behavior in the whole temperature range, but only for a sample voltage of $-2$ V. If the polarity of the tunneling voltage is changed ($+2$ V), the Arrhenian behavior of time constants remains only above 325 K. Below 325 K the values of time constants are temperature independent. Such a behavior indicates that at these conditions the process of even termination detachment is mainly controlled by a mechanism that is dependent on tunneling conditions and not thermally activated. If the mechanism was modification of the energy barrier height caused by the presence of the tunneling voltage, the resulting process would still show Arrhenian behavior. A preferred explanation is a process of electrons tunneling into the empty states and releasing energy during their thermalization. An example of similar competition between tip induced and thermally activated events was observed during investigation of mobility of individual indium adatoms on Si(100) surface at very low temperatures [113].

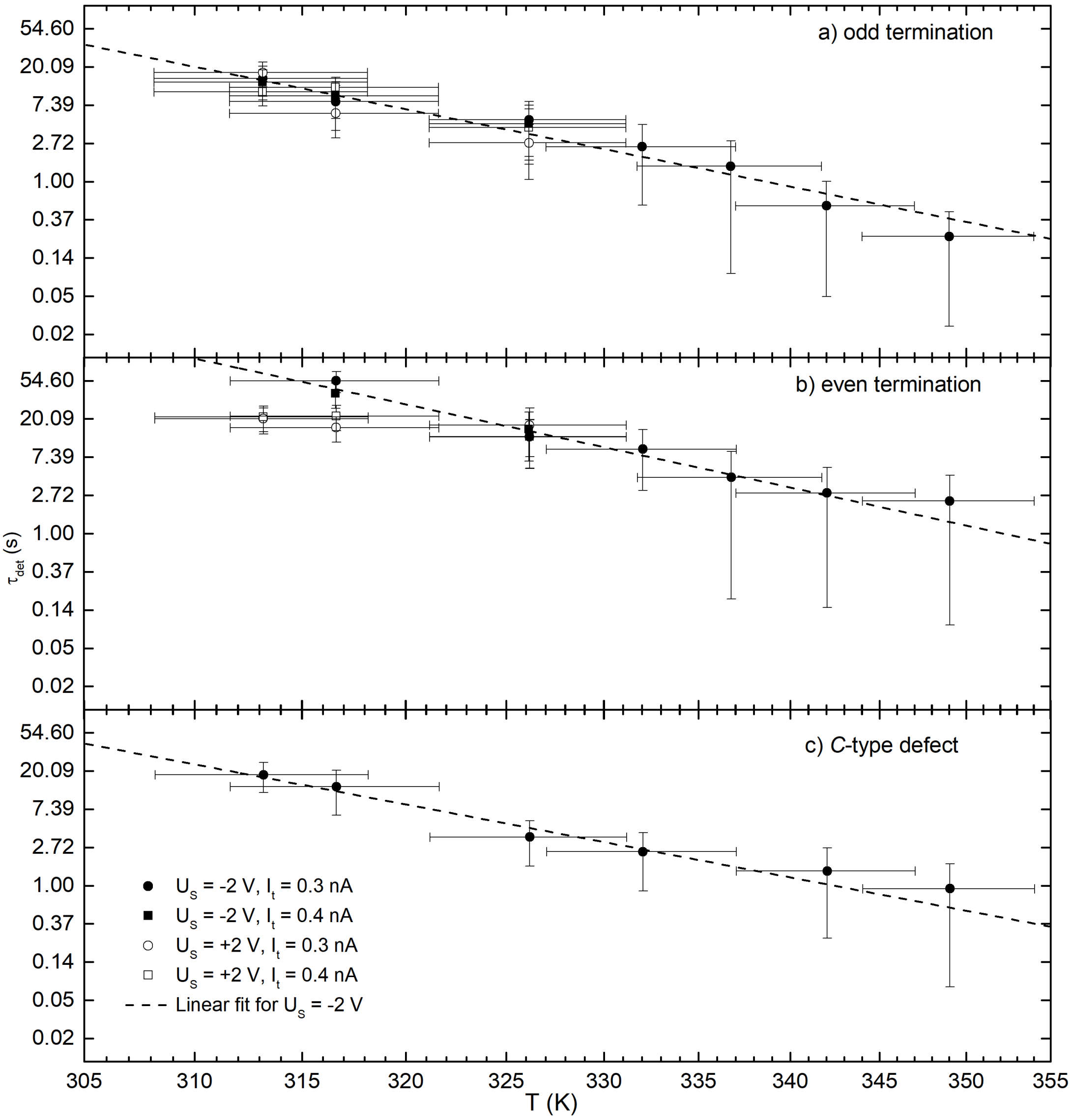

**Figure 6.5:** Temperature dependence of time constants on various scanning conditions for different chain terminations. (a) Odd termination (b) Even termination (c) *C*-type defect. The temperature axis is in a reciprocal scale.

We used the equation (6.10) for fitting the temperature dependencies of time constants in order to obtain the activation energies and frequency prefactors for the detachment of adatoms from odd and even terminations. Only the portions of the dependencies for which the detachment could be considered thermally activated were fitted. A linear function weighted by the uncertainties of the measured time constant was used. The following values, which take into account the "zero event" correction, were derived:

$$\begin{aligned} E_a^O &= (0.88 \pm 0.08)\ \text{eV} \qquad \nu_0^O = 3 \times 10^{13\pm1}\ \text{s}^{-1} \\ E_a^E &= (1.02 \pm 0.08)\ \text{eV} \qquad \nu_0^E = 3 \times 10^{14\pm1}\ \text{s}^{-1} \end{aligned} \tag{6.11}$$

The results show that an adatom at even termination (i.e. adatom, which is part of a dimer) is bound more strongly to the chain in comparison with the adatom at odd termination. The difference in activation energies is 0.14 eV. The only reported data, with which we can compare our results, are DFT calculations concerning another group-IV metal — Pb [117]. It was showed in the paper that the adsorption energy of a Pb chain terminated by a dimer is higher by less than 0.1 eV than adsorption energy of chain with monomer termination. Moreover it was shown that the difference is practically independent on a chain length, from which we derived one of our assumptions for Sn for the processing of the experimental data.

In course of our experiments, it was found out that $C$-type defects act as nucleation centers also for Sn chains. This finding is illustrated in Figure 6.6, where a sequence of STM images of the same area taken at 350 K is shown. The white arrow points to a position of one investigated $C$-type defect. The sequence starts with a plain $C$-type defect to which several adatoms are attached in the following snapshot. Sn adatoms further attach to and detach from the free end of the chain until there again remains only the $C$-type defect. Then a migrating adatom is "trapped" by it and evolution of a new chain starts over.

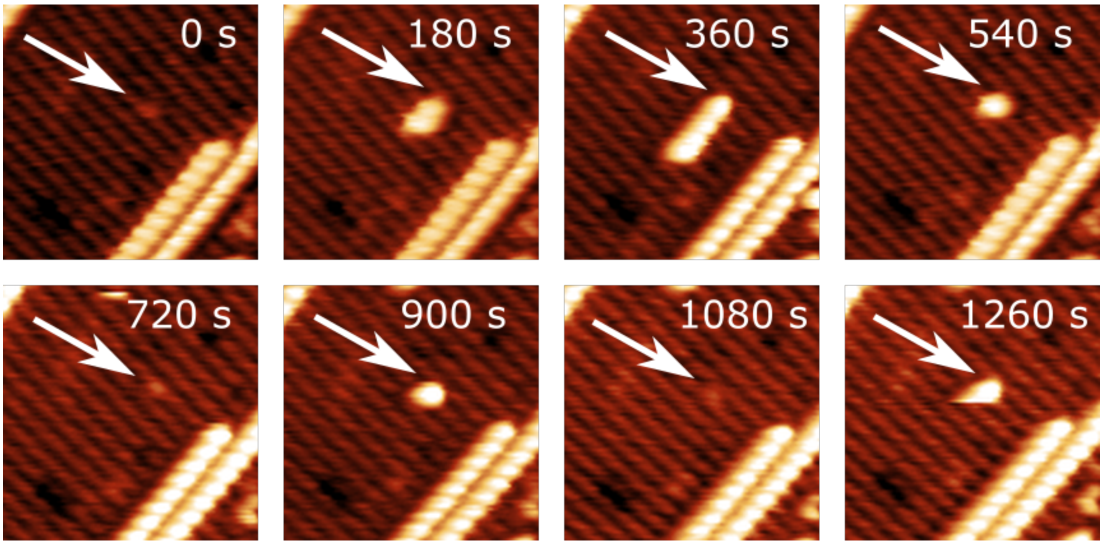

**Figure 6.6:** A sequence of STM images taken at 350 K showing repeated attachment and detachment of a Sn adatom to a $C$-type defect (scanning conditions: $U_s = -2$ V, $I = 0.3$ nA). The $C$-type defect is marked by a white arrow.

Activation energy for detachment of an adatom from a $C$-type defect can be considered a good comparable measure of its strength as a nucleation center. We employed an approach similar to the one used for the derivation of activation energies for detachment from the chains' terminations. The tunneling conditions ($U_s = -2$ V and $I = 0.3$ nA) were used, for which the tip influence on the processes of detachment and attachment was found to be negligible in comparison with the thermal activation. From the line scanning measurements over the $C$-type defects, we extracted the time intervals between the adsorption of a migrating adatom on the defect and either its consequent detachment or attachment of another adatom. Using the equation (6.9) the time constants for detachment and attachment were derived for six different temperatures. Figure 6.5(c) shows the temperature dependency of the time constant $\tau_{\mathrm{det}}$. Activation energy for detachment of an Sn adatom from the $C$-type defect and corresponding frequency prefactor (corrected for "zero event" effect) obtained from this dependency are:

$$E_a^C = (0.86 \pm 0.08) \text{ eV} \qquad \nu_0^C = 3 \times 10^{12\pm1} \text{ s}^{-1} \tag{6.12}$$

The values of activation energy and frequency prefactor are in the margin of uncertainty identical with the ones obtained for detachment of adatoms from odd terminations. Similar local character of the potential-energy surface in the close vicinity of $C$-type defects and odd terminations is the probable cause for this similitude.

### 6.1.2 Growth characteristics of Sn structures

Obtaining the activation energies for detachment of individual adatoms from grown Sn structures on Si(100)-$(2 \times 1)$ and $C$-type defects in the previous section was a leap forward in the description and understanding of the growth process in its early stages. If the energy barriers for hopping of individual Sn adatoms in the directions parallel to and perpendicular with the Si dimer rows were also known, we would have a complete picture of the growing process of Sn on Si(100)-$(2 \times 1)$ and would be able to simulate/predict not only the mechanics of the growth but also the qualitative and quantitative character of the grown structures. As was mentioned in Section 3.3, the reverse order of the investigation is also possible. We can experimentally acquire the qualitative and quantitative growth characteristics and then endeavour to find such growth controlling parameters for which the simulation of the growth yield the same results as the experiment. The parameters that are obtained this way are usually the activation energies for hops of individual adatoms in various directions on the surface.

| | **Al** | | **Ga** | | **In** | |
|---|---|---|---|---|---|---|
| | $E_a^{\parallel}$ | $E_a^{\perp}$ | $E_a^{\parallel}$ | $E_a^{\perp}$ | $E_a^{\parallel}$ | $E_a^{\perp}$ |
| DFT [52] | 0.305 | 0.466 | 0.283 | 0.332 | 0.269 | 0.272 |
| DFT [45] | 0.300 | 0.100 | | | | |
| KMC [32] | | | 0.700 | 0.350 | | |
| KMC [39] | | | | | 0.640 | 0.640 |
| STM [113] | | | | | 0.260 | 0.280 |

**Table 6.2:** Activation energies of different Group III adatom hopping on the Si(100) surface in directions parallel and perpendicular to Si dimer rows estimated by various techniques. All values are in eV.

Several papers focused on the estimation of activation energies for hops of individual Group III adatoms on the Si(100) surface. The techniques that were used include pure theoretical DFT calculations, KMC simulations, statistical analysis of the distribution of hopped distances and direct observation of individual hops at LT. A summary of the activation energies for various Group III adatom hopping in different directions on Si(100) estimated to this day are summarized in Table 6.2. The listed DFT calculations did not provide the values of frequency prefactors for individual hops. All the KMC simulations assumed, on the other hand, that the value of the prefactor is $\nu_0 = 10^{13}$ s$^{-1}$. Only the STM results for

In provided experimentally measured frequency prefactor $\nu_0 = 4 \times 10^{11\pm2}$ s$^{-1}$, which is in agreement with the generally accepted value $\nu_0 = 10^{13}$ s$^{-1}$ within the margin of error.

A serious discrepancy between the values obtained from KMC simulations and the DFT calculations can be seen from the Table 6.2. The values obtained from the KMC simulations are usually more than twice the values obtained by the DFT calculations or by the direct observations of adatom hopping by STM at LT. Even though there is also a difference between the values obtained by DFT calculations and from the LT STM measurements, the disagreement is not very significant and does not seem to be as systematic as in case of KMC simulations. The most probable and straightforward explanation of the difference between KMC results and the DFT calculations (or LT STM experiments) is the difference of the dynamic of the potential energy surface. The DFT calculations and LT STM experiments work with Si(100)-c($4 \times 2$) surface with frozen buckling, whereas the KMC simulations build upon the growth characteristics obtained at RT, at which the Si surface dimers flip-flop rapidly. Even though this makes the comparison of the KMC simulation results with the theoretically predicted values of activation energies for individual hops complicated (if not impossible), estimation of the activation energies for individual hops at RT cannot be utterly omitted from the field of investigation as it is a crucial piece of information for technological applications that are prepared and mostly work at this temperature.

Focusing on the statistical characteristics of the Sn chains, we have executed a number of experiments to obtain the characteristics for various coverages and different evaporation speeds (see Table 6.3). It was shown in Subsection 6.1.1 that in high-resolution STM images it is possible to distinguish odd and even terminations of Sn chains and thus determine with atomic precision the lengths of individual chains. However, acquiring such a resolution requires high quality STM tip and also a large amount of experimental time, which is not optimal if large statistical sets of images are to be collected. To overcome the inability to identify odd and even terminations in the vast majority of the processed images, we have assumed that all the chains are formed only of dimers and thus having only even length. Because the high-resolution images showed that the chains have equally likely odd or even termination, the impact of our assumption on the uncertainty of the acquired statistical characteristics should average out [118].

In Subsection 6.1.1 it was shown that the $C$-type defects act as preferred adsorption sites for migrating Sn adatoms and thus it can be expected that their concentration plays an important role during the growth of Sn chains. Concerning the concentration of $C$-type defects, it was reported that if the evaporation source is very near to the sample, the concentration can increase during the deposition of the material via desorption of residual water molecules from parts that are heated by the evaporation source [39]. It was, however, not the case of our experiments where the evaporation source was several tens of centimeters away from the sample. Thus, we have considered the initial concentration of $C$-type defects at the beginning of the experiments as constant.

The usual size of the investigated areas on the Si(100)-($2 \times 1$) surface was (50 nm × 50 nm). This size was found to be optimal, because it provided large enough field of view to register terraces with $\approx 150 \times 150$ adsorption sites and at the same time allowed us to distinguish individual dimers in the chains. To

| $\Theta$ (ML) | Deposition rate (ML/s) | $\langle s_{\mathrm{all}} \rangle$ | $\langle s_C \rangle$ | Chains on $C$-type defects | Occupied $C$-type defects | $\Theta_C$ (ML) | $N$ |
|---|---|---|---|---|---|---|---|
| 0.035 | 0.00230 | 13.1 | 13.3 | 65% | 33% | 0.0015 | 763 |
| 0.063 | 0.00180 | 12.9 | 12.8 | 62% | 54% | 0.0050 | 905 |
| 0.035 | 0.00023 | 17.3 | 16.9 | 35% | 46% | 0.0030 | 995 |

**Table 6.3:** Statistical characteristics of Sn chains for different deposition rates, coverages of Sn adatoms and $C$-type defects. $\langle s_{\mathrm{all}} \rangle$ is the average chain length computed from the whole population of chains, $\langle s_C \rangle$ is the average chain length calculated from the chains terminated on $C$-type defects and $N$ is total number of the investigated chains. Ratio of the chains anchored at $C$-type defects is normalized with respect to total number of chains. The experiments are referenced in the text in the same order as they are listed in this table.

exclude the influence of the surface step edges on the growth, we have chosen only the terraces that were much wider than an average length of chain.

Figures 6.7(a)-(c) show histograms of chain length distributions for all three experiments together with the scaled chain length distributions in Figure 6.7(d). Even though the length of the chains may evolve during the time of the experiment, the average time for detachment of Sn adatom from the even termination at RT is $\approx$ 13 600 s (see Subsection 6.1.1 and the respective activation energies for detachment). Thus, we can consider the chains as having constant length. The distributions contain data of approximately 1000 chains for each experiment. The data were obtained from approximately 20 STM images, which were taken from different surface areas two hours after the deposition. The histograms include both free chains and the chains nucleated on $C$-type defects, since the heterogeneous nucleation can be the governing factor for the growth kinetics and consequently define the shape of the distribution.

Inspecting the scaled chain length distribution closely, we can see that it does not exhibit a shape typical for the two ideal cases. 1) It does not have a monomodal shape with well defined maximum at 1, which is characteristic for irreversible growths with isotropic migration of adatoms and negligible role of surface defects. 2) It also does not have a shape of exponential decay, which is characteristic for reversible growths in TE or for irreversible growths with either strong anisotropic migration of adatoms or with non-negligible role of surface defects (see the list of reasons for monotonically decreasing shape of function $g$ in Section 3.3). Thus, a complex combination of reversibility/irreversibility of the growth, isotropy/anisotropy of the adatom migration and interaction with the surface defects can be expected.

We have already mentioned that the average time for detachment of Sn adatom from a dimer termination at RT is $\approx$ 13 600 s. This makes the growth of Sn chains at RT practically irreversible. Since the concentration of the $C$-type defects in our experiments was not very low, their presence had to be taken into account. The unknown isotropy/anisotropy of the adatom migration and its influence on the character of the growth had to be also inspected.

Having gathered the growth characteristics presented in Table 6.3 together with the scaled chain length distribution shown in Figure 6.7(d), we had enough

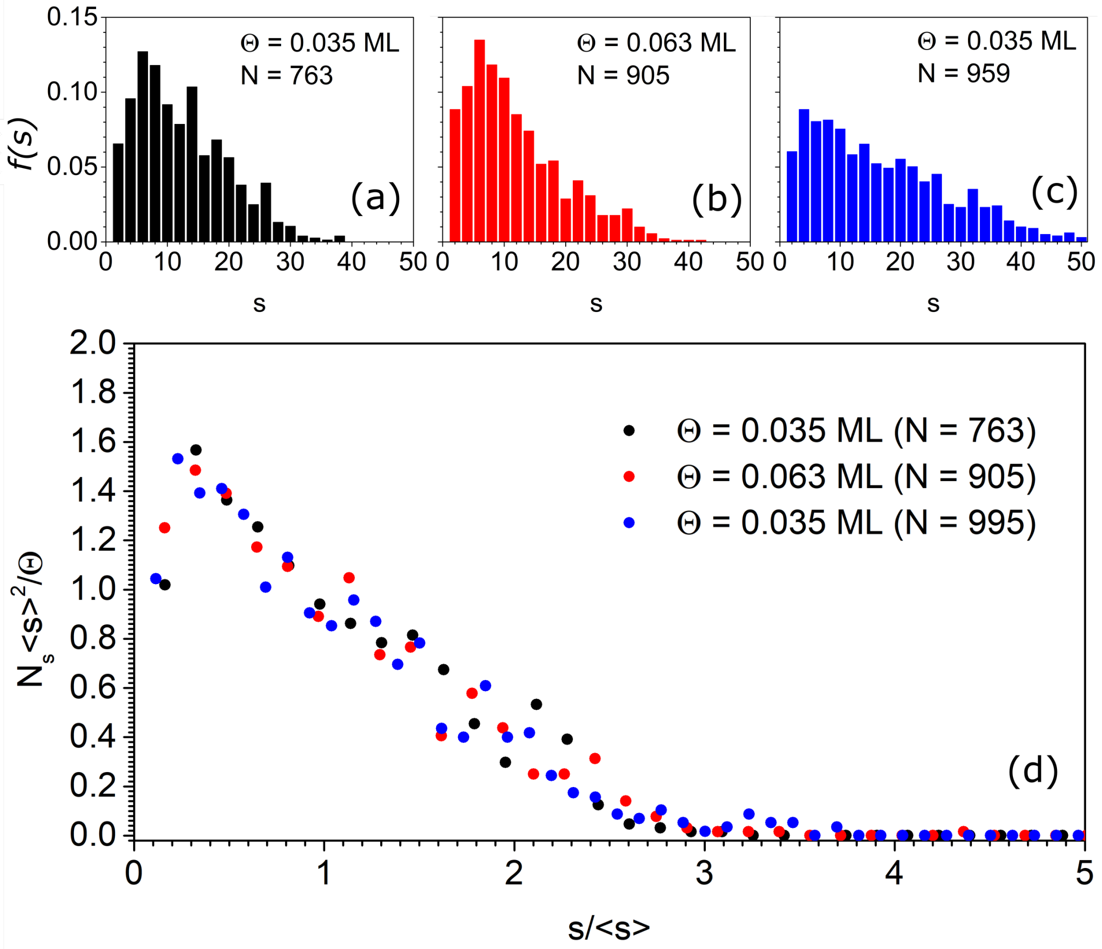

**Figure 6.7:** (a)-(c) Chain length distributions for 3 different experimental conditions (deposition rate, deposition time, concentration of defects etc.). $f(s)$ is the value of the relative frequency of the length $s$ in the whole population of the chains. The order of the histograms correspond with the order of the experiments in the Table 6.3. (d) The scaled chain length distributions for all 3 experiments. The colors of the distributions correspond with the colors used in histograms (a)-(c).

experimental information that could have been compared with the results of the KMC simulations of our model described in Chapter 5. From the free parameters of the model (see Table 5.2), we were able to assign a fixed/known value to all but 2 parameters. Several parameters were defined by the setup of the experiments - deposition rate, time of deposition, temperature, etc.. In the previous section we have directly obtained the activation energies for detachment of Sn adatom from dimer termination $E_a^E$, monomer termination $E_a^O$ and from $C$-type defect $E_a^C$. To obtain the binding energies of the adatoms to different types of terminations and $C$-type defect, the lower of the two hopping energy barriers (parallel $E_a^{\parallel}$ and perpendicular $E_a^{\perp}$) has to be subtracted from the activation energies for detachment.

Using the measured energies $E_a^E$, $E_a^O$ and $E_a^C$ and 2 unknown tunable parameters $E_a^{\parallel}$ and $E_a^{\perp}$, we were able to assign the value to all the remaining parameters

- binding energies ($E_{\mathrm{DD}}$, $E_{\mathrm{MD}}$, $E_{\mathrm{MM}}$ and $E_{\mathrm{C}}$) - in the following way:

$$\begin{aligned}E_{\mathrm{MM}} &= 0\\ E_{\mathrm{DD}} &= E_a^E - \min(E_a^{\|}, E_a^{\perp}) = 1.02 - \min(E_a^{\|}, E_a^{\perp})\\ E_{\mathrm{MD}} &= E_a^O - \min(E_a^{\|}, E_a^{\perp}) = 0.88 - \min(E_a^{\|}, E_a^{\perp})\\ E_{\mathrm{C}} &= E_a^C - \min(E_a^{\|}, E_a^{\perp}) = 0.86 - \min(E_a^{\|}, E_a^{\perp})\end{aligned} \tag{6.13}$$

The choice of the value 0 for the parameter $E_{\mathrm{MM}}$ was based on the fact that we have never observed two Sn monomers to be bound to each other over a Si dimer row.

Because the value of the frequency prefactor generally used in KMC simulations - $\nu_0 = 1 \times 10^{13}\ \mathrm{s}^{-1}$ - matches all our previously measured prefactors ($\nu_0^E = 3 \times 10^{14\pm1}\ \mathrm{s}^{-1}$, $\nu_0^O = 3 \times 10^{13\pm1}\ \mathrm{s}^{-1}$ and $\nu_0^C = 3 \times 10^{12\pm1}\ \mathrm{s}^{-1}$) within the margin of uncertainty, it was used in all our simulations.

We run the simulations of the growth of the Sn on Si(100)-(2 × 1) individually for the three presented experiments. A set of growth characteristic (average chain length, ratio of chains nucleated on $C$-type defects and chain length distribution) was obtained from the simulated layers by averaging the results of 50 simulation runs for each combination of $E_a^{\|} \in [0.35, 0.70]$, $E_a^{\perp} \in [0.40, 0.70]$. We have then studied the deviations of the simulated growth characteristics from the experimentally observed ones. The deviations $D$ of the simulations from the experiments were calculated as follows:

1. For the average chain length $\langle s \rangle$:

$$D_{\langle s \rangle} = (\langle s \rangle_{\mathrm{simulation}} - \langle s \rangle_{\mathrm{experiment}})^2 \tag{6.14}$$

2. For the ratio of chains nucleated on $C$-type defects $r^C$:

$$D_{r^C} = (r^C_{\mathrm{simulation}} - r^C_{\mathrm{experiment}})^2 \tag{6.15}$$

3. For the chain length distribution:

$$D_f = \sum_{s=1}^{s=\infty} (f(s)_{\mathrm{simulation}} - f(s)_{\mathrm{experiment}})^2, \tag{6.16}$$

   where $f(s)$ is the relative frequency of the length $s$ in the chain length histogram. We did not compare the scaled chain length distributions $g$, but rather the distributions represented by relative frequencies $f$. The analytical expression for the experimentally measured function $g$ was not easily obtainable, since its shape was more complicated than simple exponential decay measured for example for In [39].

Because the chain length distribution $f(s)$ contains among others also the information about the average chain length $\langle s \rangle$, using $\langle s \rangle$ as the comparative growth characteristic was unnecessary. We wanted, however, to examine the simulation results in their complexity and thus we decided to also include $\langle s \rangle$ among the comparative characteristics.

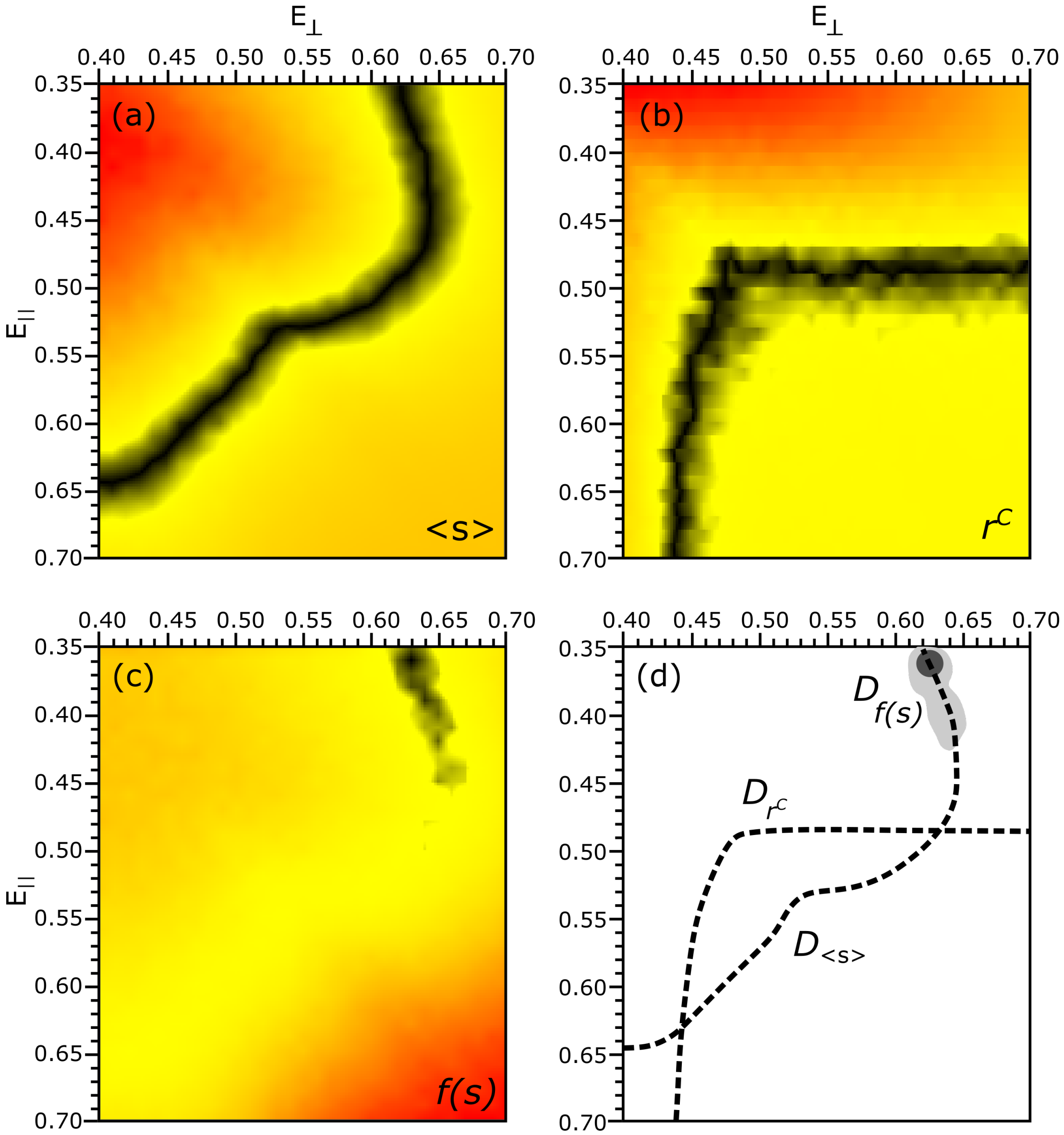

**Figure 6.8:** (a)-(c) An example of diagrams of deviations $D$ of simulations from experiment for different growth characteristics. (d) A simplified schema, where the "paths" of minimum $D$ for individual growth characteristics are put together.

Figure 6.8 shows an example of the diagrams that contain dependencies of the deviations $D$ on the combinations of $E_a^{\|}$, $E_a^{\perp}$. The color scale represents the quality of the match with black being the best match and red the worst one.

The best agreement between the simulation and the experiment for the average chain length $\langle s \rangle$ is represented by a continuous path of combinations of $E_a^{\|}$, $E_{\perp}$, for which the quality of the agreement is the same [see Figure 6.8(a)]. This is also true for the comparison of the percentage of chains nucleated on the $C$-type defects [see Figure 6.8(b)]. On the other hand, the best agreement between the simulation and experiment for the chain length distribution is represented by one global minimum in the diagram [see Figure 6.8(c)]. This global minimum lies naturally on the path of best agreement for the average length.

We expected to find a unique combination of $E_a^{\|}$, $E_a^{\perp}$ for which there would be an excellent agreement between simulations and experiments for all the studied growth characteristics. In ideal case it would mean that the global minimum $D_f$ would lie at the intersection of the minimum paths $D_{\langle s\rangle}$ and $D_{r^C}$ for all experiments. In practice the unique combination of $E_a^{\|}$, $E_a^{\perp}$ is sometimes the point that is the least distant from minimum paths $D_{\langle s\rangle}$ and $D_{r^C}$ and from the global minimum $D_f$ [39].

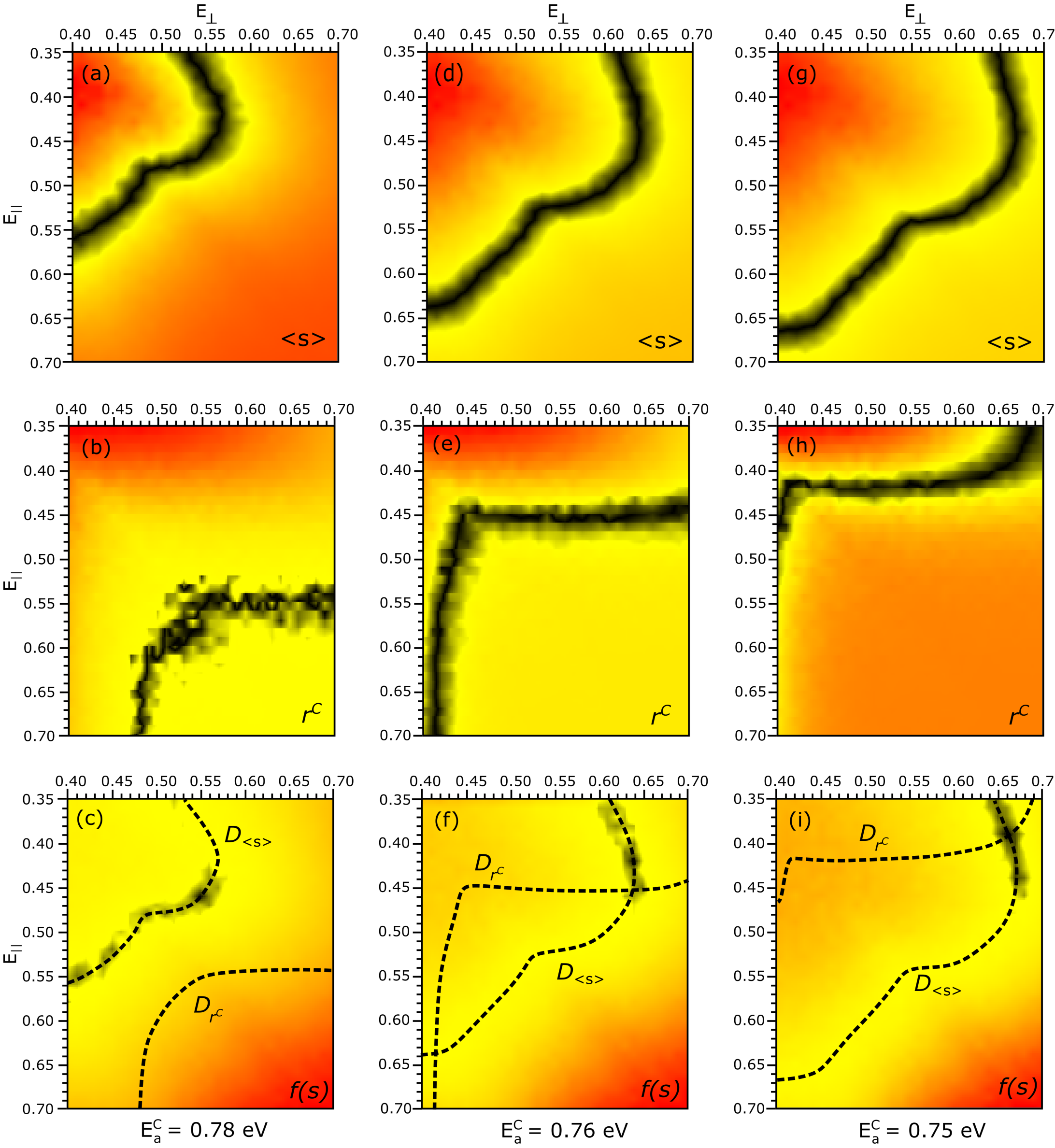

**Figure 6.9:** An example of 3 possible outcomes of the simulations represented by diagrams of deviations $D$. The choice of the model parameters correspond to the first experiment from the Table 6.3. The different values of $E_a^C$ are showed below the diagrams.

In our case the minimum paths $D_{\langle s\rangle}$ and $D_{r^C}$ did intersect, but the global minimum $D_f$ was too "far away" from the intersection that the disagreement could not be explained within the uncertainty of the measurements. Investigating the results of the simulations in detail, we have found out that our experimentally obtained mean value of $E_a^C$ used for the simulations is too high. The percentage of the chains nucleated on the $C$-type defects was 100% for most of the combinations $E_a^{\|}$, $E_a^{\perp}$. This was in direct contrast with the experimental percentages (35%-65%)

presented in the Table 6.3. This led us to a decision to use the parameter $E_C$ as a third free parameter.

Running several testing simulations we found the sensitivity of the model to the changes of the parameter $E_C$ and determined that the "correct" value of $E_a^C$ should be looked for in the interval of energies from 0.7 eV to 0.8 eV. Using the value of $E_a^C$ above 0.8 eV resulted in all the chains being anchored to $C$-type defects. Using the value of $E_a^C$ bellow 0.7 eV resulted in Sn chains not nucleating on $C$-type defects at all.

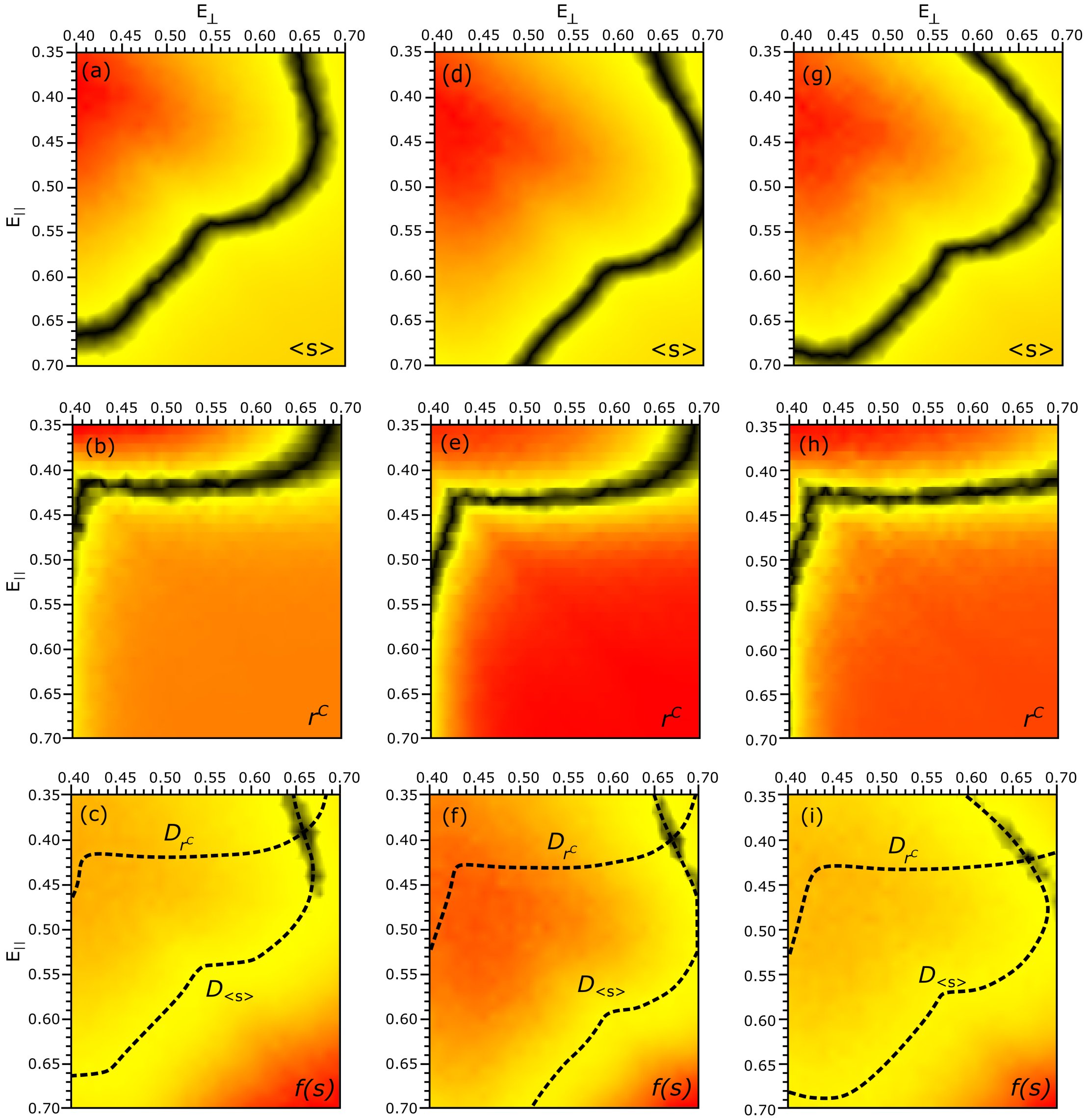

$E^C = 0.75$ eV

$E^C = 0.75$ eV

$E^C = 0.76$ eV

**Figure 6.10:** Diagrams of deviations $D$ corresponding to the best agreement between the simulated growth characteristics and the measured ones. Figures (a)-(c), (d)-(f) and (g)-(i) correspond to the first, second and third experiment listed in the Table 6.3 respectively.

With the 3 tunable parameters, there existed 3 possible outcomes of the simulations based on the value of $E_C$ (see Figure 6.9)

1. The minimum paths $D_{\langle s\rangle}$ and $D_{r^C}$ did not intersect [see Figure 6.9(a)-(c)]

2. The minimum paths $D_{\langle s \rangle}$ and $D_{r^C}$ intersected (1 or 2 intersections) but the intersection(s) did not correspond with the global minimum $D_f$ [see Figure 6.9(d)-(f)]

3. The minimum paths $D_{\langle s \rangle}$ and $D_{r^C}$ intersected (1 or 2 intersections) and one of the intersections corresponded with the global minimum $D_f$ [see Figure 6.9(g)-(i)]

Only the third type of the simulation outcome was the one for which there existed the best match between the experiment and the the simulation for all simulated growth characteristic for a given unique combination of $E_a^{||}$, $E_a^{\perp}$ and $E_a^{\mathrm{C}}$. It was this simulation outcome that we were trying to achieve. This situation is depicted in the Figure 6.10. The unique combination of the fitting parameters $E_a^{||}$, $E_a^{\perp}$ and $E_a^{\mathrm{C}}$ was the same, within the margin of uncertainty, for all 3 experiments. The obtained values are:

$$\begin{aligned} E_a^{||} &= 0.40 \pm 0.05 \text{ eV} \\ E_a^{\perp} &= 0.66 \pm 0.05 \text{ eV} \\ E_a^{C} &= 0.75 \pm 0.05 \text{ eV} \end{aligned} \tag{6.17}$$

Figure 6.11(a)-(c) shows the comparison of the simulated histograms of chain lengths with the experimentally measured ones. Figure 6.11(d) also shows the comparison of the resulting scaled distributions. In Figure 6.12 there is further presented the comparison of the measured STM images with the simulated grown structures of Sn on Si(100)-(2 × 1) at RT.

The results presented in equation (6.17) show that the hopping of Sn adatoms on Si(100)-(2 × 1) surface is anisotropic with the fast direction being the one parallel with the Si dimer rows. Even though the newly obtained mean value of activation energy for detachment from $C$-type defect ($E_a^C = 0.75 \pm 0.05$ eV) is different from the one obtained from the measurements of the evolution of the chain lengths [see equation (6.12)], both values can be considered as corresponding to each other within the margin of uncertainty.

To finally estimate the impact of the two factors - adatom hopping anisotropy and non-negligible concentration of $C$-type defects - on the character of the growth and therefore on the shape of the scaled chain length distribution for our system Sn/Si(100)-(2 × 1), we have run several simulations for different hopping anisotropies and different concentrations of $C$-type defects.

Figure 6.13 shows the results of these simulations. We have simulated 2 types of anisotropic hopping (one with faster direction being the parallel with Si dimer rows and one with opposite anisotropy) and 1 isotropic hopping. For each of these 3 types of hopping isotropy/anisotropy, we have run simulations for 6 different $C$-type defect coverages. Identical shapes of the scaled chain length distributions are plotted in the same colour in each graph.

We can conclude from the depicted distributions that for the isotropic hopping the shape of the distribution is a monomodal with well defined maximum at 1 and it is not influenced at all by any coverage of $C$-type defects from the investigated interval. For the anisotropic hopping with the faster direction being the one perpendicular to the Si dimer rows, the shape of the distribution for low coverages of $C$-type defects is nearly identical to the shape obtained for

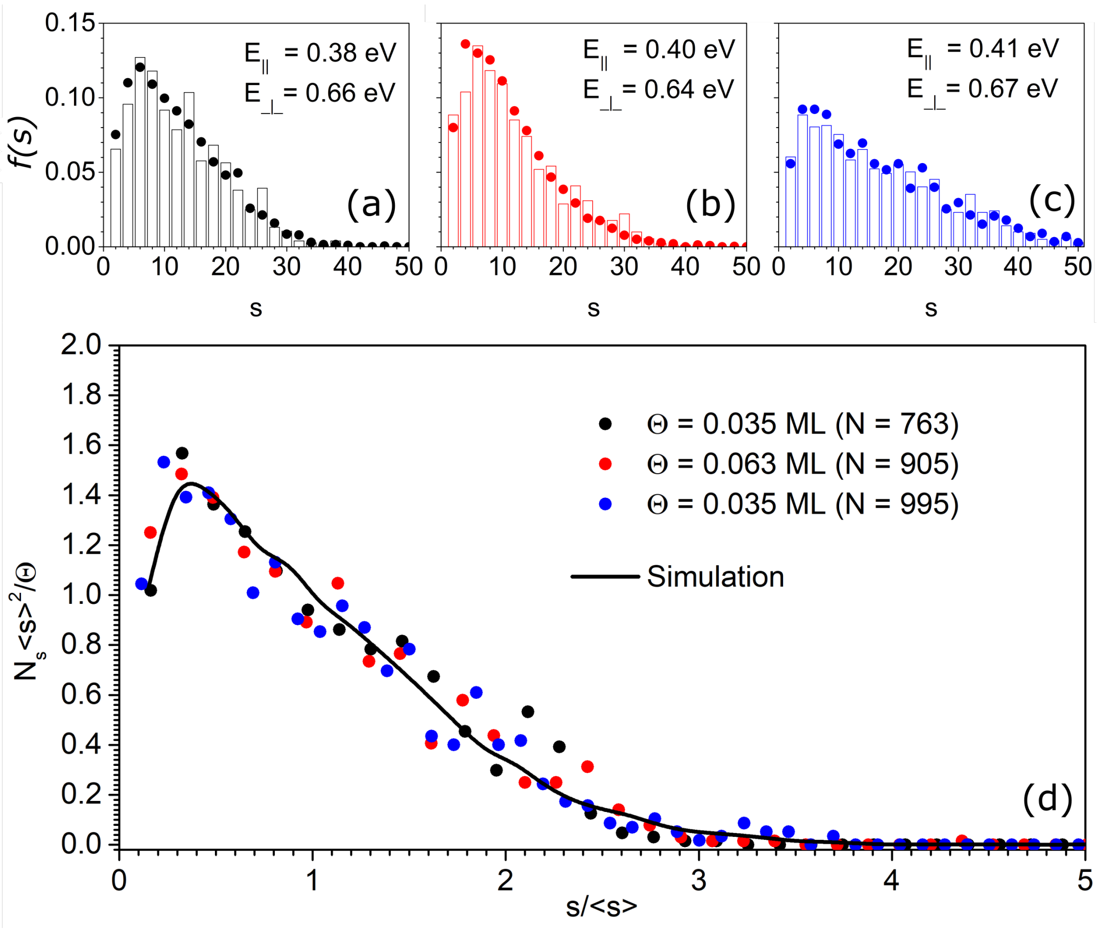

**Figure 6.11:** (a)-(c) Comparison of the simulated histograms of chain lengths with the experimentally measured ones. Each histogram contains the values of $E_{||}$ and $E_{\perp}$ for which the best fit was found. (d) The scaled chain length distribution of all experiments compared with the simulated one.

isotropic hopping. Thus, this kind of anisotropy does not change the shape of the scaled chain length distribution. However, unlike for the isotropic hopping, the shape of the distribution slightly changes for high coverages of $C$-type defects. Nevertheless, the change is not very pronounced and the monomodal character of the distribution's shape remains unchanged.

Based on the results published in [32], we expected a visible change of the shape of the scaled chain length distribution for anisotropic hopping with the faster direction being the one parallel with Si dimer rows with 0 coverage of $C$-type defects. Comparing the shapes of the distributions plotted by black symbols for different anisotropies in Figure 6.13, we can see that our observations are in agreement with these expectations. We can also see that for this type of hopping anisotropy, the presence of the $C$-type defects plays a crucial role during the growth of Sn on Si(100)-(2 × 1). Even the coverage of $C$-type defects as low as 0.0015 ML (which is also the lowest $C$-type defects coverage in our experiments) causes further change of the shape of the scaled chain length distribution.

We can recall now our discussion about the causes of the shape of the scaled chain length distributions shown in Figure 6.7 and make final conclusion. Both anisotropic hopping of Sn adatoms and the presence of non-negligible concen-

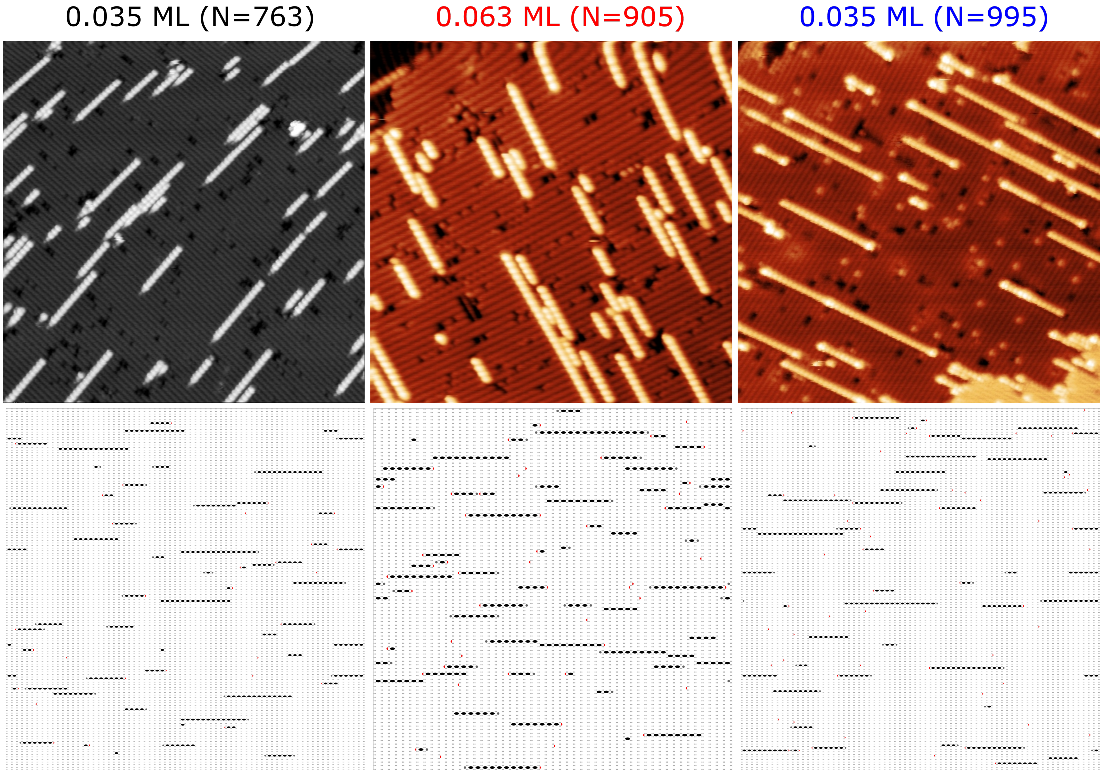

**Figure 6.12:** Comparison of the measured STM images of all three experiments with the simulated grown structures.

tration of $C$-type defects on the surface influence significantly the kinetic of the growth of the Sn chains.

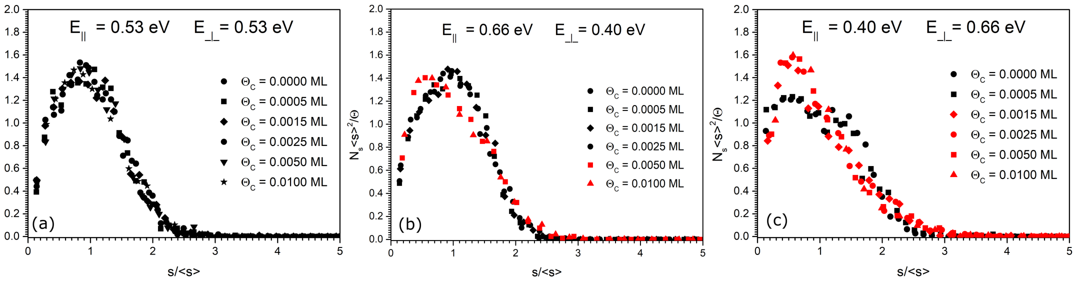

**Figure 6.13:** Comparison of the simulated scaled chain length distributions for different choices of hopping barriers and for various coverages of $C$-type defects. Simulations giving the same shape of the distribution are plotted by the same color in individual graphs. The choice of parameters (other than the $C$-type defects coverage and hopping barriers) are the same as for the experiment listed as the first one in Table 6.3.

Unfortunately, there exist no theoretical calculations or direct experimental measurement of the values $E_a^{\|}$, $E_a^{\perp}$ and $E_a^{\mathrm{C}}$, with which we could compare our results [see equation (6.17)]. We can at least discuss some similarities and differences with the values calculated/measured for various Group III metals by different techniques shown in Table 6.2. Both our values $E_a^{\|}$ and $E_a^{\perp}$ are within the range of usually presented values of hopping barriers. Our value of $E_a^{\perp}$ is twice any value of $E_a^{\perp}$ computed by DFT or directly measured at LT for all Group III metals, but it is almost the same as the value $E_a^{\perp}$ obtained by KMC simulations for In. Thus, we expect that the same discrepancy that exists between KMC and DFT (or LT experiments) results for In will exist also for our KMC results for Sn.

### 6.1.3 Summary

In the previous two sections, we have presented a detailed study of the growth and decay of Sn chains on Si(100)-($2 \times 1$) at RT and higher temperatures. Direct STM observations showed several interesting features of the system:

1. At RT Sn chains nucleate on $C$-type defects
2. At RT and higher temperatures it is possible to observe two different types of Sn chain termination - Sn monomer (odd termination) or dimer (even termination)
3. The buckling of Sn chains is caused not only by presence of another chain in its close vicinity, but it is also induced by the existence of the odd termination of the chain

Line scanning method was used to study the fluctuation of the chain length. Because of the concurrent presence of both detachment and attachment processes, we developed a statistical model, which allowed for calculation of the time constants for detachment from the observed average times between individual processes. The time constants obtained for various temperatures were used to estimate the activation energies for detachment of Sn adatoms from $C$-type defects ($E_a^C$), monomer termination ($E_a^O$) and dimer termination ($E_a^E$) together with the respective frequency prefactors.

The growth characteristics of Sn structures for different coverages and experimental conditions were gathered. The KMC model introduced in Chapter 5 was used to simulate the evolution of the system Sn/Si(100)-($2 \times 1$) during the deposition and consecutive relaxation. The previously found values of activation energies for detachment of Sn adatoms ($E_a^C$, $E_a^O$, $E_a^E$) were used in the model to fix its unknown parameters. By tuning 2 free parameters - $E_a^{\parallel}$ and $E_a^{\perp}$ - we were looking for the best match between the simulated growth characteristics and the measured ones for all experiments. The previously measured value of $E_a^C$ used in the model was found to be too high, because all the chains in the simulations were nucleated at the $C$-type defects, which was in direct contrast with the experiment. Parameter $E_a^C$ was then used as a third free parameter of the model. With 3 tunable parameters, we managed to achieve the agreement between the simulated growth characteristics and the measured ones for all experiments. It was eventually shown that the character of the growth of Sn on Si(100) is influenced by the strong anisotropy of the adatom migration and by the concentration of the $C$-type defects on the surface.

The complete set of the activation energies together with the corresponding frequency prefactors, which were either directly measured or obtained from the comparison of our model with the experimental results, are listed below. Please note that for the values obtained from the KMC simulations, the prefactors are the same for all the activation energies ($\nu_0 = 1 \times 10^{13}$ s$^{-1}$). Also notice that the energy $E_a^C$ is listed twice for the comparison of the experimental and KMC result.

$$\begin{aligned}
\text{EXP: } E_a^O &= (0.88 \pm 0.08) \text{ eV}, \quad \nu_0^O = 3 \times 10^{13\pm1} \text{ s}^{-1} \\
\text{EXP: } E_a^E &= (1.02 \pm 0.08) \text{ eV}, \quad \nu_0^E = 3 \times 10^{14\pm1} \text{ s}^{-1} \\
\text{EXP: } E_a^C &= (0.86 \pm 0.08) \text{ eV}, \quad \nu_0^C = 3 \times 10^{12\pm1} \text{ s}^{-1} \\
\text{KMC: } E_a^C &= (0.75 \pm 0.05) \text{ eV}, \quad \nu_0^C = 1 \times 10^{13} \text{ s}^{-1} \\
\text{KMC: } E_a^{\parallel} &= (0.40 \pm 0.05) \text{ eV}, \quad \nu_0^{\parallel} = 1 \times 10^{13} \text{ s}^{-1} \\
\text{KMC: } E_a^{\perp} &= (0.66 \pm 0.05) \text{ eV}, \quad \nu_0^{\perp} = 1 \times 10^{13} \text{ s}^{-1}
\end{aligned} \tag{6.18}$$

## 6.2 Aluminium on Si(100)

### 6.2.1 Basic Al objects on Si(100)-$(2 \times 1)$

During the initial studies of Al chains grown on the Si(100)-$(2 \times 1)$ surface, there were two theoretical papers published by Brocks et al. [45, 55]. The binding energy of Al monomer at the end of the chain calculated in the papers was 0.4 eV and it was concluded that the monomer terminations are not very stable and that most of the Al chains would contain only dimers. The first observation of alleged monomer terminations was reported by Itoh et al. [119]. Instead of monomers, however, they have in fact observed $\pi$ states on the surface Si dimers, which was proved by the publication of calculated LDOS of Al dimer [55]. Even though the observation of Al monomer termination was then published in several articles [48, 58, 120], the mere statement that the observed objects are genuine Al monomers lacked further proofs or explanations.

To shed some light on this issue, we used the STM to thoroughly investigate the basic Al objects (adatoms, dimers) on the Si(100)-$(2 \times 1)$ at various voltages ($\pm 0.4$ eV - $\pm 2.0$ eV) for different coverages (0.01 ML - 0.07 ML). We then compared our findings with theoretically predicted behavior of Al on Si(100)-$(2 \times 1)$ to further support our findings.

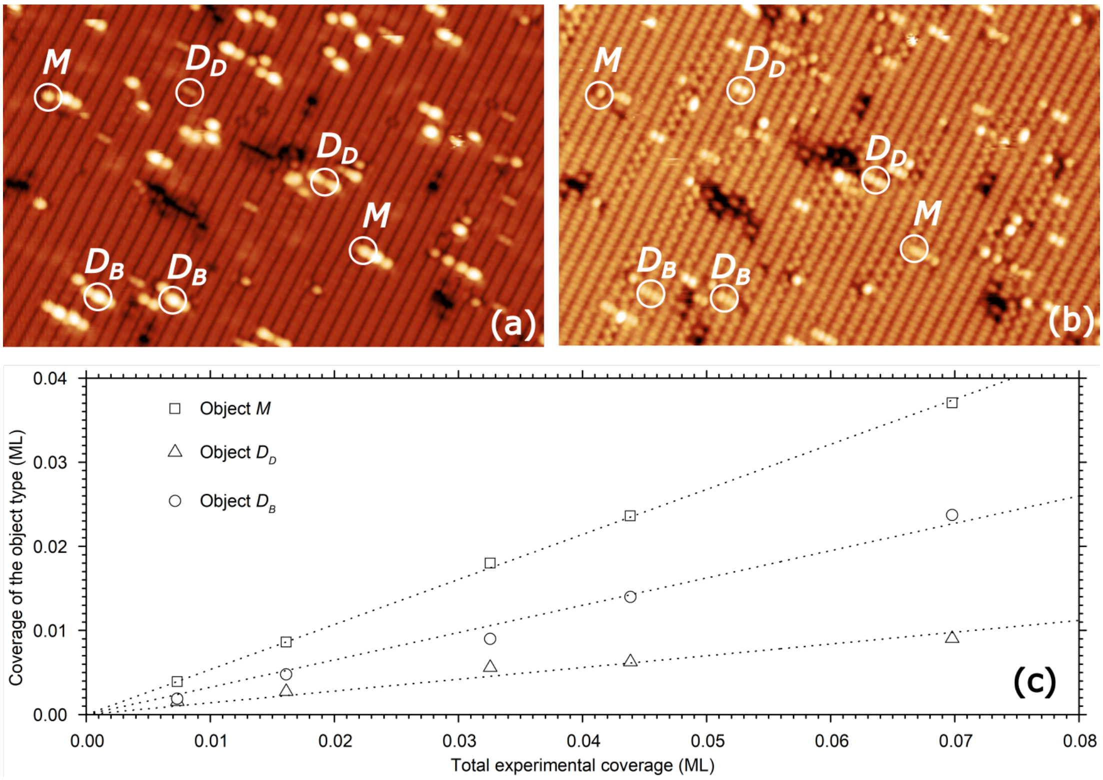

**Figure 6.14:** STM images in (a) empty and (b) filled states of area 30 nm × 19 nm with aluminium objects on Si(100) . The sample voltage was $U_S = \pm 2$ V and the tunneling current was $I = 0.3$ nA. White circles mark examples of the 3 basic types of Al objects that can be found as parts of larger structures. (c) A dependency of percentage of individual objects on the total experimental coverage.

In Figure 6.14(a)-(b) there are STM images in empty and filled states showing the same area of the Si(100)$2 \times 1$ surface with 0.01 ML Al deposited on it at RT.

The majority of the objects visible on the surface are short chains consisting of Al adatoms. Compared to the structures formed by other Group III metals at very low coverages, the Al chains are shorter and appear to be formed from non-identical objects of various contrast. During the course of our investigation, we identified 3 basic types of these objects, from which the Al chains are formed. These objects can be unambiguously distinguished based on their characteristic imaging in STM. We have denoted them as $M$, $D_D$, $D_B$ and they are all marked in the Figure 6.14(a)-(b).

In order to verify that these objects consist exclusively of Al adatoms, we have investigated the dependency of the their surface concentration on the total Al coverage. Figure 6.14(c) shows the measured results and from the strong linear dependencies we can conclude that all 3 objects - $M$, $D_D$, $D_B$ - consist of Al adatoms. Our observations imply that the $M$ object is an aluminium monomer and objects $D_D$ and $D_B$ both correspond to an Al dimer. The subscripts $D$ and $B$ for dimers are abbreviations for dark and bright respectively. All 3 objects will be further discussed in more detail in the following text.

### Object $D_D$

An STM close-up images of the $D_D$ object in empty and filled states at different sample voltages are shown in Figure 6.15(a)-(d). The $D_D$ objects are imaged at sample voltage +2 V (filled states) in STM as a bean shaped spots, slightly divided in the middle, that are positioned between Si dimers rows. At -2 V (empty states) they appear as two distinct circular spots also positioned between Si dimer rows. Lowering the sample voltage as low as 0.7 V results into significant change of imaging. In the filled states the slightly divided bean shaped spots transfer into one circular spot whereas the two distinct bright spots in empty states disappear entirely. At the same time there emerge two bright crescents both in filled and empty states on the ends of the $D_D$ objects. The crescents are positioned on the Si dimer rows between which the $D_D$ objects sit.

The observed imaging of the $D_D$ objects agrees not only with the already reported observations of individual Al dimers [119, 121] but also with the calculated LDOS [55]. The distinct bright spots at sample voltage -2 V correspond to the back bonds between Al adatoms and the Si surface. The crescents that are observed at lower sample voltages correspond to the dangling bonds on the Si surface. Because of all these agreements, the $D_D$ object was unequivocally identified as single Al dimer. It is because of its relatively dark imaging in STM that we decided to use the subscript $D$ in the name of this object.

Our experiments further showed that the presence of the $D_D$ object is not tied to the presence of another object or any type of surface defects. The majority of the observed $D_D$ objects have no surface defect in their vicinity. Nonetheless, some of the $D_D$ objects were found to be adsorbed at $C$-type defects [see Figure 6.15(e)-(f)]. It implies that the $C$-type defects play role of reaction sites for the adsorption of Al adatoms. This behaviour is not only similar to the one observed for other Group III [35, 36] and Group IV [40] metals, but is also in agreement with DFT calculations made by Pieczyrak et al. [117]. The calculations showed that the difference between adsorption energy of Al adatom on bare, defect-free Si surface and at $C$-type defect is 0.75 eV in favour of the $C$-type defect.

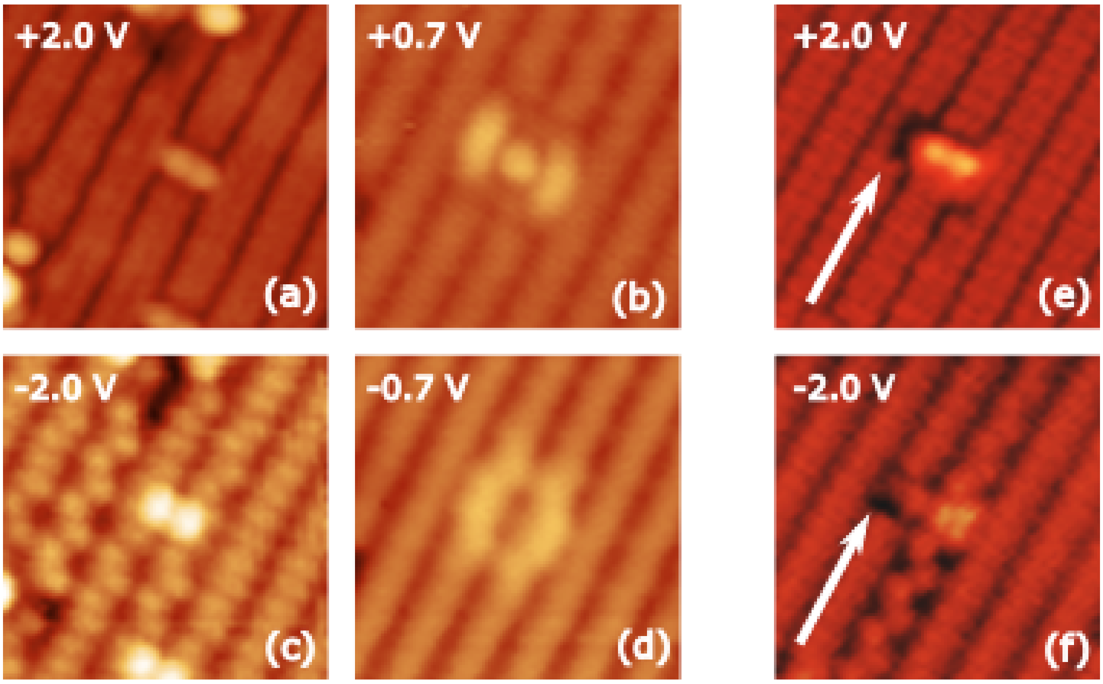

**Figure 6.15:** (a)-(d) Images (area 4 nm × 4 nm) of aluminium dimer in filled and empty states for various sample bias voltages. Images e) and f) show aluminium dimer nucleated on *C*-type defect (marked by white arrow).

Even though the presence of the $D_D$ objects is not dependent on the presence of any surface defects, it was found that the mere presence of the objects causes freezing of buckling of several Si dimers in their neighbourhood [see Figures 6.15(c) and 6.15(f)].

In none of our experiments have we ever observed 2 or more $D_D$ objects neighbouring each other in a form of a chain. Since the $D_D$ objects were positively identified as Al dimers and Al chains are known to be formed by Al dimers, the explanation of this behaviour could be that $D_D$ objects image differently in STM when they are part of larger structures. This hypothesis will be discussed later in the text.

### Object $M$

Even though it is generally accepted that the binding energy of adsorbed Al monomers to other chains' terminations on the Si(100)-(2 × 1) surface is so small that the monomer terminations are unobservable by STM at RT, we show that the $M$ objects are actually the Al monomers. They are, unlike the $D_D$ objects, not observed alone on defect-free surface as single adatoms, but their presence is always confined to the presence of another surface object: $D_D$, $D_B$, *C*-type defect (see Figure 6.16) or another $M$ object (see Figure 6.18). We have never observed the $M$ objects being adsorbed at the *A*-type or *B*-type defect.

Close-up images of $M$ objects in the filled and empty states attached to other surface objects show that at sample voltage -2 V they look like half of the $D_D$ objects - there is a bright spot, which lies between two Si dimer rows being always closer to one of them. This bright spot corresponds to the back bonds between Al monomer and the Si surface. At sample voltage +2 V the $M$ object images as circular spot that is bigger and brighter than the bean-shaped spot corresponding to $D_D$ object.

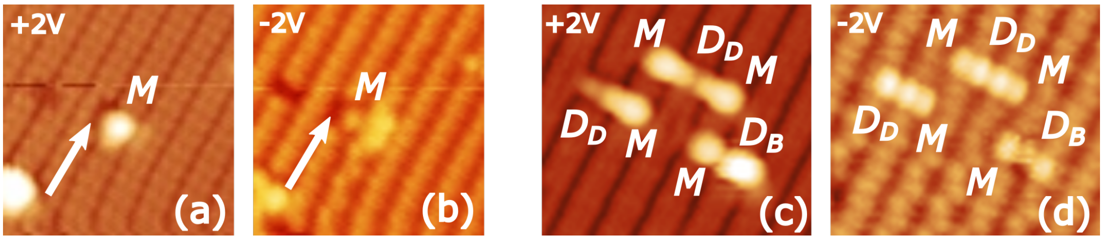

**Figure 6.16:** $M$ objects bonded to various structures. Images (a) and (b) show $M$ object bonded to C-type defect (white arrow) in empty and filled states respectively. Images (c) and (d) show empty and filled states images of $M$ objects bonded to $D_D$ objects or $D_B$ objects. All images were taken at bias voltages $U_S = \pm 2$ V.

Lowering the sample voltage to 0.4 V resulted into a significant change of imaging of the structure containing $M$ object together with $D_D$ object (see Figure 6.17). Imaging of the vicinity of the $D_D$ object was identical to the situation when an isolated $D_D$ object was observed - there appeared a bright crescent on the neighboring Si row [compare Figure 6.17(b),(d) and Figure 6.16(b),(d)]. Instead of a bright crescent a large bright cloud appeared on the Si row in the neighbourhood of the $M$ object. There is an excellent agreement between this observation and results of LDOS around the energy 0.3 eV below Fermi level calculated for an Al chain consisting of Al dimer and Al monomer [55]. These findings support our assumption that the $M$ object is an Al monomer and further supports our identification of $D_D$ object as Al dimer.

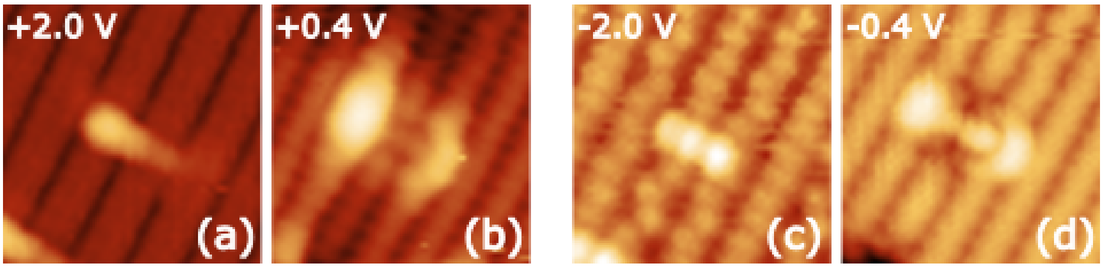

**Figure 6.17:** Imaging of aluminium chain consisting of one dimer and single aluminium adatom for various bias voltages

It was calculated by Zorn et al.[61] that apart from Al dimers the two Al monomers can form a "bridge structure" that should be stable enough (the energy of disintegration being 1.48 eV) to be observable by STM at RT. The bridge structure consists of two Al monomers bounded together over an Si dimer row [see Figure 6.18(a)-(b)]. The bridge structure was already subject of another theoretical research ten years before Zorn. Brocks et al.[55] calculated the activation energy of the transition of the bridge structure as a whole object from its original position to a new more stable one between Si dimer rows. As a result of this transition, the bridge structure would become a genuine Al dimer. The calculated activation energy of the transition is 1.1 eV, which is by 0.38 eV lower than the energy of disintegration of the structure. Thus, the bridge structure should be stable and can transform into a dimer more probably than disintegrate. Additionally to this, the activation energy of the transition is low enough to allow its observation during the course of a typical STM experiment.

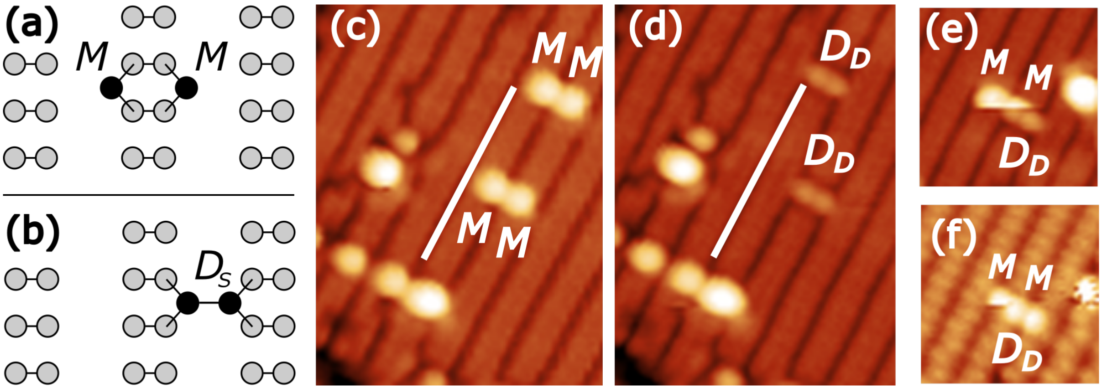

**Figure 6.18:** (a) and (b) depict schematically the bridge structure and aluminium dimer after the transition of the structure (Si atoms - gray circles, Al adatoms - black circles). Images (c) and (d) are subsequent images (taken at $U_S = +2$ V and $I = 0.3$ nA) of the same area showing transition of the "bridge" structure to the aluminium dimer. The white line helps to guide the eye. Images (e) and (f) are empty and filled states images (taken at $U_S = \pm 2$ V and $I = 0.3$ nA) respectively of the same area showing the transition of the "bridge" structure to the aluminium dimer during the scanning. The direction of the scanning is top-down.

We observed two $M$ objects (i.e. Al monomers) forming several stable bridge structures on the Si surface at RT [see Figure 6.18(c)], which is in agreement with the Zorn's predictions. We further observed transition of two $M$ objects to a $D_D$ object in the mean time between two subsequent scans [see Figure 6.18(c)-(d)], which is in agreement with the theoretical calculation of the activation energy for the transition made by Brocks. We also observed the transition during scanning of a single bridge structure [see Figure 6.18(e)-(f)]. The transition should be observable at RT as a purely thermally activated process, but we do not exclude the possibility of the transition being influenced by the STM tip. The agreement between the theoretical results and our experimental findings further supports the assumption that $M$ objects are Al monomers and $D_D$ objects are Al dimers.

### Object $D_B$

Figure 6.19(a) shows a STM image of 0.07 ML of Al on Si(100). The chains consist of several dimers and are terminated either by monomers or dimers. We denote the dimers within the longer chains as $D_B$ objects, because their imaging is much brighter than that of the dimers identified as $D_D$ objects.

Identifying both objects $D_D$ and $D_B$ as Al dimers may seem contradictory. However, we propose a hypothesis that two and more $D_D$ objects, upon neighbouring each other in a form of chain, are then imaged as $D_B$ objects. In other words, the imaging of Al dimers differs for single Al dimers and for Al dimers that are part of longer chains. The hypothesis is build the upon following assumptions and observations as follows:

1. The $D_D$ objects are Al dimers.
2. The long Al chains consist of $D_B$ objects. Thus, $D_B$ objects are Al dimers.
3. Two and more $D_D$ objects neighbouring each other in a form of a chain was never observed. Thus, there either exist an interaction that prevents such a neighbourhood (which we find unlikely) or they appear differently in such a case.

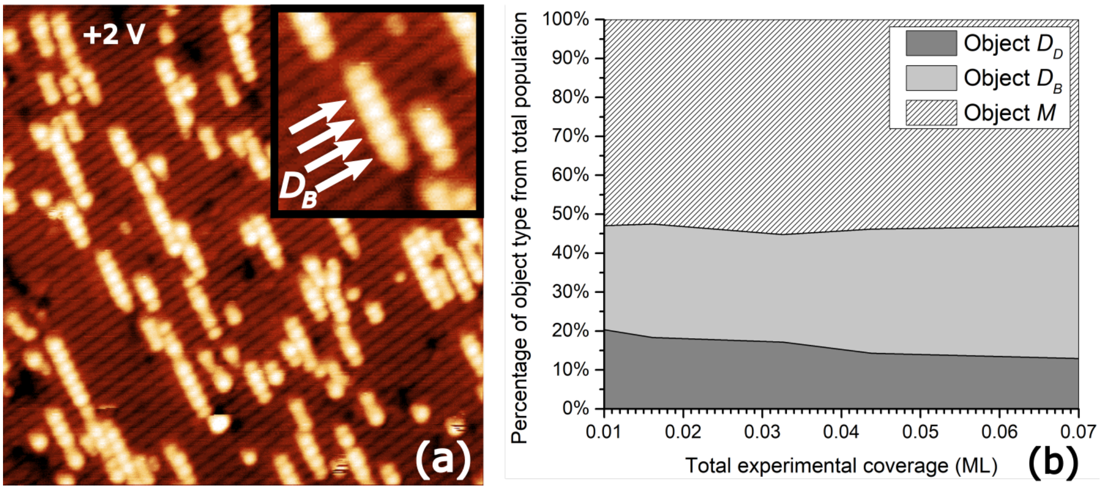

**Figure 6.19:** (a) STM image (area 25 nm × 25 nm) of 0.07 ML coverage of Al on Si(100)2 × 1 measured at RT. The sample voltage: $U_S = +2$ V and the tunneling current: $I = 0.3$ nA. At this coverage there are long Al chains predominantly formed by $D_B$ objects. The inset shows close-up of Al chain with $D_B$ objects marked by white arrows. (b)-(c) Single $D_B$ objects adsorbed at defected surface. (d)-(e) Imaging of neighbourhood of Al chains terminated by $M$, $D_D$ and $D_B$ objects at low scanning voltage.

The hypothesis of changed imaging may be further supported by the results presented in Figure 6.19(b). It shows the dependency of the population representation of individual objects on the total experimental coverage. With increasing coverage the representation of $D_B$ objects increases on expense of the population of $D_D$ objects, whereas the representation of $M$ objects remains the same. This can be explained exactly by the fact that the $D_D$ objects transform into $D_B$ objects. The constant representation of $M$ objects can be explained by the fact that at such a low coverages there are still enough free chain ends for $M$ objects to adsorb at.

Even though the hypothesis can explain why two or more $D_D$ objects are never observed on Si(100) surface, it does not explain why the Al dimer within a chain consisting of one dimer and one or two monomer terminations appear sometimes as $D_B$ object and sometimes as $D_D$ object [see Figure 6.14(a)-(b)]. To learn more about the imaging of Al dimers and directly prove or disprove the hypothesis, it would be needed to obtain a "life recording" (so-called in-vivo measurement) of the growth of Al chains at RT to observe the proposed imaging transition. Until then, it remains an open question.

### 6.2.2 Direct observation of single Al adatom hopping at LT

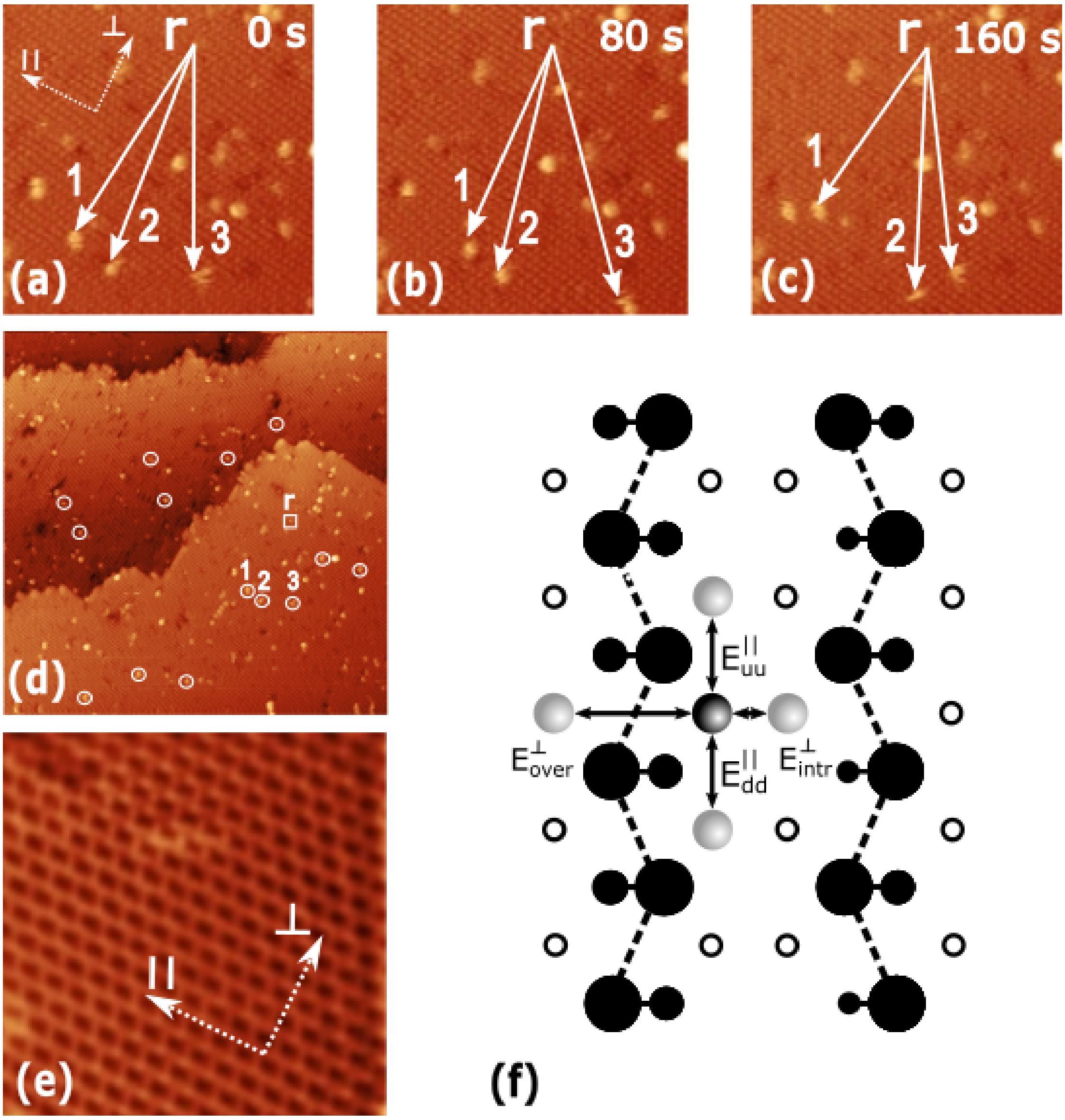

**Figure 6.20:** (a)-(c) Set of 3 STM consequent images of the same area of system Al/Si(100)-c(4×2) obtained at T = 115 K showing 3 migrating Al adatoms (scanning conditions: 50 nm × 50 nm, $U_s$ = -2 V, $I$ = 0.25 pA). (d) The investigated surface area with processed adatoms marked by white circles. (e) Detail image of the Si(100)-c(4×2) reconstruction. (f) A schema of the Si(100)-c(4×2) surface (black disks) with adsorbed Al adatom (dark gray ball). The possible adsorption sites of the Al adatom are represented by open circles/light gray balls. Possible directions for single hop of the Al adatom are indicated by black arrows together with the respective activation energies. The energy $E^{\perp}_{\mathrm{intr}}$ is related to the hops between the adsorption site lying between two Si dimer rows. The energy $E^{\perp}_{\mathrm{over}}$ is related to the hops of Al adatoms over the Si dimer row. Further $E^{||}_{\mathrm{dd}}$ is activation energy for hops between two down Si atoms and $E^{||}_{\mathrm{uu}}$ is activation energy for hops between two up Si atoms.

After having identified individual Al adatoms on the Si(100) surface, we have focused on their diffusion on the surface. Since it was found out for the system

In/Si(100)-c(4×2) that he thermally activated hopping of In adatoms dominates for temperatures above 100 K at tunneling current of 25 pA [113], we used the same preset value in all our experiments to eliminate hopping of adatoms activated by tunneling current. It was also found out that the tip voltage plays a crucial role in inducing atomic events over thermal activation for similar metals - Sn [40] and In [34, 113]. Thus, to suppress the voltage induced adatom manipulation all STM images were acquired at sample voltage $U_S = -2$ V

Figure 6.20(f) shows a schema of Si(100)-c(4×2) surface reconstruction together with Al adatom adsorption sites. In the schema there are also depicted the directions of possible Al adatom hops to neighbouring adsorption sites together with the respective activation energies for these hops. A direct consequence of the surface symmetry is the fact that the adatom has to execute at least two hops in a given direction with different activation energies in order to get to an adsorption site that is equivalent to its starting one. The lower of the two energy barriers that has to be overcome can be so small that the hopping between the respective adsorption sites can be relatively fast with respect to the scanning speed of the STM. This can result in a multiple imaging of the same adatom within one scan [112, 113, 122]. The higher of the two energy barriers plays the role of the effective energy barrier for the movement of the adatom in the given direction.

To observe and evaluate the thermally activated mobility of the Al adatoms, we employed experimentally the most straightforward technique of repetitive full STM scans of one chosen area of the sample. In Figure 6.20 there is an example of sequence of 3 consecutive STM images of an area on Si(100)-c($4 \times 2$) surface with individual Al adatoms present. An immobile reference surface defect is marked in the images by letter "r", whereas three white arrows point to the positions of three representative hopping Al adatoms. The fuzziness of the imaging of the adatoms is caused by the fact that at the experimental temperature the individual adatoms had enough energy to perform on average more than one hop between neighboring adsorption positions in time between two scans. Obtaining a good resolution of the STM images that would allow for fine observation of the surface reconstruction during the mobility studies proofed to be time demanding and thus counterproductive. By the time such a resolution was achieved, all the individual adatoms were immobile, because they were either adsorbed at surface defects or they were bound to each other creating dimers or longer chains. The reconstruction is, however, clearly visible in the zoomed STM image 6.20(e), which could only be obtained after the collection of the migration data.

We observed an anisotropy of hopping of individual Al adatoms. Their mobility was faster in the direction parallel with silicon dimer rows. This kind of anisotropy of migration of Al adatoms was expected. The expectations were based on the published calculations of the hopping barriers between two equivalent adsorption sites on Si(100)-c(4×2) performed by Albao et al. for several Group III metals including Al [52].

When the surface used for the experiments was prepared according to [114] and was virtually defect free, the fast migrating adatoms either migrated out of the visible area, adsorbed at *C*-type defects or they found another migrating adatoms and created stable dimers before their migration could have been recorded. The defected surface was found to serve our needs better. Because of the nearly exclusive movement of the single Al adatoms along one Si dimer row, it often happened that the movement remained confined between two $A$-type or $B$-type surface defects positioned on the same Si dimer row. A bordered linear area with finite number of adsorption sites, between which the trapped adatom hopped, was thus created. We have never observed the Al adatoms hopping over the limiting surface defects. In our experiments, we have recorded linear areas with sizes ranging from 6 to 85 adsorption sizes. The anisotropy was, however, not as strong as to completely prevent the movement in the direction perpendicular to the Si dimer rows and we also observed several perpendicular hops. The perpendicular hops resulted in the fast parallel movement being confined in a new linear area of new size and it sometimes resulted in termination of the adatom movement, because of its adsorption on $C$-type defect, which was present in the new linear area.

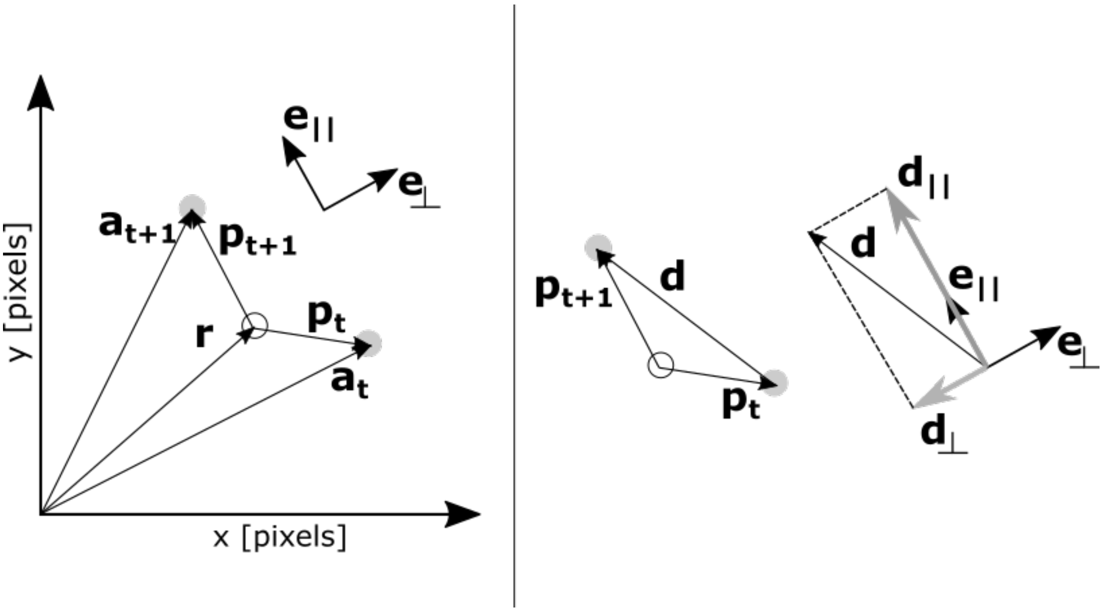

**Figure 6.21:** The schematics of process of acquiring the distance traversed by aluminium adatoms between two consecutive STM measurements. The gray circles represent the aluminium adatom and empty circle represent the reference defect. The vectors $\vec{r}$, $\vec{a_t}$ and $\vec{a_{t+1}}$ denotes the positions of reference defect, adatom position in the image in time $t$ and adatom position in consecutive image respectively. The vectors $\vec{e_{\|}}$ and $\vec{e_{\perp}}$ are the unit vectors in directions parallel and perpendicular to the silicon dimer rows. From the relative positions of the adatom measured in time $t$ and $t+1$ to the reference defect - $\vec{p_t}$ and $\vec{p_{t+1}}$ - the vector of displacement $\vec{d} = \vec{p_{t+1}} - \vec{p_{t+1}}$ is acquired. Its projections $\vec{d_{\|}}$ and $\vec{d_{\perp}}$ on the unit vectors $\vec{e_{\|}}$ and $\vec{e_{\perp}}$ gives the displacement of adatom between two consecutive measurements in directions parallel and perpendicular to the silicon dimer rows. From the known size of measured area in nm and pixels we were able to convert the hopped distance in pixels to nm and subsequently to the number of adsorption positions

Since our observations did not show any change of migration character of the Al adatoms in the vicinity of the $A$-type, $B$-type or $C$-type defects that were present in the adjacent rows, we conclude that if the adatoms felt the presence of these defects, the impact of such interaction on the hopping was of negligible margin compared to the thermal activation.

Because of the above mentioned sub-optimal quality of the STM resolution of the surface reconstruction, we were unable to determine the number of adsorption sites traveled by the adatoms in the time between two consecutive scans. To overcome this complication, instead of number of adsorption sites we have measured the direction and absolute size of the distance traveled. Making use of the known geometry of the surface, we were able to convert the measured distance into the number of adsorption positions traveled in parallel and perpendicular direction. We have estimated the accuracy of this approach to be ±1 adsorption position in each direction. This processing is described in more detail in the description of Figure 6.21.

A total of 14 adatoms were studied [see white circles in Figure 6.20(d)] and we measured approximately 30 displacements for each one of them. We made use of the approach developed by Burgess et al. [123] and later employed by Setvín et al. [113] to obtain the mean lifetime of the adatom in one adsorption position $\tau^{\parallel}$ from the distribution of the total distances traveled by the adatom in time between two observations. For a greater clarity, we will repeat the derivation here in more detail than it was presented in both mentioned articles.

We start with an assumption that movement of the adatom on the surface can be described as unrestrained 1-D random walk (further in the text we will study the impact of violating this assumption). Every single hop of the adatom during the random walk is a random event $e$ with equal probability of being either a forward hop ($e = +1$) or backward hop ($e = -1$). It easily follows that:

$$\begin{aligned} \langle e \rangle &= 0 \\ \operatorname{var}(e) &= \langle e^2 \rangle - \langle e \rangle^2 = 1 \end{aligned} \tag{6.19}$$

The total displacement $d$ of the adatom between two observations can be obtained as finite sequence of random events $e$:

$$d = \sum_{i=1}^{n} e_i, \tag{6.20}$$

where $n$ is the number of the hops realized in the time $t_{\text{scan}}$ between two observations. Number of hops $n$ is also a random variable with its expected value being:

$$\langle n \rangle = \frac{t_{\text{scan}}}{\tau^{\parallel}}. \tag{6.21}$$

Clearly the two random variables $d$ and $n$ are not independent and thus we have to start by deriving the expected value of $d$ given that $n = N$:

$$\langle d | n = N \rangle = \langle d | N \rangle = \left\langle \sum_{i=1}^{N} e_i \right\rangle = \sum_{i=1}^{N} \langle e_i \rangle = N \langle e \rangle \tag{6.22}$$

If we denote $P(N)$ the probability of number of hops $n$ being equal to $N$, then the expected value of the total displacement $d$ can be derived as follows:

$$\langle d \rangle = \sum_N P(N) \langle d | N \rangle = \sum_N P(N) N \langle e \rangle = \langle e \rangle \sum_N P(N) N = \langle e \rangle \langle n \rangle = 0. \tag{6.23}$$

To derive the variance of the total displacement $d$, we can use the law of total variance, which says that:

$$\operatorname{var}(X) = \langle \operatorname{var}(X|Y) \rangle + \operatorname{var}(\langle X|Y \rangle). \tag{6.24}$$

Applying this law and using equations (6.19), (6.21) and (6.22) we get:

$$\begin{aligned}\mathrm{var}(d) &= \langle \mathrm{var}(d|n)\rangle + \mathrm{var}(\langle d|n\rangle)\\ &= \langle \mathrm{var}\left(\sum_{i=1}^{n} e_i\right)\rangle + \mathrm{var}\left(n\left\langle e\right\rangle\right)\\ &= \langle n\rangle \mathrm{var}\left(e\right) + \mathrm{var}(n)\langle e\rangle^2\\ &= \frac{t_{\mathrm{scan}}}{\tau^{\parallel}}.\end{aligned} \tag{6.25}$$

When $t_{\mathrm{scan}} \gg \tau$ the distribution of $n$ is Gaussian. Because $t_{\mathrm{scan}}$ is a known parameter of the experiment and $\mathrm{var}(d)$ is a straightforward statistical characteristic of the measured displacements, the mean lifetime can be easily computed from the equation (6.25).

Furthermore, assuming that for the chosen tunneling conditions the influence of the STM tip on the hopping process is negligible and that the process can be considered as purely thermally activated, the mean lifetime $\tau^{\parallel}$ can be expressed as:

$$\tau^{\parallel} = \frac{1}{\nu_0}\exp\left(\frac{E_a^{\parallel}}{kT}\right), \tag{6.26}$$

where $E_a$ is activation energy for one hop between neighbouring adsorption sites, $\nu_0$ is a frequency prefactor, $k$ is Boltzmann constant and $T$ is temperature. By combining equations (6.25) and (6.26) we can derive the activation energy $E_a$:

$$E_a^{\parallel} = kT\ln\left(\frac{\nu_0 t_{\mathrm{scan}}}{\mathrm{var}(d)}\right). \tag{6.27}$$

Experimental measurements of frequency prefactor $\nu_0$ for different Group III [113] and Group IV metals [40] agreed on the value $10^{13}$ s$^{-1}$ within the margin of uncertainty. However, based on the reported uncertainties we have assumed that the interval of the possible values of prefactor is $1\times10^{10}\ \mathrm{s}^{-1} \le \nu_0 \le 1\times10^{14}\ \mathrm{s}^{-1}$. Even though we included the influence of the choice of the frequency prefactor $\nu_0$ into our analysis, if not stated otherwise, we assume throughout this subsection that $\nu_0 = 10^{13}\ \mathrm{s}^{-1}$.

Although the condition $t_{\mathrm{scan}} \gg \tau^{\parallel}$ was fulfilled for our measurements, the derived results depend also on fulfillment of the assumption that the 1-D random walk of the adatom is unrestricted, which is not valid in the case of hopping areas of finite size, where hopping adatoms reflect from the boundaries. Using the Einstein formula to express the displacement $n(t)$ in the used model of Brownian motion, we get $\langle n(t)^2\rangle = 2DT$, where $D$ is diffusion constant and $t$ is time. It follows that the measurements cannot be interpreted correctly by means of equation (6.25) when the diffusion of the adatoms is so high that $\sqrt{\langle n(t)^2\rangle}$ is larger than the length of the investigated hopping area.

The fulfillment of the condition of unrestricted 1-D random walk would theoretically require infinite size of the linear area in which the adatom moves. Effectively it would be, however, sufficient if the area is large enough with respect to the average number of hops of adatom in time between two scans [see equation (6.21)]. In such a case the activation energy, which defines the hopping rate by equation (6.26) ("real activation energy"), would be equal to the activation energy computed from the character of the random walk by equation (6.27) ("computed activation energy"). However, when the limited area is small with respect to the fast hopping rate, the character of the unrestricted 1-D random walk becomes distorted by repeated reflections from the boundaries and the difference between real and computed activation energies can become non-negligible.

To estimate the relation between the finite size of hopping area and the value of the activation energy calculated by equation (6.27), we have developed a simple model of the Al adatom hopping along Si dimer row between two surface defects. Lattice $1 \times N$ represented the line of $N$ adsorption sites. The adatom traveling in this lattice could randomly move by 1 position backward or forward with hopping rate $\nu = 1/\tau$, which followed the equation (6.26). The schematic representation of this 1-D restricted hopping model is shown in Figure 6.22(a). The model contains the following free parameters: size of the 1-D lattice $N$, temperature $T$, activation energy for single hop $E_a^{\parallel}$, number of "samples" (i.e. STM images) $l$ and frequency prefactor $\nu_0$.

In Figure 6.22(a) there are also shown the activation energies for hops of adatom from different adsorption positions. Worth noticing is the fact that we let the boundaries be fully reflective. This is based on our observation that in the experiments the finite areas were limited by $A$-type and $B$-type surface defects and these types of defects, in contrast to $C$-type defects, were neither reported to create preferential adsorption sites for Al adatoms nor have we ever observed such a behavior.

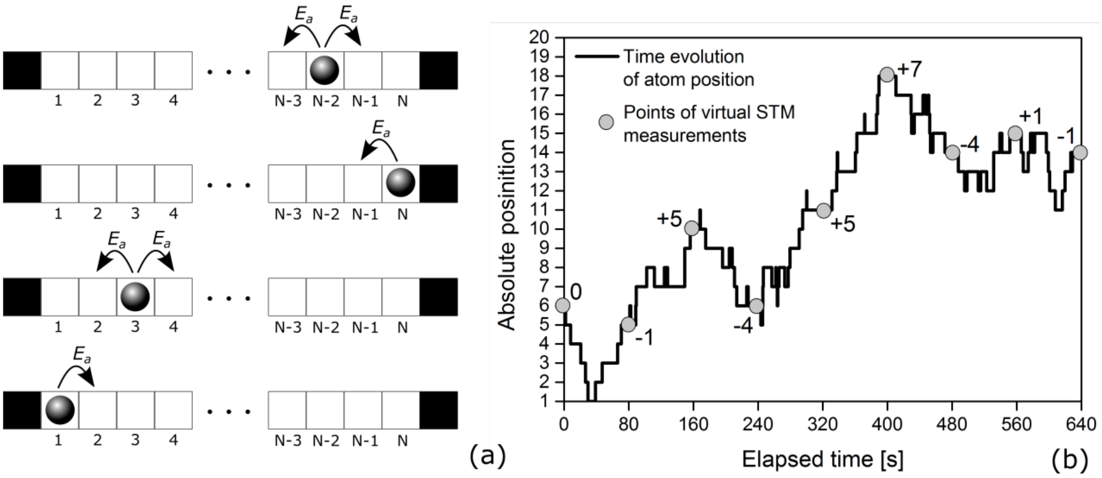

**Figure 6.22:** (a) Schematic of 1-D lattice model used to simulate the migration of an Al adatom along one Si dimer row. Each empty square represents an adsorption site. The black squares represent the reflecting ends of the finite migration area. The activation energies for hopping of adatom from different adsorption sites are also shown together with the arrows pointing in the direction of the possible hop. (b) An illustration of the time evolution of the adatom position in 1-D lattice of $N = 20$ cells. The actual positions of adatom in the lattice "measured" at 80 s time intervals are marked by gray disks. The numbers next to the disks show the relative displacement of the adatom to its previously measured position.

We further employed KMC simulations to generate the time intervals between individual hops of the adatom. From these intervals we were able to model the time evolution of the adatom position in the linear lattice. To imitate the data acquirement of STM measurements, we looked at the absolute positions of the adatom only at fixed times [$i \times 80$ s, where $i \in \{0, 1, 2, \ldots, l\}$] and evaluated the total displacements of the adatom between two STM observations as a difference between the observed positions. An illustration of this process is shown in Figure 6.22(b).

The temperature was set to 115 K. The energies $E_a^{\|}$ were chosen from an interval around the energy estimated from the preliminary application of the equation (6.27) on the raw experimental data [$0.25$ eV$, 0.32$ eV]. The size of 1-D areas $N$ was chosen from an interval $6 \leq N \leq 1000$ and the frequency prefactor $\nu_0$ was chosen from interval $1 \times 10^{10}$ s$^{-1} \leq \nu_0 \leq 1 \times 10^{14}$ s$^{-1}$. For a given set of parameters, the simulation started from a random position of the adatom on the lattice ($t = 0$). The adatom was then let to hop for $l \times 80$ s. All the simulated results were then averaged over 1000 independent runs and the variance of the simulated distribution was used to compute the activation energy by the equation (6.27).

We started by investigating the influence of the parameter $l$ on the variance of the displacement distribution. First, a relative uncertainty of the variance determined from the simulated data for $l = 20$ (which corresponds to the number of images in one experimentally obtained sequence) was evaluated. The resulting relative uncertainty was 50%. This result was used for assessing the uncertainties of the activation energies calculated from our measurements [see Figure 6.24(b)]. A negligible relative uncertainty of the variance was achieved for $l \geq 2000$, which was then used for our simulations and which provided also smooth investigated dependencies.

Figure 6.23 shows the results of the simulations. A strong dependency of the calculated activation energy on the size of the bounded area is clearly observable. For areas of size of several tens of cells the activation energies calculated from the distributions of total displacement significantly differs from the real activation energies used to set the adatom hopping rate. As might be expected for a given lattice size, the difference between the real and computed energy is the larger the lower is the real activation energy (i.e. the higher is the hopping speed). With growing lattice size the initial difference between computed and real activation energy diminishes and for large enough lattices the two energies are equal.

The simulated dependencies also reveal that for small lattice sizes and low real activation energies the random walk is so limited that its unique character for different hopping speeds is smeared. The processing of the distribution of total distances gives then identical computed activation energies. Direct consequence of this feature is that if the real activation energy was experimentally measured for very small lattice sizes, it would not be possible to determine its value exactly. It would be possible only to estimate its upper limit, because all lower activation energies would provide the same result (i.e. the same computed activation energy).

Because of the proved strong dependence of the calculated activation energy on the lattice size, we processed the measured random walks in such a way that we created statistical groups of the displacements occurring in linear areas of the same size. During this data processing, we took into account the fact that after a perpendicular hop the adatom finds itself in an area of new size [see Fig-

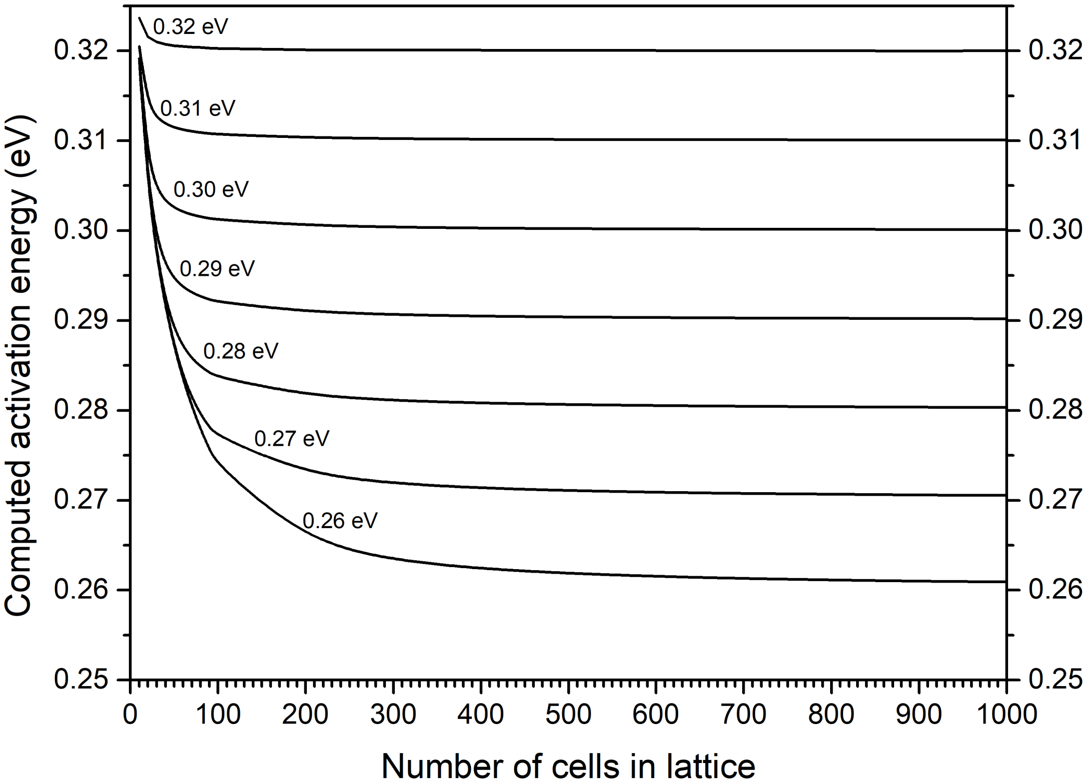

**Figure 6.23:** The results of simulating a dependency of the computed activation energy on the size of the limited area $N$ for 8 different real activation energies. The real activation energy used to set the hopping rate of the adatoms is denoted above the respective lines. The results are obtained for $\nu_0 = 10^{13}$ s$^{-1}$.

ure 6.24(a)]. We kept only the groups containing enough displacement samples ($> 20$) for further statistical calculations. The displacement distributions were then constructed for each group (i.e. linear area size) individually and the equation (6.27) was used to calculate the activation energy from the variances of the distributions. From the observation of 14 adatoms a total of 10 distinct activation energies for 10 different linear area sizes were computed [see Figure 6.24(b)]. The resulting experimental dependency of the calculated activation energy on the lattice size strongly resembles the simulated dependencies shown in Figure 6.23. By fitting the simulation results to the measured data we found the real activation energy for which the simulated dependency of calculated activation energy on lattice size best fit the experimental data. By the same process we were also able to estimate the uncertainties of the found value of the real activation energy. Because of the non-linear relation between the real activation energy and the calculated activation energy for a given lattice size, the uncertainty intervals are asymmetric. The value $E_a^{\|}$ found by the fitting is:

$$E_a^{\|} = 0.290^{+0.025}_{-0.015} \text{ eV} \tag{6.28}$$

We repeated the fitting procedure for the frequency prefactors from interval $1 \times 10^{10}$ s$^{-1}$ $\leq \nu_0 \leq 1 \times 10^{14}$ s$^{-1}$. The expected effect was confirmed by our investigations: the dependence of the $E_a^{\|}$ on the change of the value $\nu_0$ by one order is given only by the term $kT \ln(10)$. It means that an increase of the $\nu_0$ by 10 causes an increase in the $E_a^{\|}$ by $\approx 0.023$ eV and vice versa.

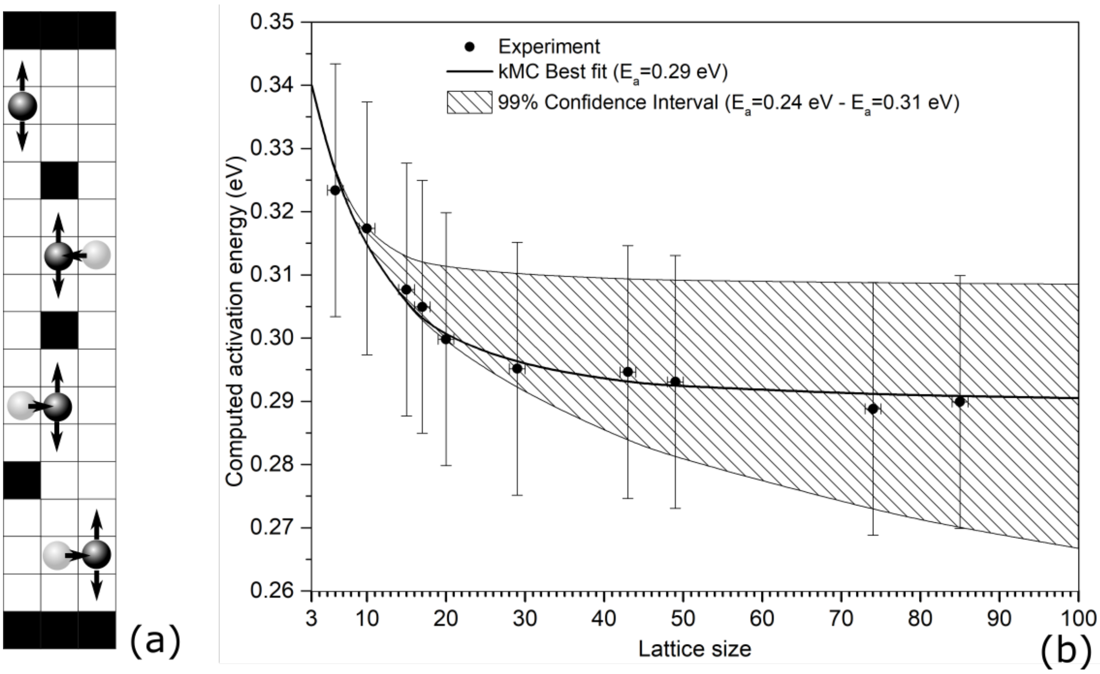

**Figure 6.24:** (a) The schematics of Al adatom changing bounded areas for parallel hopping by performing perpendicular hops. In this example the adatom switched between 4 bounded areas of considerably different sizes by 3 perpendicular hops. (b) Fitting of the experimentally measured dependency with kMC simulations results. The best fit, the lower and upper bound fits are all plotted in the graph.

Within the margin of uncertainty and within the interval of reasonable frequency prefactors, the obtained value of $E_a^{\|}$ is in a good agreement with the values 0.303 eV and 0.300 eV, which were theoretically calculated in [52] and [45] respectively.

Further illustration of how the violation of the assumption about unrestricted random walk influence the data is shown in Figure 6.25(a). The distribution of all adatom displacements, regardless of the size of linear area in which the hopping was observed, is plotted there. If $t_{\text{scan}} \gg \tau^{\|}$ then $\langle n \rangle \gg 1$ [see equation (6.21)] and distribution of $d$ [see equation (6.20)] should converge to Gaussian distribution. Even though this condition was fulfilled, the experimental distribution overshoots the normal distribution at 0 and has heavier tails. This is the impact of violating the unrestricted random walk assumption. However using the found activation energy and plotting the simulated distribution of adatom displacements regardless of the size of linear area reproduces the experimental distribution exceptionally well.

Despite the anisotropic character of Al adatom movement with preferred direction being the one parallel with Si dimer rows, the frequency of hops in perpendicular direction was not negligible and we were able to measure 41 individual perpendicular hops. Thus we obtained 41 measurements of lifetimes of Al adatom in adsorption site before it moved to neighbouring adsorption site via perpendicular hop. Since the hopping of Al adatom at given temperature is defined by two constant hopping rates - one in parallel and one in perpendicular direction - the hopping in each direction can be described as Poisson process. The probability that the adatom will not move from the adsorption position in time interval $(0, t)$

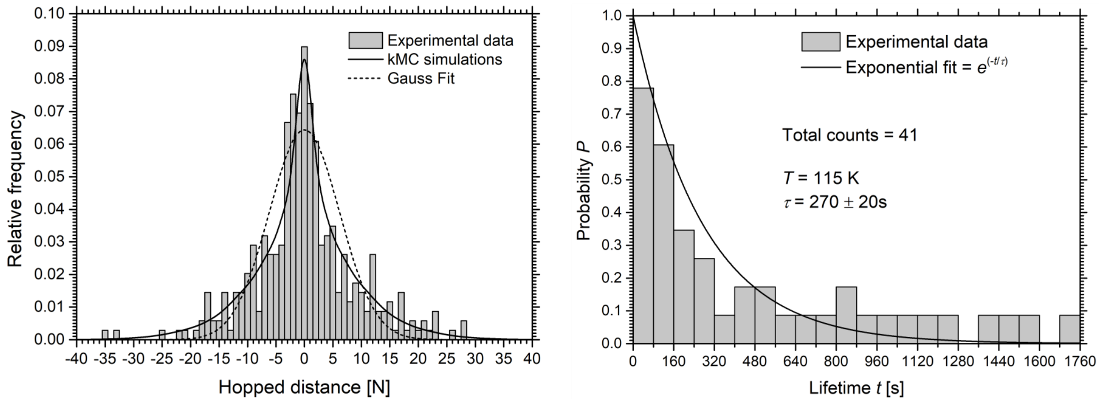

**Figure 6.25:** (a) Comparison of measured distribution of hopped distances with distribution obtained by kMC simulations (using the activation energy for parallel hops $E_a^{\parallel} = 0.29$ eV) and with Gauss fit. (b) Histogram of adatom lifetimes in adsorption positions before undergoing perpendicular hop. The fit of this distribution with function (6.29) is shown.

via perpendicular hop is then expressed as:

$$P(t) = \exp\left(-\frac{t}{\tau^{\perp}}\right) \tag{6.29}$$

We fitted the histogram of time intervals between individual perpendicular hops (i.e. lifetimes) by function (6.29) in order to obtain the mean lifetime $\tau^{\perp}$. The results can be seen in Figure 6.25(b). Equation (6.26) was used to calculate the activation energy for perpendicular hop from the the mean lifetime $\tau^{\perp}$. Taking into account that the uncertainty of temperature measurement was ±3 K, the resulting activation energy is:

$$E_a^{\perp} = 0.35 \pm 0.05 \text{ eV} \tag{6.30}$$

Due to a small size of the experimental sample, the fit in Figure 6.25(b) does not seem as a perfect one. We also calculated the arithmetic mean of the measured lifetimes to challenge the value of $\tau^{\perp}$ obtained via fitting. We obtained value $\tau^{\perp} = 520 \pm 160$ s. Even though there is a significant difference between this value and the one obtained via fitting, it produces practically identical activation energy within the margin of uncertainty: $E_a^{\perp} = 0.36 \pm 0.05$ eV.

Until now we have presumed that we have registered all the perpendicular hops. It is however possible that during one image acquisition a perpendicular hop is followed by another one in opposite direction. Such a chain of events would result in missing the perpendicular hop. Since we have already expressed the probability that the adatom will not move from the adsorption position in time interval $(0, t)$ via perpendicular hop by equation (6.29), we can easily derive the probability $P_{\text{miss}}$ of the just described missing observation during one STM image acquisition:

$$P_{\text{miss}} = \frac{1}{2T} \int_0^T \left[1 - P(t)\right]\left[1 - P(T - t)\right] \mathrm{d}t, \tag{6.31}$$

where $[1 - P(t)]$ expresses the probability of perpendicular hop happening in time interval $(0, t)$ and $[1 - P(T - t)]$ expresses the probability of second perpendicular hop happening in time interval $(t, T)$. Two consecutive perpendicular hops give 4 possible combinations of resulting displacement from which only two combinations result in 0 displacement. Because of that there is the factor 1/2 in the equation.

After integrating the equation (6.31) we get:

$$P_{\text{miss}} = \frac{1}{2}\left(1 + e^{-\frac{T}{\tau^{\perp}}}\right) - \frac{\tau^{\perp}}{T}\left(1 - e^{-\frac{T}{\tau^{\perp}}}\right) \tag{6.32}$$

Substituting the values of $T$ and $\tau^{\perp}$ into the equation (6.32), we get $P_{\text{miss}} = 0.18\%$ for $\tau^{\perp} = 520$ s and $0.63\%$ for $\tau^{\perp} = 270$ s. These results show that the occurrence of missed perpendicular hops can be neglected.

Both activation energies - $E_a^{\parallel}$ and $E_a^{\perp}$ - were theoretically calculated in [52]. Whereas the value of activation energy $E_a^{\parallel}$ estimated from our experiments is in agreement with the prediction, the experimentally obtained value of the activation energy $E_a^{\perp}$ (0.35 eV) differs significantly from the calculated one (0.466 eV) even at the upper uncertainty bound and within the interval of reasonable frequency prefactors. It is worth noting that for the theoretically calculated activation energies, the hopping rate at the temperature 115 K in parallel and perpendicular direction would differ by approximately 7 orders. In such a case, the simultaneous observation of parallel and perpendicular hops during the duration of one experiment would be, contrary to our observations, impossible.

### 6.2.3 Growth characteristics of Al structures

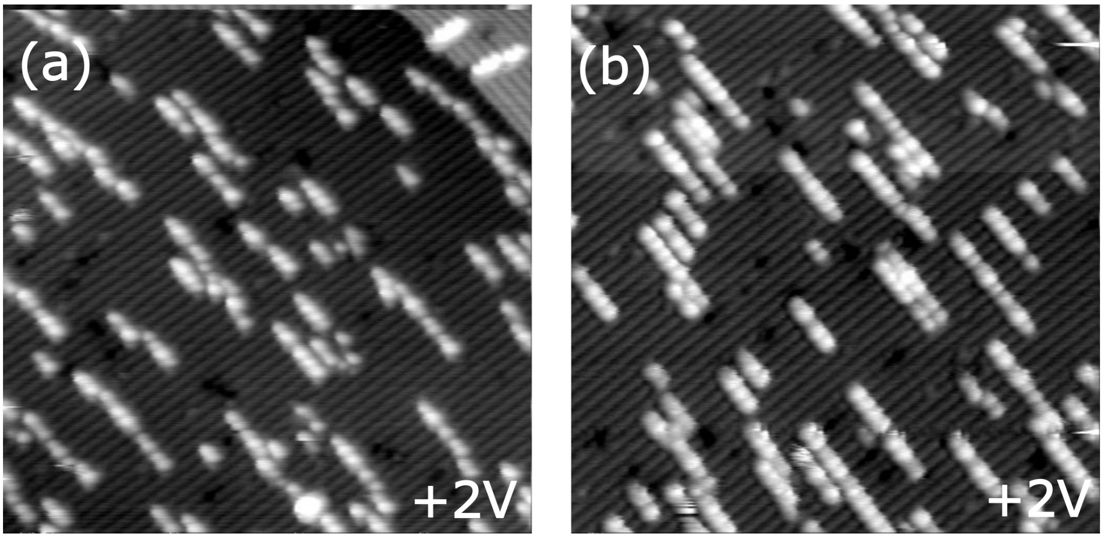

**Figure 6.26:** Visual comparison of the density of kinks for Al structures grown at RT [picture (a)] and after heating the sample to 450 K [picture (b)].

Unlike other Group III metals (In, Ga) and Group IV metals (Sn), the Al chains grown at RT have tendency to create groups of short chains adjoining each other diagonally [see Figure 6.26(a)]. In this work, we call this kind of diagonal adjoining a "kink". The group of diagonally neighbouring chains is called an "island" and the individual branches of the islands are called the "chains". The long and straight Al chains can be obtained not only by growing the Al structures at elevated temperatures, but also by heating the sample with Al structures grown at RT [see Figure 6.26(b)], which shows, among other things, that the diagonal neighbouring of the chains is not very stable.

In Section 6.2.1 the Al dimers and monomers were identified in STM images. Thus, we were able to unequivocally identify the Al objects forming the kink and subsequently describe it as Al monomer that can alternately attach to each of the two diagonally neighbouring chains. Figure 6.27(e) shows a simplified structure of the kink. By repeatedly scanning several Al islands for an extensive time at RT, we were able to record the movement of the Al monomers within the kinks [see Figure 6.27(a)-(d)]. We were able to observe several back and forth changes of the kink's position without the hopping Al monomer detaching from the whole island and migrating away. It shows that the energy barriers in the vicinity of the Al monomer within the kink are changed in such a way that:

1. The monomer is able to detach from the chain termination.
2. The hopping of the Al adatom is favored in the direction in which the diagonally adjacent chain termination is located.

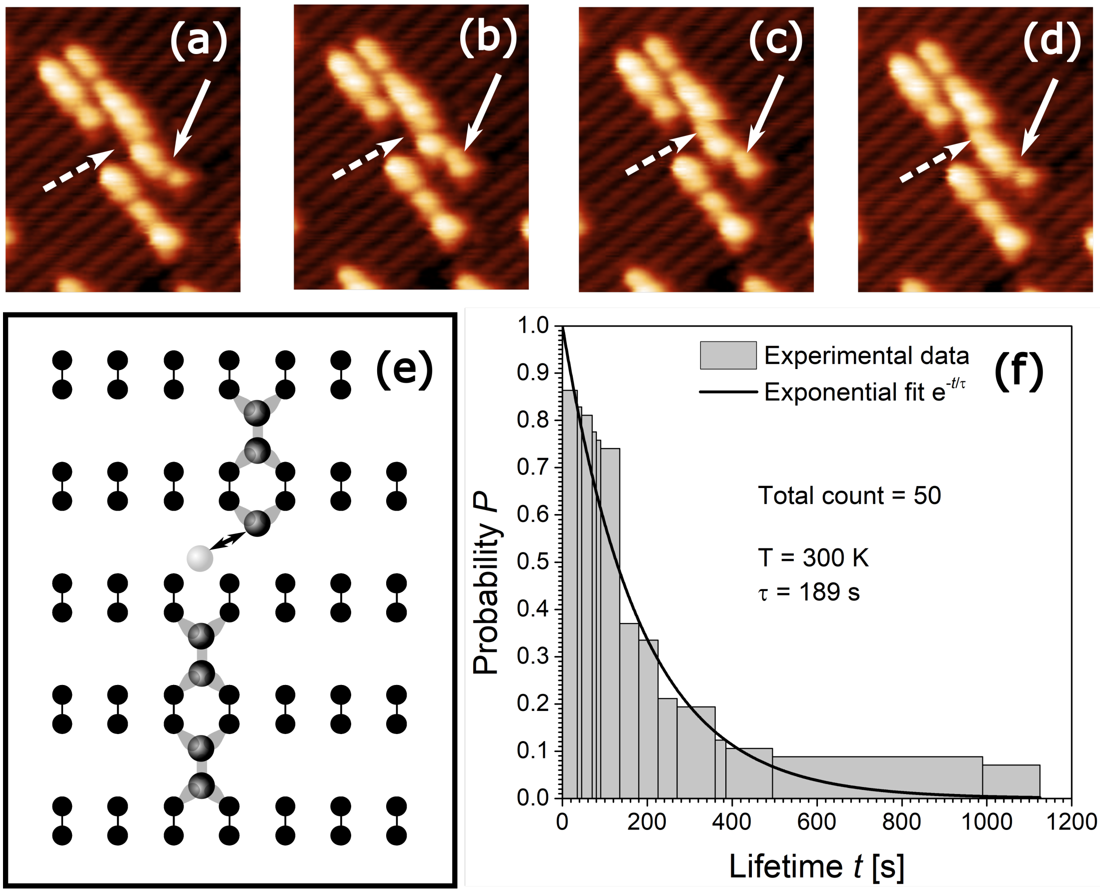

**Figure 6.27:** (a)-(d) A sequence of STM images showing a switching of Al monomers in two kinks (marked by white straight and dashed arrows). (e) A schematic drawing of a kink structure. (f) Histogram of kink lifetimes in adsorption positions before undergoing a switch. The fit of this distribution with function (6.29) is also shown.

We gathered 50 measurements of the lifetimes of Al adatom in adsorption site before it moved to a new position within the kink. We used the same method as to obtain the activation energies for perpendicular hops of Al adatoms on Si(100)-c($4 \times 2$) surface. We fitted the normalized distribution of time intervals between individual hops within the kink (i.e. lifetimes) by function (6.29) in order to obtain the mean lifetime $\tau_{\mathrm{kink}}$. The results can be seen in Figure 6.27(f). Equation (6.26) was used to calculate the activation energy for hop within the kink from the mean lifetime $\tau_{\mathrm{kink}}$. The resulting activation energy is:

$$E_a^{\mathrm{kink}} = 0.92 \pm 0.03 \text{ eV} \tag{6.33}$$

Due to a small size of the set of the experimental observations, the fit in Figure 6.27(f) did not seem as a perfect one. We also calculated the arithmetic mean of the measured lifetimes to challenge the value of $\tau_{\mathrm{kink}}$ obtained via fitting. We came to the value $\tau^{\mathrm{kink}} = 213 \pm 20$ s. This value corresponds within the margin of uncertainty to the one obtained via fitting. It also produces identical activation energy: $E_a^{\mathrm{kink}} = 0.92 \pm 0.01$ eV. Using the equation (6.32), we made sure that missed hops within the kink due to fast consecutive hops back and forth were not an issue.

Focusing next on the statistical characteristics of the Al structures, we have executed a number of experiments to obtain the characteristics for various coverages and different evaporation rates (see Table 6.4). Since the evaporation source of Al was several tens of centimeters away from the sample, we have considered the initial concentration of $C$-type defects at the beginning of the experiments constant as in case of Sn.

The usual size of the investigated areas on the Si(100)-($2 \times 1$) surface was (50 nm × 50 nm). This size was found to be optimal, because it provided large enough field of view to register terraces with $\approx 150 \times 150$ adsorption sites and at the same time allowed us to distinguish individual dimers in the chains. To exclude the influence of the surface step edges on the growth, we have chosen only the terraces that were much wider than an average length of chain.

At the beginning we have ignored the existence of the kinks and processed the branching chains as individual objects (i.e. we have ignored the grouping of Al chains into islands). During none of our experiments have we ever observed a change of the size of the chains. Thus, we conclude that the growth of Al chains at RT is irreversible. We can support our statement also by the results of DFT calculations of adsorption energies of Al adatoms in the chains published in [117]. It follows from the published adsorption energies that the difference between the adsorption energy of single Al adatom on Si(100) and Al adatom bound in a dimer is 1.5 eV. The difference between the adsorption energy of the single Al adatom and Al adatom bound as a monomer termination of Al chain is 0.75 eV. After breaking the bond, the adatom has to also overcome a hopping barrier of several tenths of eV to detach from the chain's termination completely. From the mean life times of the chain's termination calculated by the equation (6.1), we can also conclude that the growth of Al chains is irreversible at RT.

We showed in Subsection 6.2.1 that we are able to identify Al monomers and dimers and thus determine with atomic precision the lengths of individual chains and sizes of Al islands. However, the same argument, which was presented for similar problem concerning Sn chains, is valid for Al - acquiring a resolution that enables the identification of individual types of Al objects requires high quality STM tip and also a large amount of experimental time, which is not optimal if voluminous statistical sets of images are to be collected. Thus, we have assumed that all the chains (and islands) are formed only of dimers and have only even number of adatoms. Because the high-resolution images showed that the chains have equally likely odd or even termination, the impact of our assumption on the uncertainty of the acquired statistical characteristics should average out as in case of Sn.

In Subsection 6.2.1 it was shown that the $C$-type defects act as preferred adsorption sites for migrating Al adatoms. In Subsection 6.1.2 it was also shown that coverages of $C$-type defects as small as 0.0015 ML non-negligibly influence the character of the growth of Sn on the Si(100) surface. From the values presented in Table 6.4, several observations concerning this issue for Al could be made:

1. The percentage of occupied $C$-type defects in case of Al is approximately twice as high as in case of Sn.
2. The percentage of the chains anchored to $C$-type defects in case of Al is, on the other hand, approximately twice as low as in case of Sn.
3. Sn chains are approximately three times longer than Al chains

It can be concluded from the point 1 that the Al adatoms are bound to the $C$-type defects more strongly than Sn adatoms. Because the growth of both Al and Sn is irreversible at RT, point 3 shows that the Al adatoms are less mobile on Si(100) (i.e. the activation energies for hopping of individual adatoms are higher in case of Al). This conclusion is also in agreement with the point 2 - even though the Al adatoms are bounded to the $C$-type defects more strongly than Sn adatoms and higher concentration of Al chains nucleated on $C$-type defects could be expected, their slow hopping on the surface causes them to meet another hopping Al adatom with higher probability than nucleating on the $C$-type defect. As a result, vast majority of the Al chains (approximately 80%) grow on the Si(100) surface at RT as if it was defect-free. Thus, the $C$-type defects probably do not significantly influence the character of the growth of Al chains.

| $\Theta$ (ML) | Deposition rate (ML/s) | $\langle s_{\mathrm{ch}} \rangle$ | $\langle s_i \rangle$ | Chains on $C$-type defects | Occupied $C$-type defects | $\Theta_C$ (ML) | $N$ |
|---|---|---|---|---|---|---|---|
| 0.044 | 0.00025 | 4.37 | 5.74 | 21% | 82% | 0.0030 | 491 |
| 0.059 | 0.00022 | 5.12 | 8.47 | 18% | 85% | 0.0025 | 454 |
| 0.030 | 0.00010 | 4.40 | 5.76 | 28% | 79% | 0.0035 | 442 |

**Table 6.4:** Statistical characteristics of Al chains for different deposition rates and coverages of Al adatoms. $\langle s_{\mathrm{ch}} \rangle$ is the average chain length computed from the individual branches of the islands, $\langle s_{\mathrm{i}} \rangle$ is the average size of branching islands and $N$ is total number of investigated chains. Ratio of the chains terminated on $C$-type defects is normalized with respect to total number of chains. The experiments are referenced in the text in the same order as they are listed in this table.

Figures 6.28(a)-(c) show histograms of the chain length distributions for all three experiments together with the scaled chain length distributions in Figure

6.28(d). The distributions for each experiment contain data of approximately 500 chains.The data were obtained from approximately 10 STM images, which were taken from different surface areas two hours after the deposition.

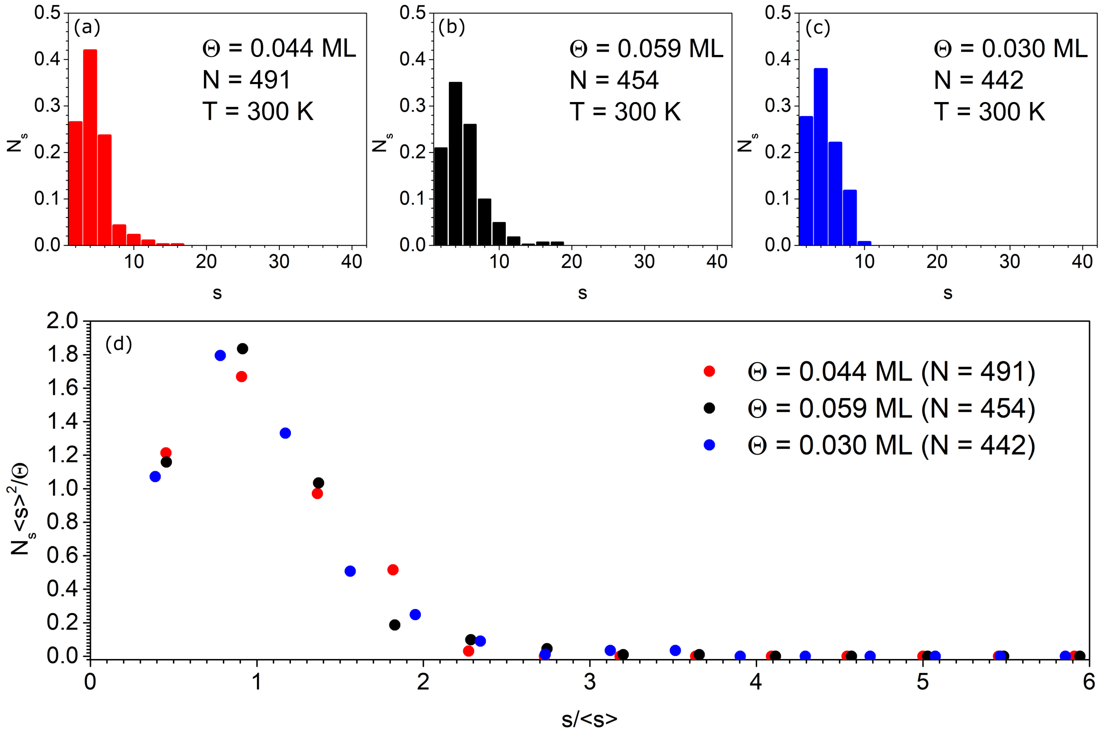

**Figure 6.28:** (a)-(c) Chain length distributions for 3 different experimental conditions (deposition rate, deposition time, concentration of defects etc.). The order of the histograms correspond with the order of the experiments in the Table 6.4. (d) The scaled chain length distributions for all 3 experiments. The colors of the distributions correspond with the colors used in histograms (a)-(c).

Looking at the scaled chain length distribution, we can see that it has a monomodal shape with maximum around 1 that is characteristic for irreversible growth with isotropic migration of the adatoms and negligible role of the surface defects. This shape of distribution is in direct contrast to the one obtained for growth of Sn chains. In case of Sn chains, the shape of the distribution reflected the character of the growth, which was irreversible with the strong anisotropy of migration of Sn adatoms on Si(100)-(2 × 1) surface and non-negligible role of $C$-type defects.

Additionally to the analysis of the chain lengths, we also processed the Al islands. Figure 6.29(a) shows the scaled island size distribution. Although the position of the peak is moved to the left from 1 and the peak itself is narrower [compare with Figure 6.29(b) and see Figure 6.29(c)-(d)], the shape of the scaled island size distribution is - within the margin of the statistical uncertainty - the same as the distribution for individual chains. We concluded that the existence of the kinks does not significantly change the character of the growth of Al chains.

Having gathered the growth characteristics presented in Table 6.4 together with the scaled chain length distributions shown in Figure 6.7, we had enough experimental information that could have been compared with the results of the KMC simulations described in Chapter 5. Whereas for Sn we were able to fix all

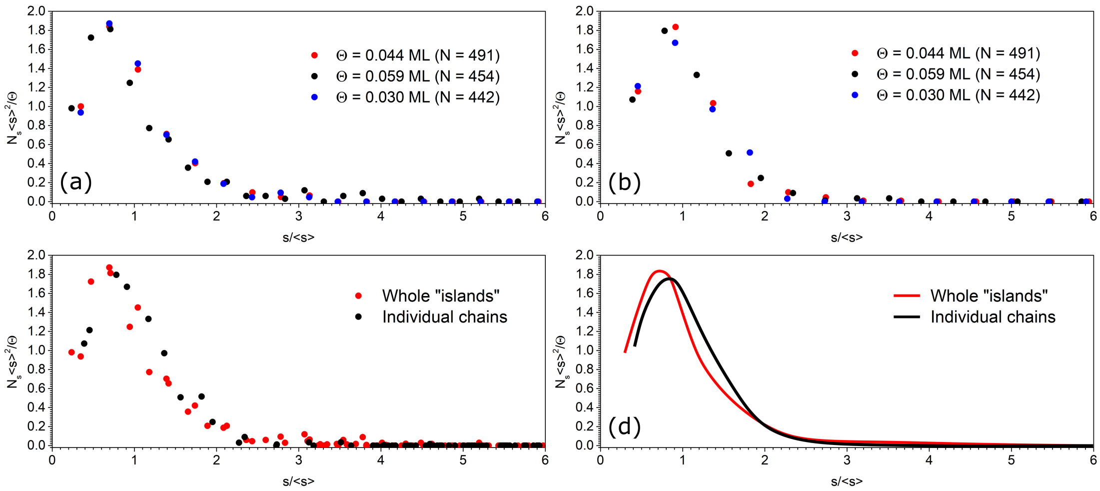

**Figure 6.29:** Comparison of scaled distribution of (a) whole islands and (b) individual chains. (c) The two distributions put into one graph for better comparison. (d) The two distributions put into one graph represented by smoothed lines.

but 3 model parameters by values either defined by the setup of the experiment or by values directly obtained from the experiment, for Al we have faced the following problems (our decisions how to solve the problems are also listed):

1. Having compared the average chain lengths, we already concluded that the activation energies for hopping of Al adatoms at RT should be higher than the energies for Sn obtained in Section 6.1.2. The same reasoning can be done for comparison of Al and In on the basis of the results publish in [39]. As a result, both energies - $E_a^{\perp}$ and $E_a^{\parallel}$ - should be in case of Al roughly larger than 0.64 eV. The values of $E_a^{\perp}$ and $E_a^{\parallel}$ obtained in the previous Section are, however, much smaller. Since they were obtained from experiments executed on the Si(100)-c($4\times 2$) surface at LT, the main reason for this discrepancy is probably the fast flip-flop motion of the Si dimers at RT, which non-negligibly influences the potential energy surface. Thus, we found the experimentally obtained values of $E_a^{\perp}$ and $E_a^{\parallel}$ unsuitable for RT simulations.
   **Solution/Decision:** We decided to use the parameters $E_a^{\perp}$ and $E_a^{\parallel}$ again as the tunable parameters of the model with lower limit 0.60 eV.

2. Incorporating kinks into our lattice gas model would require our detailed understanding of the formation of the kinks (e.g. the preferred adsorption positions during the growth, which we do not know) and it would also introduce new free parameter to the model and increase its complexity.
   **Solution/Decision:** Since we have already concluded that the presence of the kinks does not significantly influence the character of the growth, we have decided not to include them into our model.

3. We possessed neither the experimentally measured activation energies for detachment of monomer and dimer terminations from the chains nor the binding energies of these terminations. We also did not have the activation energies for detachment of Al adatom from $C$-type defect.
   **Solution/Decision:** We derived the binding energies of monomer ($E_{\mathrm{MD}}$)

and dimer ($E_{\mathrm{DD}}$) terminations from the differences between adsorption energies of single Al adatom and adsorption energies of monomer and dimer terminations, which were presented in [117]. In the same way, we have obtained the binding energy of Al adatom to $C$-type defect ($E_{\mathrm{C}}$). The binding energy of adatoms in the bridge structure ($E_{\mathrm{MM}}$) was taken from [61].

As a result of our assumptions and simplifications listed above, we were able to assign a fixed/known value to all but 2 parameters of the model - $E_a^{\|}$ and $E_a^{\perp}$. Notice that we again used the same value of the frequency prefactor $\nu_0$ for all the thermally activated processes as in the case of Sn:

$$\begin{aligned}
E_a^{\|} &> 0.60 \text{ eV} \\
E_a^{\perp} &> 0.60 \text{ eV} \\
E_{\mathrm{MM}} &= 1.48 \text{ eV} \\
E_{\mathrm{DD}} &= 5.80 - 4.30 = 1.50 \text{ eV} \\
E_{\mathrm{MD}} &= 4.30 - 3.55 = 0.75 \text{ eV} \\
E_{\mathrm{C}} &= 4.30 - 3.55 = 0.75 \text{ eV} \\
\nu_0 &= 1 \times 10^{13} \text{ s}^{-1}
\end{aligned} \tag{6.34}$$

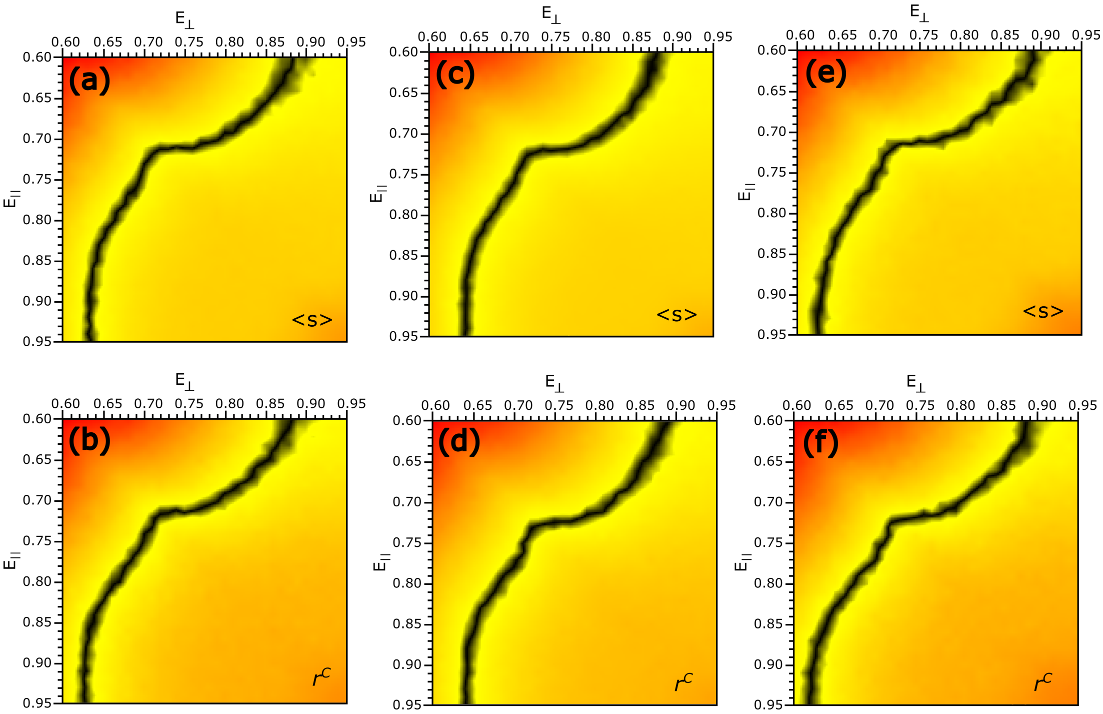

**Figure 6.30:** Diagrams of the best agreement between the simulated and the experimentally measured values of $\langle s \rangle$ and $r^C$. Figures (a)-(b), (c)-(d) and (e)-(f) correspond to the first, second and third experiment listed in the Table 6.4 respectively.

We ran the simulations of the growth of the Al on Si(100) at RT individually for the three presented experiments with the model parameters being always in agreement with the experimental ones. We collected a set of growth characteristic from the simulated layers and for three of them (average chain length, ratio of chains nucleated on $C$-type defects and chain length distribution) studied their deviation from the experimentally observed values for different combinations of $E_a^{\|}$, $E_a^{\perp}$. The deviations $D$ of the simulations from the experiments were calculated in the same way as in case of Sn [see equations (6.14), (6.15), (6.16)].

Following the same procedure as in case of Sn, we plotted the dependencies of the deviations $D$ on the combinations of $E_a^{\|}$, $E_a^{\perp}$. In Figure 6.30 the diagrams for deviations $D_{\langle s \rangle}$ and $D_{r^C}$ are shown. The minimum paths of $D_{\langle s \rangle}$ and $D_{r^C}$ are nearly identical. This is in contrast with the results obtained for Sn, where the two minimum paths for $D_{\langle s \rangle}$ and $D_{r^C}$ were completely different. It shows that in case of Al, the growth characteristic $r^C$ brings no new information about the growth kinetics than is already brought by the average chain length $\langle s \rangle$. Thus, it confirms our previous conclusion that the role of the $C$-type defects will be negligible during the growth of Al chains on Si(100)-(2 × 1).

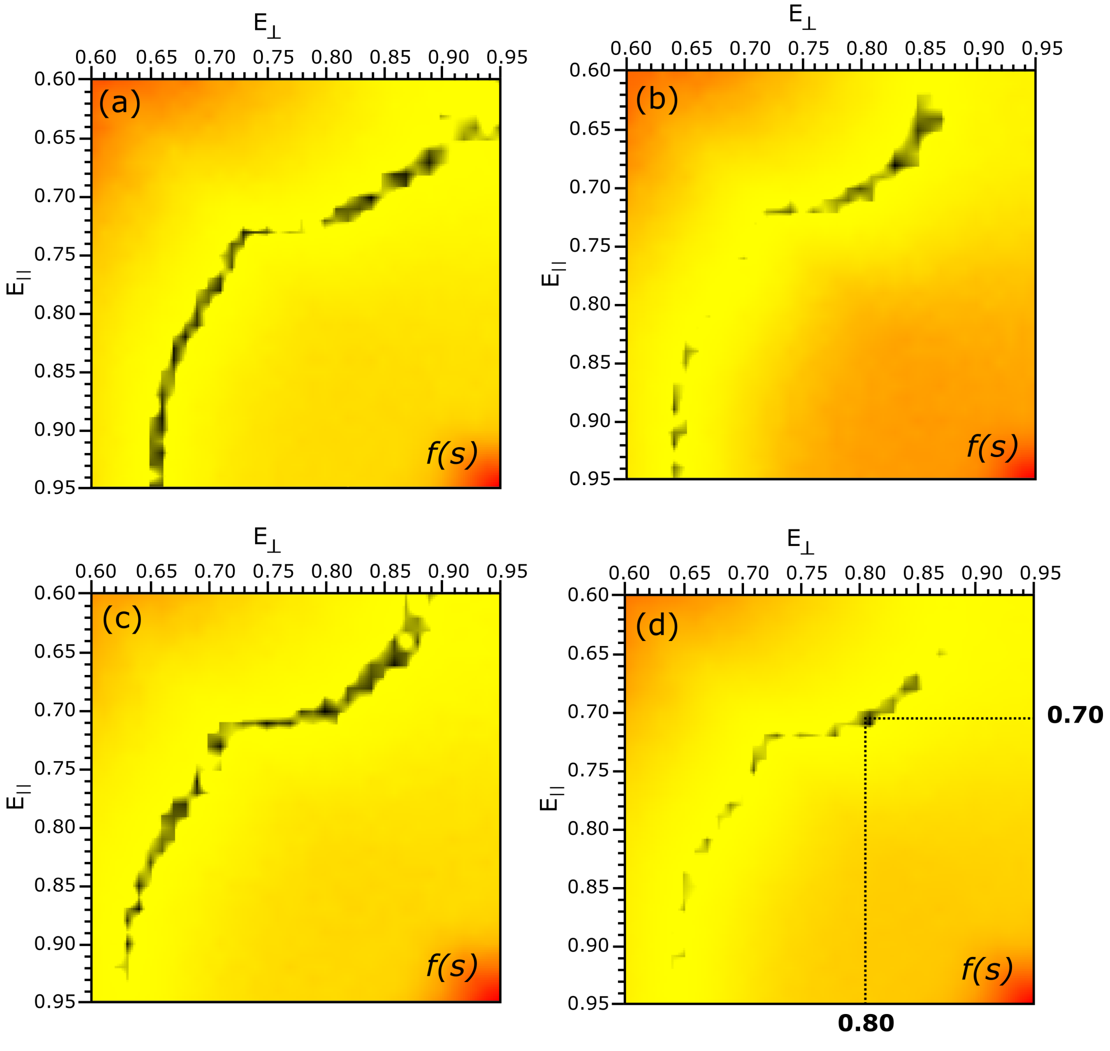

**Figure 6.31:** (a)-(c) The diagrams of deviations $D_f$ for the first, second and third experiment listed in the Table 6.4 respectively. (d) The result of superimposition of the diagrams (a)-(c) with the "coordinates" $E_a^{\|}$ and $E_a^{\perp}$ shown for the resulting global minimum.

In Figure 6.31(a)-(c) there are shown the diagrams of $D_f$. Even though there is a global minimum of $D_f$ in each diagram, it is very shallow and the area of local minima with very close values spans along the minimum path of $D_{\langle s \rangle}$.

Superimposing individual $D_f$ diagrams, however, emphasizes the unique global minimum [see Figure 6.31(d)] for the whole set of simulations. The combination of $E_a^{\parallel}$ and $E_a^{\perp}$ corresponding to this point is:

$$\begin{aligned} E_a^{\parallel} &= 0.70 \pm 0.05 \text{ eV} \\ E_a^{\perp} &= 0.80 \pm 0.05 \text{ eV} \end{aligned} \tag{6.35}$$

Figure 6.32 shows the comparison of the simulated chain length distributions with the experimentally measured ones for this obtained combination of $E_a^{\parallel}$ and $E_a^{\perp}$. It also shows the comparison of the resulting scaled distributions. In Figure 6.33 we further present the comparison of the measured STM images with the simulated grown structures of Al on Si(100)-(2 × 1) at RT. It is clear from the images that the model does not simulate correctly the formation of the kinks and Al islands. The formation of several kinks in our simulations was caused only by pure chance by two growing Al chains meeting each other diagonally.

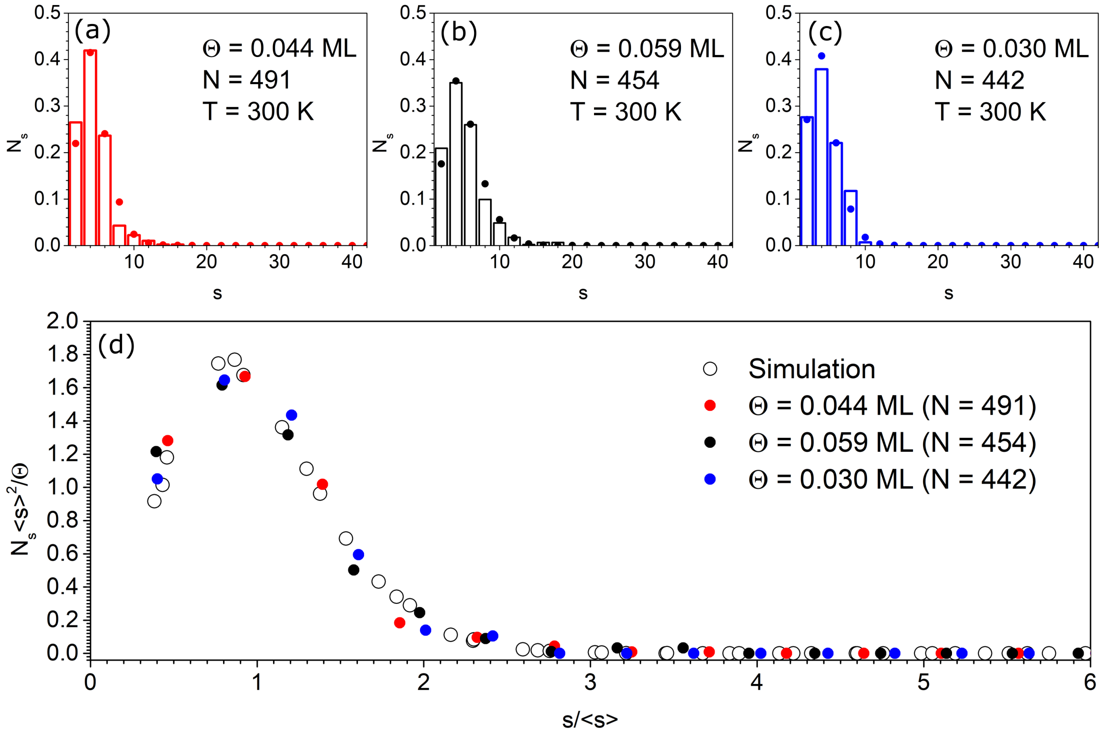

**Figure 6.32:** (a)-(c) Comparison of the simulated histograms of chain lengths with the experimentally measured ones. (d) The scaled chain length distribution of all experiments compared with the simulated one.

The results from the equation (6.35) show that hopping of Al adatoms on Si(100)-(2 × 1) is anisotropic. By comparing the hopping rates for parallel and perpendicular hops for Sn and Al adatoms (calculated from the activation energies and using the same frequency prefactor $\nu_0 = 1 \times 10^{13}$ s$^{-1}$), we can, however, de-

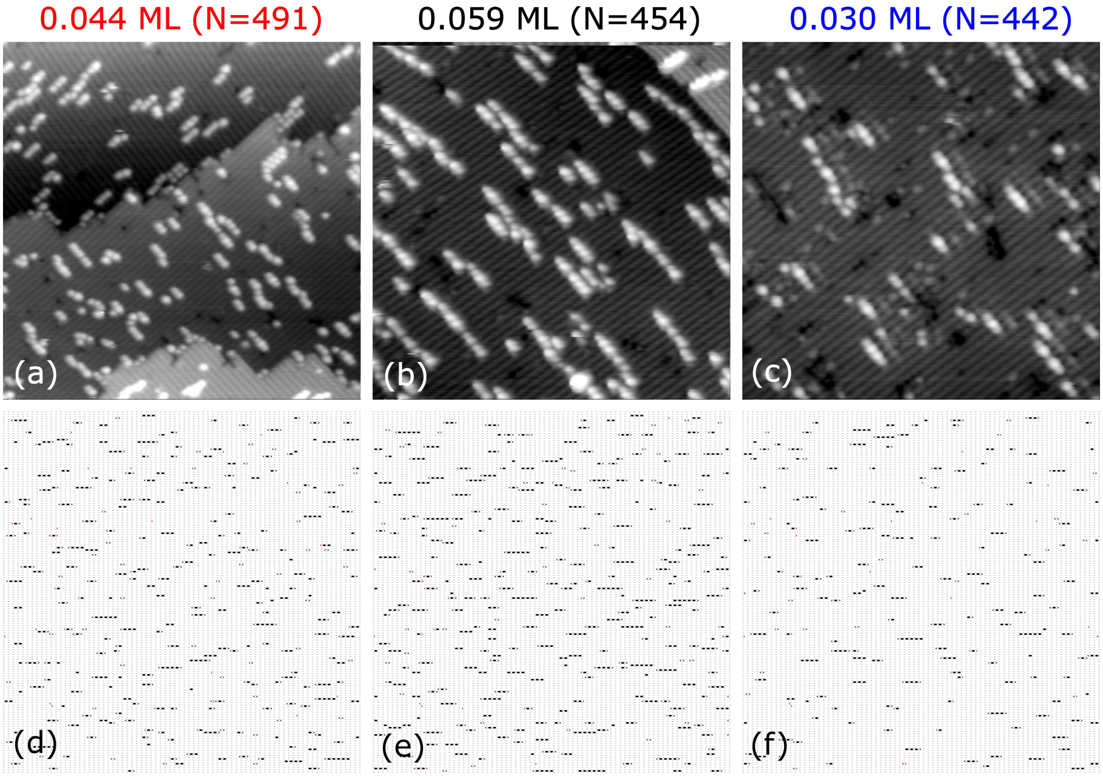

**Figure 6.33:** Comparison of the measured STM images of all three experiments with the simulated grown structures.

scribe the hopping of Al adatoms at RT as weakly anisotropic or nearly isotropic:

$$\begin{aligned} \text{Sn:}\ \frac{\nu^{\parallel}}{\nu^{\perp}} &= \exp\left(\frac{E_a^{\perp}-E_a^{\parallel}}{kT}\right) = \exp\left(\frac{0.66-0.40}{kT}\right) = 23000 \\ \text{Al:}\ \frac{\nu^{\parallel}}{\nu^{\perp}} &= \exp\left(\frac{E_a^{\perp}-E_a^{\parallel}}{kT}\right) = \exp\left(\frac{0.80-0.70}{kT}\right) = 48 \end{aligned} \tag{6.36}$$

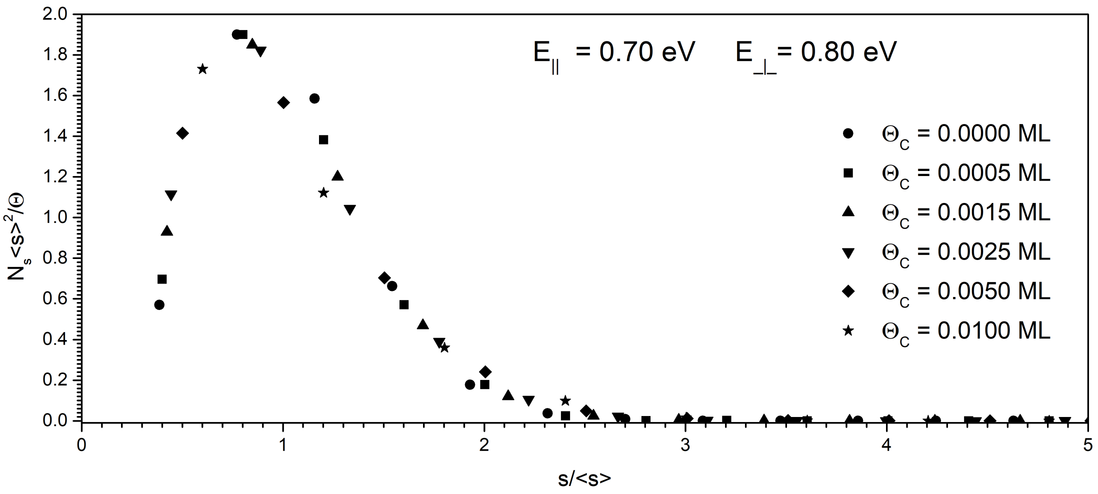

**Figure 6.34:** Comparison of the simulated scaled chain length distributions for various coverages of *C*-type defects. The choice of the parameters is the same as for the experiment listed as the third one in Table 6.4.

To eventually demonstrate that the concentration of $C$-type defects has indeed negligible impact on the character of the growth of Al chains on Si(100), we have run several simulations of the growth for different concentrations of $C$-type defects on the surface. Figure 6.34 shows that the scaled chain length distribution remains unchanged for coverages of $C$-type defects up to 0.01 ML.

### 6.2.4 Summary

In the previous three subsections we have presented a detail study of the stystem Al/Si(100). Based on the extensive experimental and theoretical evidence, we have identified 3 basic Al objects that can be observed by STM at RT on the Si(100)-(2 × 1) surface. An observation and identification of stable monomer terminations of Al chains is in contrast with generally accepted opinion that Al chains should be terminated only by the dimers. We have further identified two types of imaging of Al dimers - dark and bright. We have proposed a hypothesis that explains the existence of such a difference in imaging of Al dimer. Even though we were unable to provide any direct evidence for this hypothesis, we have presented several arguments that support it.

Further, we have used a real time STM observations to study an anisotropic migration of Al adatoms on Si(100)-c$(4 \times 2)$ surface at 115 K. These observations were used to determine the activation energies corresponding to faster hopping along Si dimer rows and slower hopping in perpendicular direction. Otherwise non-reactive $A$-type and $B$-type surface defects were found to serve as reflecting boundaries for hopping Al adatoms, which remained trapped within 1-D areas of limited size, because of the preferential hopping along the Si dimer rows. The presence of the reflecting defects was inevitable for successful recording of the Al adatom hopping. Next, we have used a KMC model of 1-D hopping in limited areas to investigate an influence of a finite size of a hopping area on the mean lifetime of Al adatom at an adsorption position inside the limited area. Because the experimental measurements of frequency prefactor $\nu_0$ for different Group III [113] and Group IV metals [40] agreed on the value $10^{13}$ s$^{-1}$ within the margin of uncertainty, the value was also used in our simulations. By finding the best agreement between the results of KMC simulations and experimental data, we were able to obtain the activation energy for hopping of Al adatoms along Si dimer rows. Apart from parallel hops, several less frequent perpendicular hops were also individually registered. We have derived the corresponding activation energy for hops in direction perpendicular to Si dimer rows by directly calculating the mean lifetime from the individually measured lifetimes. Our measurements yielded the following values:

$$\begin{aligned} E_a^{\|} &= 0.290^{+0.025}_{-0.015} \text{ eV} \\ E_a^{\perp} &= 0.35 \pm 0.05 \text{ eV} \end{aligned} \tag{6.37}$$

Finally, the growth characteristics of Al structures for different coverages and experimental conditions were gathered. It was observed that the Al chains create so called kinks and group into islands. The kink consists of a single Al adatom that alternately changes its position between two diagonally neighbouring Al chains. The hops of the kink adatom between the diagonally neighbouring chains were individually registered and the corresponding activation energy for these hops was derived by directly calculating the mean lifetime from the individually measured lifetimes. The value of the activation energy was found to be:

$$E_a^{\text{kink}} = 0.92 \pm 0.03 \text{ eV} \tag{6.38}$$

The KMC model introduced in Chapter 5 was further used to simulate the evolution of the system Al/Si(100)-(2 × 1) during the deposition and consecutive relaxation. By tuning two model parameters - $E_a^{\|}$ and $E_a^{\perp}$, we found the best match between the simulated growth characteristics and the measured ones for all experiments for the values presented in equation (6.39). The growth of the Al chains was found to be irreversible with nearly isotropic migration of Al adatoms. It was also shown that although the Al adatoms are strongly bound to $C$-type defects, their concentration does not influence the character of the growth. It is because of the low mobility of the Al adatoms on Si(100) surface at RT.

$$\begin{aligned} E_a^{\|} &= 0.70 \pm 0.05 \text{ eV} \\ E_a^{\perp} &= 0.80 \pm 0.05 \text{ eV} \end{aligned} \tag{6.39}$$

# 7. Conclusions

Our experiments aimed to thoroughly investigate and compare behaviour of two representative metals (Al from Group III metals and Sn from Group IV metals) on the Si(100) surface at low coverages. We focused our measurements and investigations on the identification of elementary objects of Sn and Al that can be observed during the early stages of the growth of the metal chains, on the evaluation of the hopping barriers of individual adatoms and on the evaluation of the activation energies for several elementary atomic actions such as detachment of adatoms from grown structures, etc.

For both metals, we have observed stable monomer terminations of the chains and have shown that $C$-type defects serve as nucleation centers for growth of the chains. For Sn the existence of the monomer terminations is already a generally accepted knowledge. We have, however, showed that another already documented phenomenon - buckling of the dimers within the chain caused by the close presence of another chain - can be also induced by the presence of the monomer termination. For Al it was the first time that the statement of the existence of stable monomer termination was supported by a detailed experimental evidence. Also the existence of two types of Al dimer imaging was proposed.

It was further shown that the two metals differ significantly in the character of the chains grown at RT. Whereas the Sn forms long straight chains, the Al chains tend to group into islands by forming so called kinks while neighbouring each other diagonally. We have found out that the kinks consist of one Al monomer that alternately terminates one or the other of the two diagonally neighbouring chains. We were able to estimate the activation energy for one hop within the kink by registering individual hops and evaluating the mean lifetime of the kink before the hop. The activation energy found is:

$$E_a^{\mathrm{kink}} = (0.92 \pm 0.03)\ \mathrm{eV} \tag{7.1}$$

Another significant difference between the Sn and Al that we have observed, was the stability of the chains. No detachment of the adatoms from the chains was observed for Al chains at RT and their growth can be described as irreversible. On the other hand, we have observed several detachment actions from Sn chains even at RT. Thus, we have run experiments focused on the stability of Sn chains at various temperatures. After dealing with concurrent presence of detachment and attachment of the atoms by means of probability calculations, we were able to estimate the activation energies for detachment of both monomer and dimer terminations from the Sn chains and from $C$-type defects together with the respective frequency prefactors:

$$\begin{aligned} E_a^O &= (0.88 \pm 0.08)\ \mathrm{eV} & \nu_0^O &= 3 \times 10^{13\pm1}\ \mathrm{s}^{-1} \\ E_a^E &= (1.02 \pm 0.08)\ \mathrm{eV} & \nu_0^E &= 3 \times 10^{14\pm1}\ \mathrm{s}^{-1} \\ E_a^C &= (0.86 \pm 0.08)\ \mathrm{eV} & \nu_0^E &= 3 \times 10^{12\pm1}\ \mathrm{s}^{-1} \end{aligned} \tag{7.2}$$

Even though the monomer terminations can detach from the Sn chains easily at RT, the dimer terminations are rather stable (mean lifetime for detachment is 13 600 s) and the growth of Sn chains can be also described as irreversible at RT.

For Al we have used a real time STM observations to study an anisotropic migration of the adatoms on Si(100)-c($4\times2$) surface at 115 K. Making use of non-reactive $A$-type and $B$-type surface defects to confine Al adatoms preferentially migrating along Si dimer rows in limited 1-D areas, we analyzed the distributions of hopped distances between acquirement of two consecutive STM images by joint means of statistics and KMC simulations. As a result we were able to estimate the activation energy for hops of Al adatoms in the direction parallel with Si dimer rows. Activation energy for hops in the perpendicular direction was calculated by directly registering individual perpendicular hops and evaluation the mean lifetime of the adatom before the hop. The activation energies found are:

$$\begin{aligned} E_a^{\|} &= (0.290^{+0.025}_{-0.015})\ \text{eV} \\ E_a^{\perp} &= (0.35 \pm 0.05)\ \text{eV} \end{aligned} \tag{7.3}$$

Finally we have gathered and compared several growth characteristics (including scaled chain length distribution) obtained from a number of experiments for both metals. There was a significant difference in the shapes of the scaled chain length distributions for Al and Sn.

The shape of the scaled distribution for Sn suggested that even though the growth itself is irreversible (i.e. far from equilibrium) the migration of the Sn adatoms is either strongly anisotropic or the presence of $C$-type defects on the surface non-negligibly influences the character of the growth. Both of these factors were found to be the reasons for the shape of the scaled distribution.

The shape of the scaled distribution for Al suggested that the migration of Al adatoms is isotropic or nearly isotropic and that the nucleation of Al chains on $C$-type does not influence the character of the growth, whatever the coverage of the defects. These conclusions were proven to be right by our studies.

| | **Al** | | **In** | | **Sn** | |
|---|---|---|---|---|---|---|
| | $E_a^{\|}$ | $E_a^{\perp}$ | $E_a^{\|}$ | $E_a^{\perp}$ | $E_a^{\|}$ | $E_a^{\perp}$ |
| DFT [52] | 0.305 | 0.466 | 0.269 | 0.272 | | |
| DFT [45] | 0.300 | 0.100 | | | | |
| STM [113] | | | 0.260 | 0.280 | | |
| KMC [39] | | | 0.640 | 0.640 | | |
| **STM** | **0.290** | **0.350** | | | | |
| **KMC** | **0.700** | **0.800** | | | **0.400** | **0.660** |

**Table 7.1:** Activation energies of different Group III and Group IV adatom hopping on the Si(100) surface in directions parallel and perpendicular to Si dimer rows estimated by various techniques. The bold figures are the values obtained by us. All values are in eV.

The growth characteristics were eventually used as a comparative experimental input for our KMC simulations. Using values of different activation energies (either measured by us or theoretically computed by others) to fix the free model parameters, we were looking for the unique combination of the remaining unfixed free parameters, for which the simulated growth characteristics perfectly match the experimentally measured ones. For Sn we were looking for unique combination of 3 model parameters - $E_a^{\|}$, $E_a^{\perp}$ and $E_a^{C}$. For Al we were looking for unique combination of only 2 model parameters - $E_a^{\|}$ and $E_a^{\perp}$. Fitting the simulated results to the experimental measurements yielded unique values of the free parameters both for Sn and for Al.

Our findings concerning the hopping barriers for Al and Sn are summarized in Table 7.1 (see bold figures) together with the values already published for the same metals and for In.

# Bibliography

[1]W. Shakespeare, "Hamlet, Prince of Denmark", in *Complet. work. william shakespear.* (Wordsworth Editions Limited, London, 2007), pp. 670–713.

[2]X. G. Zhang, *Electrochemistry of Silicon and Its Oxide* (Kluwer Academic Publishers, Boston, 2004), pp. 1–537.

[3]J. A. Appelbaum, G. A. Baraff, and D. R. Hamann, "The Si (100) surface. III. Surface reconstruction", Phys. Rev. B **14**, 588–601 (1976).

[4]A. Ramstad, G. Brocks, and P. J. Kelly, "Theoretical study of the Si(100) surface reconstruction", Phys. Rev. B **51**, 14504–14523 (1995).

[5]M. Hortamani, "Theory of Adsorption, Diffusion and Spinpolarization of Mn on Si (001) and Si (111) Substrates", Doctoral thesis (Freie Universitat Berlin, 2006), pp. 1–179.

[6]D. J. Chadi, "Atomic and Electronic Structures of Reconstructed Si(100) Surfaces", Phys. Rev. Lett. **43**, 43–47 (1979).

[7]R. J. Hamers and U. K. Köhler, "Determination of the local electronic structure of atomic-sized defects on Si(001) by tunneling spectroscopy", J. Vac. Sci. Technol. A **7**, 2854–2859 (1989).

[8]R. A. Wolkow, "Direct observation of an increase in buckled dimers on Si(001) at low temperature", Phys. Rev. Lett. **68**, 2636–2639 (1992).

[9]K. Hata, Y. Sainoo, and H. Shigekawa, "Atomically Resolved Local Variation of the Barrier Height of the Flip-Flop Motion of Single Buckled Dimers of Si(100)", Phys. Rev. Lett. **86**, 3084–3087 (2001).

[10]C. B. Duke, "Semiconductor Surface Reconstruction: The Structural Chemistry of Two-Dimensional Surface Compounds", Chem. Rev. **96**, 1237–1260 (1996).

[11]K. Takayanagi, Y. Tanishiro, M. Takahashi, and S. Takahashi, "Structural analysis of Si(111)-7 × 7 by UHV-transmission electron diffraction and microscopy", J. Vac. Sci. Technol. A Vacuum, Surfaces, Film. **3**, 1502–1506 (1985).

[12]R. J. Hamers, R. M. Tromp, and J. E. Demuth, "Surface Electronic Structure of Si (111)-(7 × 7) Resolved in Real Space", Phys. Rev. Lett. **56**, 1972–1975 (1986).

[13]J. A. Kubby and J. J. Boland, "Scanning tunneling microscopy of semiconductor surfaces", Surf. Sci. Rep. **26**, 61–204 (1996).

[14]Y. Suda, N. Hosoya, and K. Miki, "Si submonolayer and monolayer digital growth operation techniques using Si2H6 as atomically controlled growth nanotechnology", Appl. Surf. Sci. **216**, 424–430 (2003).

[15]Y. Yamada, A. Girard, H. Asaoka, H. Yamamoto, and S. Shamoto, "Single-domain Si (110) -16 × 2 surface fabricated by electromigration", Phys. Rev. B **76**, 153309 (2007).

[16]A. Alguno, S. N. Filimonov, and M. Suemitsu, "Step bunching and step "rotation" in homoepitaxial growth of Si on Si(110)-16 × 2", Surf. Sci. **605**, 838–843 (2011).

[17] T. An, M. Yoshimura, I. Ono, and K. Ueda, "Elemental structure in Si(110)-"16 × 2" revealed by scanning tunneling microscopy", Phys. Rev. B **61**, 3006–3011 (2000).

[18] A. A. Stekolnikov, J. Furthmüller, and F. Bechstedt, "Long-range surface reconstruction: Si(110)-(16 × 2)", Phys. Rev. Lett. **93**, 136104 (2004).

[19] A. A. Stekolnikov, J. Furthmüller, and F. Bechstedt, "Structural elements on reconstructed Si and Ge(110) surfaces", Phys. Rev. B **70**, 045305 (2004).

[20] K. Sakamoto, M. Setvín, K. Mawatari, P. E. J. Eriksson, K. Miki, and R. I. G. Uhrberg, "Electronic structure of the Si(110) - (16×2) surface: High-resolution ARPES and STM investigation", Phys. Rev. B **79**, 045304 (2009).

[21] M. Setvín, V. Brázdová, K. Miki, and D. R. Bowler, "Step structure of Si(110)-(16 × 2 ) and adsorption of H2O", Phys. Rev. B **82**, 125421 (2010).

[22] M. Setvín, V. Brázdová, D. R. Bowler, K. Tomatsu, K. Nakatsuji, F. Komori, and K. Miki, "Electronic structure of Si(110)-(16×2) studied by scanning tunneling spectroscopy and density functional theory", Phys. Rev. B **84**, 115317 (2011).

[23] Y. Ohira, M. Yoshimura, and K. Ueda, "Pd-Induced Surface Reconstructions of Si(110) Studied by Scanning Tunneling Microscopy and Low-Energy Electron Diffraction", Jpn. J. Appl. Phys. **46**, 1630–1634 (2007).

[24] S. R. Schofield, N. J. Curson, J. L. O'Brien, M. Y. Simmons, R. G. Clark, N. A. Marks, H. F. Wilson, G. W. Brown, and M. E. Hawley, "Split-off dimer defects on the Si(001)2 × 1 surface", Phys. Rev. B **69**, 085312 (2004).

[25] K. Hata, S. Ozawa, and H. Shigekawa, "Metastable and excited states of the C defects of Si(001)", Surf. Sci. **441**, 140–148 (1999).

[26] K. Hata, S. Ozawa, Y. Sainoo, K. Miyake, and H. Shigekawa, "Electronic structure of the C defects of Si(001) measured by scanning tunneling spectroscope at room and low temperature (80 K)", Surf. Sci. **447**, 156–164 (2000).

[27] M. Nishizawa, T. Yasuda, S. Yamasaki, K. Miki, M. Shinohara, N. Kamakura, Y. Kimura, and M. Niwano, "Origin of type-C defects on the Si(100)(2 × 1) surface", Phys. Rev. B **65**, 161302 (2002).

[28] Y. J. Chabal and S. B. Christman, "Evidence of dissociation of water on the Si(100)2 × 1 surface", Phys. Rev. B **29**, 6974–6976 (1984).

[29] M. Z. Hossain, Y. Yamashita, K. Mukai, and J. Yoshinobu, "Model for C defect on Si(100): The dissociative adsorption of a single water molecule on two adjacent dimers", Phys. Rev. B **67**, 153307 (2003).

[30] O. Warschkow, S. R. Schofield, N. A. Marks, M. W. Radny, P. V. Smith, and D. R. McKenzie, "Water on silicon (001): C defects and initial steps of surface oxidation", Phys. Rev. B **77**, 201305 (2008).

[31] P. Sobotík and I. Ošt'ádal, "Transformations of C-type defects on Si(100)-2×1 surface at room temperature – STM/STS study", Surf. Sci. **602**, 2835–2839 (2008).

[32] M. A. Albao, M. M. R. Evans, J. Nogami, D. D. Zorn, M. S. Gordon, and J. W. Evans, "Monotonically decreasing size distributions for one-dimensional Ga rows on Si(100)", Phys. Rev. B **72**, 035426 (2005).

[33] M. A. Albao, M. M. R. Evans, J. Nogami, D. D. Zorn, M. S. Gordon, and J. W. Evans, "Reply to "Comment on 'Monotonically decreasing size distributions for one-dimensional Ga rows on Si(100)' "", Phys. Rev. B **74**, 037402 (2006).

[34] P. Kocán, P. Sobotík, I. Ošt'ádal, J. Javorský, and M. Setvín, "Stability of In rows on Si(100) during STM observation", Surf. Sci. **601**, 4506–4509 (2007).

[35] P. Kocán, L. Jurczyszyn, P. Sobotík, and I. Ošt'ádal, "Defects on the Si(100)2× 1 surface: Anchoring site", Phys. Rev. B **77**, 113301 (2008).

[36] P. Kocán, P. Sobotík, and I. Ošt'ádal, "Role of surface defects in room-temperature growth of metals on Si(100)2 × 1", Czechoslov. J. Phys. **56**, 27–32 (2006).

[37] P. Kocán, P. Sobotík, and I. Ošt'ádal, "Comment on "Monotonically decreasing size distributions for one-dimensional Ga rows on Si(100)"", Phys. Rev. B **74**, 037401 (2006).

[38] M. A. Albao, J. W. Evans, and F.-C. Chuang, "A kinetic Monte Carlo study on the role of defects and detachment in the formation and growth of In chains on Si(100)", J. Phys. Condens. Matter **21**, 405002 (2009).

[39] J. Javorský, M. Setvín, I. Ošt'ádal, P. Sobotík, and M. Kotrla, "Heterogeneous nucleation and adatom detachment at one-dimensional growth of In on Si(100)2 × 1", Phys. Rev. B **79**, 165424 (2009).

[40] M. Kučera, P. Kocán, P. Sobotík, K. Majer, and I. Ošťádal, "Analysis of the Sn chain length fluctuations on Si(100) 2 × 1: An extraction of microscopic parameters", Phys. Rev. B **96**, 045430 (2017).

[41] P. Kocán, P. Sobotík, I. Ošt'ádal, M. Setvín, and S. Haviár, "Modeling growth of one-dimensional islands: Influence of reactive defects", Phys. Rev. E **80**, 061603 (2009).

[42] Y. J. Li, H. Nomura, N. Ozaki, Y. Naitoh, M. Kageshima, Y. Sugawara, C. Hobbs, and L. Kantorovich, "Origin of p(2×1) Phase on Si(001) by Noncontact Atomic Force Microscopy at 5 K", Phys. Rev. Lett. **96**, 106104 (2006).

[43] A. Sweetman, S. Gangopadhyay, R. Danza, N. Berdunov, and P. Moriarty, "qPlus atomic force microscopy of the Si(100) surface: Buckled, split-off, and added dimers", Appl. Phys. Lett. **95**, 063112 (2009).

[44] M. Setvín, "Interaction of group III and IV metals with Si(100) surface in temperature range from 20 to 800K", Doctoral thesis (Charles University in Prague, 2011), pp. 1–123.

[45] G. Brocks, P. J. Kelly, and R. Car, "Adsorption of Al on Si(100): A surface polymerization reaction", Phys. Rev. Lett. **70**, 2786–2789 (1993).

[46] H. Itoh, J. Itoh, A. Schmid, and T. Ichinokawa, "Temperature-depending growth and surface structures of low-coverage Al phases on Si(100) observed by scanning tunneling microscopy", Surf. Sci. **302**, 295–302 (1994).

[47] V. G. Kotlyar, A. A. Saranin, A. V. Zotov, V. G. Lifshits, O. Kubo, H. Ohnishi, M. Katayama, and K. Oura, "High-temperature interaction of Al with Si(100) surface at low Al coverages", Surf. Sci. **506**, 80–86 (2002).

[48] C. Zhu, S. Misawa, and S. Tsukahara, "Structures of Al/Si(100) surfaces as determined by scanning tunneling microscopy", J. Appl. Phys. **80**, 4205–4207 (1996).

[49] Z.-C. Dong, D. Fujita, and H. Nejoh, "Adsorption and tunneling of atomic scale lines of indium and lead on Si(100)", Phys. Rev. B **63**, 115402 (2001).

[50] A. A. Baski, C. F. Quate, and J. Nogami, "Tin-induced reconstructions of the Si(100) surface", Phys. Rev. B **44**, 11167–11177 (1991).

[51] M. A. Walsh, S. R. Walter, K. H. Bevan, F. M. Geiger, and M. C. Hersam, "Phenylacetylene One-Dimensional Nanostructures on the Si(100)-(2 × 1):H Surface", J. Am. Chem. Soc. **132**, 3013–3019 (2010).

[52] M. A. Albao, C.-H. Hsu, D. B. Putungan, and F.-C. Chuang, "Room-temperature deposition of group III metals on Si(100): A comparative study of nucleation behavior", Surf. Sci. **604**, 396–403 (2010).

[53] J. C. Glueckstein, M. M. R. Evans, and J. Nogami, "Growth of Sn on Si(001) at room temperature", Surf. Sci. **415**, 80–94 (1998).

[54] L. Magaud, A. Pasturel, and J.-Y. Veuillen, "Instability of metallic In-Sn dimer lines on Si(100) 2 × 1 surface", Phys. Rev. B **65**, 245306 (2002).

[55] G. Brocks, P. J. Kelly, and R. Car, "Aluminum on Si(100): Growth and structure of the first layer", J. Vac. Sci. Technol. B Microelectron. Nanom. Struct. **12**, 2705 (1994).

[56] J. Nogami, A. A. Baski, and C. F. Quate, "Aluminum on the Si(100) surface: Growth of the first monolayer", Phys. Rev. B **44**, 1415–1418 (1991).

[57] C. Zhu, S. Misawa, and S. Tsukahara, "Initial stage of aluminum thin film growth on Si(100) surfaces as observed by scanning tunneling microscopy", Surf. Sci. **325**, 279–284 (1995).

[58] C. Zhu, S. Misawa, S. Tsukahara, and S. Fujiwara, "Growth kinetics of aluminum on the Si(100) surface studied by scanning tunneling microscopy", Surf. Sci. **357-358**, 926–930 (1996).

[59] H. W. Yeom, T. Abukawa, Y. Takakuwa, M. Nakamura, M. Kimura, A. Kakizaki, and S. Kono, "Initial stage growth and interface formation of Al on Si(001)2 × 1", Surf. Sci. **365**, 328–336 (1996).

[60] J. Y. Park, J. H. Seo, C. N. Whang, S. S. Kim, D. S. Choi, and K. H. Chae, "Structural determination of the low-coverage phase of Al on Si(001) surface", J. Chem. Phys. **122**, 244723 (2005).

[61] D. D. Zorn, M. A. Albao, J. W. Evans, and M. S. Gordon, "Binding and Diffusion of Al Adatoms and Dimers on the Si(100)-2×1 Reconstructed Surface: A Hybrid QM/MM Embedded Cluster Study", J. Phys. Chem. C **113**, 7277–7289 (2009).

[62] N. Shimizu, H. Kitada, and O. Ueda, "Cluster-ordered array on the Si(001) surface formed by Al deposition", Phys. Rev. B **51**, 5550–5553 (1995).

[63] C. Zhu, A. Kawazu, S. Misawa, and S. Tsukahara, "Adsorption of Al on Si(100) at high temperature", Phys. Rev. B **59**, 9760–9763 (1999).

[64] Y. Oshima, T. Hirata, T. Yokoyama, H. Hirayama, and K. Takayanagi, "Atomic structure of cluster-ordered array on the Si(001) surface induced by aluminum", Surf. Sci. **465**, 81–89 (2000).

[65] D. V. Gruznev, D. A. Olyanich, V. A. Avilov, A. A. Saranin, and A. V. Zotov, “Growth of In nanocrystallite arrays on the Si(100)-c($4\times12$)–Al surface”, Surf. Sci. **600**, 4986–4991 (2006).

[66] V. G. Kotlyar, Y. V. Luniakov, A. V. Zotov, and A. A. Saranin, “Peculiarities of Al magic cluster self-assembly on Si(100) surface”, Surf. Sci. **604**, 674–678 (2010).

[67] Y. W. Mo, J. Kleiner, M. B. Webb, and M. G. Lagally, “Activation energy for surface diffusion of Si on Si(001): A scanning-tunneling-microscopy study”, Phys. Rev. Lett. **66**, 1998–2001 (1991).

[68] M. C. Bartelt and J. W. Evans, “Nucleation and growth of square islands during deposition: Sizes, coalescence, separations and correlations”, Surf. Sci. **298**, 421–431 (1993).

[69] C. Ratsch, A. Zangwill, P. Šmilauer, and D. D. Vvedensky, “Saturation and scaling of epitaxial island densities”, Phys. Rev. Lett. **72**, 3194–3197 (1994).

[70] D. D. Vvedensky, “Scaling functions for island-size distributions”, Phys. Rev. B **62**, 15435–15438 (2000).

[71] J. A. Stroscio and D. T. Pierce, “Scaling of diffusion-mediated island growth in iron-on-iron homoepitaxy”, Phys. Rev. B **49**, 8522–8525 (1994).

[72] J. R. Albia and M. A. Albao, “Non-Arrhenius temperature dependence of the island density of one-dimensional Al chains on Si(100): A kinetic Monte Carlo study”, J. Vac. Sci. Technol. A Vacuum, Surfaces, Film. **33**, 021404 (2015).

[73] J. R. Albia and M. A. Albao, “Dynamic scaling of island size distribution in submonolayer one-dimensional growth”, Phys. Rev. E **95**, 042802 (2017).

[74] A. G. Syromyatnikov, M. R. Guseynova, A. M. Saletsky, and A. L. Klavsyuk, “Non-equilibrium island size distribution in one dimension”, J. Stat. Mech. Theory Exp. **2020**, 093202 (2020).

[75] V. I. Tokar and H. Dreyssé, “Scaling in the equilibrium size distribution of one-dimensional surface clusters”, Phys. Rev. B **74**, 115414 (2006).

[76] D. P. Woodruff, “Surface Microscopies”, in *Mod. tech. surf. sci.* (Cambridge University Press, Cambridge, 2016) Chap. 4, pp. 215–286.

[77] R. Young, J. Ward, and F. Scire, “Observation of Metal-Vacuum-Metal Tunneling, Field Emission, and the Transition Region”, Phys. Rev. Lett. **27**, 922–924 (1971).

[78] G. Binnig, H. Rohrer, C. Gerber, and E. Weibel, “Tunneling through a controllable vacuum gap”, Appl. Phys. Lett. **40**, 178–180 (1982).

[79] G. Binnig, H. Rohrer, C. Gerber, and E. Weibel, “Surface Studies by Scanning Tunneling Microscopy”, Phys. Rev. Lett. **49**, 57–61 (1982).

[80] G. Binnig, H. Rohrer, C. Gerber, and E. Weibel, “$7\times7$ Reconstruction on Si(111) Resolved in Real Space”, Phys. Rev. Lett. **50**, 120–123 (1983).

[81] G. Binnig, C. F. Quate, and C. Gerber, “Atomic Force Microscope”, Phys. Rev. Lett. **56**, 930–933 (1986).

[82] M. Schmid and G. Pietrzak, “Scanning Tunneling Microscope schematic”, https:// commons.wikimedia.org /w/index.php?curid=180388 (2020).

[83] G. Gamow, “Zur Quantentheorie des Atomkernes”, Zeitschrift für Phys. **51**, 204–212 (1928).

[84] L. Skála, “Potenciálová jáma konečné hloubky a potenciálový val”, in *Úvod do kvantové mech.* (Academia, Praha, 2005) Chap. 14, pp. 97–107.

[85] L. Eckertová, “Fyzikální elektronika pevných látek”, in *Fyzikální elektron. pevných látek*, 1st ed. (Karolinum, Praha, 1992), pp. 111–123.

[86] L. I. Schiff, “The Wentzel-Kramers-Brillouin-Jeffreys Approximation”, in *Quantum mech.* (McGraw-Hill Education, 1968), W14–15.

[87] C. Bai, “The Tunneling Effect”, in *Scanning tunneling microsc. its appl.* (Springer-Verlag Berlin Heidelberg New York, 1995) Chap. 2, pp. 10–32.

[88] J. Tersoff and D. R. Hamann, “Theory of the scanning tunneling microscope”, Phys. Rev. B **31**, 805–813 (1985).

[89] E. P. Stoll, “Restoration of STM images distorted by time-dependent piezo driver aftereffects”, Ultramicroscopy **42-44**, 1585–1589 (1992).

[90] E. P. Stoll, “Correction of geometrical distortions in scanning tunneling and atomic force microscopes caused by piezo hysteresis and nonlinear feedback”, Rev. Sci. Instrum. **65**, 2864–2869 (1994).

[91] M. Kučera, “Study of growth of 1-D structures containig atoms from III. and IV. group of metals by STM”, Diploma thesis (Charles University in Prague, 2011), p. 73.

[92] N. D. Lang, “Theory of Single-Atom Imaging in the Scanning Tunneling Microscope”, Phys. Rev. Lett. **56**, 1164–1167 (1986).

[93] N. D. Lang, “Spectroscopy of single atoms in the scanning tunneling microscope”, Phys. Rev. B **34**, 5947–5950 (1986).

[94] J. A. Stroscio, R. M. Feenstra, D. M. Newns, and A. P. Fein, “Voltage-dependent scanning tunneling microscopy imaging of semiconductor surfaces”, J. Vac. Sci. Technol. A Vacuum, Surfaces, Film. **6**, 499–507 (1988).

[95] R. M. Feenstra and P. Mårtensson, “Fermi-Level Pinning at the Sb/GaAs(110) Surface Studied by Scanning Tunneling Spectroscopy”, Phys. Rev. Lett. **61**, 447–450 (1988).

[96] R. M. Feenstra, “Tunneling spectroscopy of the (110) surface of direct-gap III-V semiconductors”, Phys. Rev. B **50**, 4561–4570 (1994).

[97] R. M. Feenstra, G. Meyer, and K. H. Rieder, “Transport limitations in tunneling spectroscopy of Ge(111)c(2 × 8) surfaces”, Phys. Rev. B **69**, 081309 (2004).

[98] R. M. Feenstra, Y. Dong, M. P. Semtsiv, and W. T. Masselink, “Influence of tip-induced band bending on tunnelling spectra of semiconductor surfaces”, Nanotechnology **18**, 044015 (2006).

[99] R.-L. Lo, I.-S. Hwang, M.-S. Ho, and T. T. Tsong, “Diffusion of Single Hydrogen Atoms on Si(111)-(7 × 7) Surfaces”, Phys. Rev. Lett. **80**, 5584–5587 (1998).

[100] J. M. Gómez-Rodríguez, J. J. Sáenz, A. M. Baró, J.-Y. Veuillen, and R. C. Cinti, “Real-Time Observation of the Dynamics of Single Pb Atoms on Si(111)(7× 7) by Scanning Tunneling Microscopy”, Phys. Rev. Lett. **76**, 799–802 (1996).

[101] Y. W. Mo, “Precursor states in the adsorption of Sb4 on Si(001)”, Phys. Rev. Lett. **69**, 3643–3646 (1992).

[102] Y. W. Mo, “Direct determination of surface diffusion by displacement distribution measurement with scanning tunneling microscopy”, Phys. Rev. Lett. **71**, 2923–2926 (1993).

[103] N. Kitamura, M. G. Lagally, and M. B. Webb, “Real-time observations of vacancy diffusion on Si(001)-(2 × 1) by scanning tunneling microscopy”, Phys. Rev. Lett. **71**, 2082–2085 (1993).

[104] E. Ganz, S. K. Theiss, I.-S. Hwang, and J. Golovchenko, “Direct measurement of diffusion by hot tunneling microscopy: Activation energy, anisotropy, and long jumps”, Phys. Rev. Lett. **68**, 1567–1570 (1992).

[105] Z. Zhang, F. Wu, H. J. W. Zandvliet, B. Poelsema, H. Metiu, and M. G. Lagally, “Energetics and Dynamics of Si Ad-Dimers on Si(001)”, Phys. Rev. Lett. **74**, 3644–3647 (1995).

[106] P. Sobotík, P. Kocán, and I. Ošt’ádal, “Direct observation of Ag intercell hopping on the Si(111)-(7 × 7) surface”, Surf. Sci. **537**, L442–L446 (2003).

[107] P. Sobotík, M. Setvín, P. Zimmermann, P. Kocán, I. Ošt’ádal, P. Mutombo, M. Ondráček, and P. Jelínek, “Emergence of state at Fermi level due to the formation of In-Sn heterodimers on Si(100)-2 × 1”, Phys. Rev. B **88**, 205406 (2013).

[108] M. J. Rost, “In Situ Real-Time Observation of Thin Film Deposition: Roughening, Zeno Effect, Grain Boundary Crossing Barrier, and Steering”, Phys. Rev. Lett. **99**, 266101 (2007).

[109] D. W. Pohl and R. Möller, ““TRACKING” TUNNELING MICROSCOPY”, Rev. Sci. Instrum. **59**, 840–842 (1988).

[110] B. S. Swartzentruber, “Direct Measurement of Surface Diffusion Using Atom-Tracking Scanning Tunneling Microscopy”, Phys. Rev. Lett. **76**, 459–462 (1996).

[111] K. Wang, C. Zhang, M. M. T. Loy, and X. Xiao, “Time-Dependent Tunneling Spectroscopy for Studying Surface Diffusion Confined in Nanostructures”, Phys. Rev. Lett. **94**, 036103 (2005).

[112] C. Zhang, G. Chen, K. Wang, H. Yang, T. Su, C. T. Chan, M. M. T. Loy, and X. Xiao, “Experimental and Theoretical Investigation of Single Cu, Ag, and Au Atoms Adsorbed on Si(111)-(7 × 7)”, Phys. Rev. Lett. **94**, 176104 (2005).

[113] M. Setvín, J. Javorský, Z. Majzik, P. Sobotík, P. Kocán, and I. Ošt’ádal, “Competition between thermally activated and tip-induced hopping of indium atoms on Si(100)”, Phys. Rev. B **85**, 081403 (2012).

[114] K. Hata, T. Kimura, S. Ozawa, and H. Shigekawa, “How to fabricate a defect free Si(001) surface”, J. Vac. Sci. Technol. **18**, 1933–1936 (2000).

[115] A. B. Bortz, M. H. Kalos, and J. L. Lebowitz, “A new algorithm for Monte Carlo simulation of Ising spin systems”, J. Comput. Phys. **17**, 10–18 (1975).

[116] T.-L. Chan, C.-Z. Wang, Z.-Y. Lu, and K.-M. Ho, "A first-principles study of Group IV dimer chains on Si(100)", Phys. Rev. B **72**, 045405 (2005).

[117] B. Pieczyrak and L. Jurczyszyn, "Influence of C-defect at Si(001) surface on the adsorption of Al, Ag and Pb atoms", Appl. Surf. Sci. **304**, 91–95 (2014).

[118] M. M. R. Evans and J. Nogami, "Indium and gallium on Si(001): A closer look at the parallel dimer structure", Phys. Rev. B **59**, 7644–7648 (1999).

[119] H. Itoh, J. Itoh, A. Schmid, and T. Ichinokawa, "Structures of low-coverage phases of Al on the Si(100) surface observed by scanning tunneling microscopy", Phys. Rev. B **48**, 14663–14666 (1993).

[120] K. Endo, K. Arima, T. Kataoka, K. Hirose, Y. Oshikane, H. Inoue, H. Kuramochi, T. Sato, and Y. Mori, "STM/STS and the first principles calculations on Al/Si(001)2 × 1", Appl. Phys. A Mater. Sci. Process. **66**, S145–S148 (1998).

[121] C. Zhu, S. Misawa, S. Tsukahara, A. Kawazu, and S. J. Pang, "Adsorption and growth of Al on Si(100) in the initial stage", Appl. Phys. A Mater. Sci. Process. **68**, 145–151 (1999).

[122] T. Jarolímek, J. Mysliveček, P. Sobotík, and I. Ošt'ádal, "Adsorption and diffusion of Ag atoms on Si(1 1 1)-(7 × 7) surface", Surf. Sci. **482-485**, 386–390 (2001).

[123] R. E. Burgess, "Homophase and heterophase fluctuations in semiconducting crystals", Discuss. Faraday Soc. **28**, 151 (1959).

# List of Figures

# List of Tables

# List of Abbreviations

| | |
|---|---|
| 1-D | One-Dimensional |
| 2-D | Two-Dimensional |
| AFM | Atomic Force Microscope |
| DFT | Density Functional Theory |
| FEM | Field Emission Microscope |
| FIM | Field Ion Microscope |
| KMC | Kinetic Monte Carlo |
| LEED | Low-Energy Electron Diffraction |
| LDOS | Local Density Of States |
| LT | Low Temperature |
| ML | Mono-Layer |
| RHEED | Reflection High-Energy Electron Diffraction |
| RT | Room Temperature |
| SPM | Scanning Probe Microscopy |
| STM | Scanning Tunneling Microscopy |
| STS | Scanning Tunneling Spectroscopy |
| UHV | Ultra High Vacuum |
| XPS | X-ray Photoelectron Spectroscopy |

# List of publications

(1) M. Kučera, P. Kocáan, P. Sobotík, K. Majer, and I. Ošťádal, “Analysis of the Sn chain length fluctuations on Si(100)-(2 × 1): An extraction of microscopic parameters”, *Phys. Rev. B* **96**, 045430 (2017).

(2) M. Vondráček, D. Kalita,3, M. Kučera, L. Fekete, J. Kopeček, J. Lančok, J. Coraux, V. Bouchiat, J. Honolka, "Nanofaceting as a stamp for periodic graphene charge carrier modulations", *Sci. Rep.*, 23663 (2016).

(3) K. Majer, F. Rozbořil, M. Kučera, M. Setvín, P. Sobotík, I. Ošťádal, "Details of Al Atomic Chain Morphology on Si(100) Surface Observed by STM", *WDS 2014 - Proceedings of Contributed Papers - Physics*, ed. by J. Šafránková and J. Pavlů, (Matfyzpress, Prague, 2014), pp. 141-147.

(4) M. Kučera, P. Kocán, P. Sobotík., P. Zimmermann, K. Majer, I. Ošťádal, "Stability of Tin Chains on Si(100)-(2 × 1) Studied by STM", *WDS 2014 - Proceedings of Contributed Papers — Physics*, ed. by J. Šafránková and J. Pavlů, (Matfyzpress, Prague, 2014), pp. 136-140.

(5) M. Kučera, F. Rozbořil, P. Sobotík., I. Ošťádal, "Aluminium on the Si(100)-(2 × 1) - "Growth, Morphology, and Different Modifications of Aluminium Dimers Studied by STM", *WDS'13 Proceedings of Contributed Papers: Part III - Physics*, ed. by J. Šafránková and J. Pavlů, (Matfyzpress, Prague, 2013), pp. 110-115.